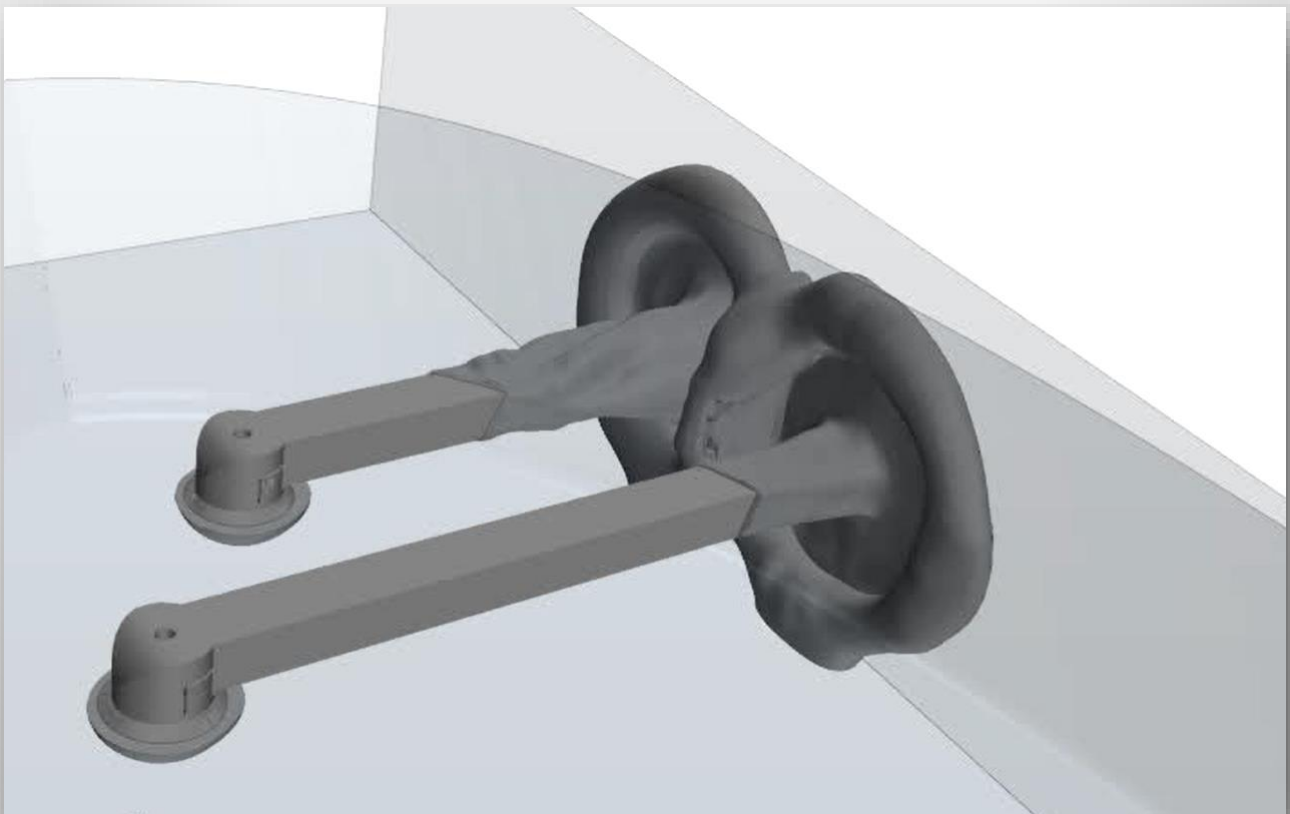


Numerical simulation of bow thruster induced near-bed flow next to quay wall

Thom Haafkes

4375246



Numerical simulation of bow thruster induced near-bed flow next to quay wall

MSc Thesis

by

Thom Haafkes

to obtain the degree of Master of Science
at the Delft University of Technology,
to be defended publicly on Friday May 21, 2021 at 14:00.

Student number:	4375246	
Project duration:	June 2020 – May 2021	
Thesis committee:	Prof. dr. ir. T. J. C. van Terwisga	TU Delft
	Dr. ir. H. J. de Koning Gans	TU Delft
	Dr. ir. T. S. D. O'Mahoney	Deltares
	Ir. A. J. van der Hout	Deltares, TU Delft

An electronic version of this thesis is available at <http://repository.tudelft.nl/>.

Abstract

During berthing operations of ships, the horizontal thrusters cause a hydraulic load on the quay wall and bed. This could eventually lead to scour holes in the bed, which may affect the structural integrity of the quay wall. This thesis is about a numerical simulation of a bowthruster jet which is deflected by a quay wall and the focus of this study will be on the resulting bottom velocities. In 2019, field measurements were executed with an inland vessel and the measured bottom velocities were low compared to the design guidelines. The goal of this study is to simulate the field measurements in a numerical model to gather more knowledge about the flow field induced by bowthrusters next to quay walls. The obtained numerical results are compared to the field measurement and to the design guidelines of PIANC. As it turns out, the velocity sensors probably did not measure the maximum bottom velocity during the field measurements, since they are located slightly above the highest velocities at the bottom, as predicted by the numerical simulations. The maximum bottom velocities from the numerical simulation are similar to the expected near-bed bottom velocities by PIANC. However, there is room for improvement in these design guidelines, e.g., adjusting the efflux velocity for tunnel thrusters to account for the variation in cross-sectional area between propeller and tunnel exit.

Preface

This thesis is the final report to hand in to complete a Master's degree in Marine Technology at the Delft University of Technology. During the past 11 months I worked on a numerical model of a bowthruster jet to predict the near bed velocities. This thesis could not have been completed without the help and support of several people, who I would like to thank here.

Firstly, I would like to thank my supervisors Prof. dr. ir. T.J.C. van Terwisga and Dr.ir. H.J. de Koning Gans for their excellent guidance throughout my research. Secondly, I would like to express my gratitude to my daily supervisor from Deltares, Tom O'Mahoney for the wonderful, and sometimes long, brainstorming and discussion sessions. He guided me through the numerical program and within a short time I was familiar to it. Last but definitely not least, I would like to thank Arne van der Hout, my other supervisor from Deltares, his tips and guidance at the decisive moments really helped me to follow the right path during my research. Besides my direct supervisors, I also want to thank all the other colleagues from Deltares and within the CROW propeller jet meetings for their sincere interest and their interesting questions.

The pandemic has demanded a more online cooperation and working from home has some advantages and disadvantages. I want to thank my friends and roommates for the countless walks where I could take load off my mind. Finally, I want to thank my family, who have supported me through my whole study process.

*Thom Haafkes
Rotterdam, April 2021*

Contents

List of Figures	ix
List of Tables	xiii
1 Introduction	1
1.1 State of the art	2
1.2 Objective and research questions	2
1.3 Outline	3
2 Theory	5
2.1 Bow thruster	5
2.2 Induced flow velocities	6
2.2.1 Free jet velocity distribution	6
2.2.2 Transverse thruster velocity distribution	7
2.2.3 Efflux velocity	9
2.3 CFD modelling	9
2.3.1 Meshing	10
2.3.2 Wall functions	10
2.3.3 Turbulence Modelling	13
2.3.4 RANS	14
2.3.5 Governing equations of $k-\varepsilon$ model	17
2.3.6 Turbulence Intensity	18
2.3.7 Propeller model	19
2.4 TU Delft Theses	20
2.5 Conclusive remarks from literature	21
3 Virtual disk	23
3.1 Reference experiment	23
3.2 CFD implementation	23
3.3 Results	24
3.3.1 Free flow	26
3.3.2 Solution for discrepancies	27
3.4 Convergence study	28
3.4.1 Convergence in time	28
3.4.2 Mesh convergence	29
3.5 Turbulence models	31
3.5.1 Convergence of k-omega turbulence model	32
4 Vorstenbosch model	35
4.1 Built models	35
4.1.1 Comparison Cantoni	35
4.1.2 Comparison PIANC guidelines	35
4.1.3 Parameter sensitivity tests	35
4.2 Model setup	36
4.2.1 Ship geometry	36
4.2.2 Tunnel thruster	37
4.2.3 Boundary conditions	38
4.2.4 Mesh	39

5 Results	41
5.1 Convergence over time	41
5.2 Comparison with field measurements	44
5.3 Comparison with PIANC theory	46
5.3.1 Efflux velocity	46
5.3.2 Maximum bottom velocity	48
5.4 Independence of location of boundaries.	51
5.5 Wall jet thickness	51
5.6 Turbulence Intensity	54
5.7 Parameter sensitivity analysis	55
6 Discussion	57
7 Conclusion	61
7.1 Research questions	61
7.2 General conclusions	62
8 Recommendations	63
Bibliography	65
A German free jet velocity distribution	67
B Velocity field all tests	69
C Sensor convergence	71
D Velocity profiles	73
E Bottom velocity field	75
F Wall velocity field	77
G Velocity along line	79
H Roughness	81
I Instantaneous vs. mean	83

List of Figures

1.1	Bow thruster jet against quay wall (from PIANC [17])	1
2.1	Tunnel thruster (from Veth [35])	5
2.2	Tunnel thruster (from PIANC [17])	5
2.3	Pump jet thruster (from PIANC [17])	6
2.4	Transverse pump jet thruster (from PIANC [17])	6
2.5	flow field development of a transverse thruster (from PIANC [17])	6
2.6	Bottom velocity as a function of the position of the thruster to the quay wall and the bottom (from Schmidt [22])	8
2.7	Fine grid resolution is needed near the wall to accurately solve the steep gradients	11
2.8	Law of wall (from Simcenter STAR-CCM+ [24])	11
2.9	Base size y_H and wall distance y_{wall} definition	13
2.10	Turbulence models in CFD	14
2.11	Reynolds decomposition in typical flow measurement	14
3.1	Photo of experimental setup of Wei (from Wei [36])	23
3.2	Mesh on a section for the simulation of the Wei experiments	24
3.3	Velocity field obtained from CFD for different wall clearances	25
3.4	Velocity field obtained from Wei [36] for different wall clearances	25
3.5	The free flow velocity comparison (with wall clearances of $10-20D_p$)	26
3.6	2D velocity field for three different cases where the influence of K_q on the spreading of the jet is studied	27
3.7	Velocity monitors that show the convergence over time	28
3.8	Mesh used for convergence study (130.705 cells)	29
3.9	Mesh used for convergence study (6.787.659 cells)	29
3.10	Mesh convergence	29
3.11	Obtained 2D velocity field for every mesh size	30
3.12	Reference 2D velocity field on the left and on the right the velocity field obtained with the side walls and floor further away. The spreading is significantly more present when the side walls and floor are placed further away from the jet.	30
3.13	2D velocity field of different turbulence models at solution time of 40 s	31
3.14	Mean 2D velocity field of different turbulence models (20-40 sec)	32
3.15	Mesh convergence of $k - \omega$ turbulence model	32
3.16	Maximum 2D velocity over time for the finest two meshes	33
3.17	Obtained 2D velocity field for every mesh size of $k - \omega$ turbulence model	33
4.1	Tanker 3D CAD (from 3D Warehouse [11])	36
4.2	Filling of old bow thruster channel system in 3D CAD	37
4.3	Veth jet (from Veth [35])	37
4.4	Top view of old hull, with wrong wall clearances	37
4.5	Top view of new hull, with correct wall clearances	37
4.6	3D view of both channels in CAD model	38
4.7	Tunnel dimensions	38
4.8	The domain of the CFD model (Test 13)	39
4.9	Control volumes in which the mesh is refined	39
4.10	Mesh in cross section through tunnel thruster (Test 11)	40
5.1	Instantaneous velocity field Test 11	41
5.2	CFD results for the horizontal velocity at sensor location over time for test 13	42

5.3	CFD result for the maximum bottom velocity in y-direction for each test	43
5.4	Velocity profile through sensor locations Test 11 at 81s. The mean value of the CFD results and the field measurements (FM) are plotted with their 90% confidence interval (CI).	44
5.5	Plot with the mean velocity of each sensor with a 90% Confidence Interval	45
5.6	Tunnel velocities over time for Test 1 & Test 2	46
5.7	Instantaneous velocity profile in x-direction at the outflow plane of tunnel for different tests	47
5.8	Instantaneous velocity profile in z-direction at the outflow plane of tunnel for different tests	47
5.9	Axial velocity distribution at the outflow of the tunnel of BT1	48
5.10	The 20s mean and the instantaneous velocity distribution behind BT1	48
5.11	Velocity in y-direction 0.5 cm above the bed for Test 11 after 81s	49
5.12	Velocity in x-direction 0.5 cm above the bed for Test 11 after 81s	49
5.13	Mean of the maximum bottom velocity present on the bottom with 90 % CI for CFD results compared to the PIANC guidelines with different efflux velocities V_0 as input parameter .	49
5.14	Line following a flow direction of the jet for Test 11 after 81s. Here $x_t = 3.30\text{m}$ and $h_t = 3.40\text{m}$	50
5.15	Instantaneous velocity degradation along line in Test 11 after 81s	50
5.16	Difference in maximum bottom velocity over time with boundaries located further away .	51
5.17	Wall jet thickness Test 1 after 7 seconds solution time. In the top left corner a velocity profile for different radial coordinates over the wall normal direction.	52
5.18	Wall jet thickness over radial coordinate	52
5.19	Velocity distribution over wall normal direction	53
5.20	Turbulent kinetic energy k for Test 11 after 81s	54
5.21	Turbulence intensity I for Test 11 after 81s	54
5.22	Turbulence intensity over height through ADCP1 location of Test 11 after 81s. Note here that this is not in the same plane as shown in figure 5.21.	54
5.23	Turbulent kinetic energy k and wall shear stress τ_w at the bottom for Test 11 after 81s .	55
5.24	Parameter sensitivity of keel clearance	56
5.25	Parameter sensitivity of wall clearance	56
5.26	Parameter sensitivity of nominal rotation rate	56
8.1	Include the surface roughness geometry in the mesh	64
B.1	Instantaneous velocity field trough bowthruster	69
C.1	Horizontal velocity at sensor location over time for test 1	71
C.2	Horizontal velocity at sensor location over time for test 2	71
C.3	Horizontal velocity at sensor location over time for test 11	72
C.4	Horizontal velocity at sensor location over time for test 13	72
D.1	Velocity profile through sensor locations Test 1 after 93s	73
D.2	Velocity profile through sensor locations Test 2 after 99s	73
D.3	Velocity profile through sensor locations Test 11 after 81s	74
D.4	Velocity profile through sensor locations Test 13 after 80s	74
E.1	Horizontal bottom velocity 1 cm above bed for Test 1 after 93s	75
E.2	Horizontal bottom velocity 1 cm above bed for Test 2 after 99s	75
E.3	Horizontal bottom velocity 1 cm above bed for Test 11 after 81s	75
E.4	Horizontal bottom velocity 1 cm above bed for Test 13 after 75s	75
F.1	Velocity field 1 cm from the quay wall for Test 1, 2, 11 and 13	77
G.1	Velocity degradation along line in Test 1 after 93s	79
G.2	Velocity degradation along line in Test 2 after 99s	79
G.3	Velocity degradation along line in Test 11 after 81s	80
H.1	Law of wall (adjusted from Simcenter STAR-CCM+ [24])	81

I.1	Instantaneous velocity field of the parameter sensitivity test run for keel clearance of 4.11m after 100s	83
I.2	Mean velocity field of the parameter sensitivity test run for keel clearance of 4.11m between 80-100s	83
I.3	Instantaneous velocity field of the parameter sensitivity test run for keel clearance of 4.11m after 100s	83
I.4	Mean velocity field of the parameter sensitivity test run for keel clearance of 4.11m between 80-100s	83
I.5	Instantaneous and mean velocity profile through ADCP1 location of Wall clearance 5.70m run	83

List of Tables

3.1	Propeller characteristics	23
3.2	Velocity comparison	25
4.1	Test cases	35
4.2	Parameters that are varied to check their influence on the maximum bottom velocity	36
4.3	Main dimensions of MTS Vorstenbosch	36
4.4	Main dimensions of the original 3D model [11]	36
4.5	Bowthruster characteristics (from Veth and Cantoni[7])	37
4.6	Input parameters virtual disk	38
4.7	Boundary condition specification	39
4.8	Default controls for meshing	39
4.9	Surface controls	39
4.10	Volumetric control input parameters	39
4.11	Number of cells in mesh of each test	40
5.1	Mean (μ) and standard deviation (σ) of measured V_{hor} between 10-70 seconds	45
5.2	Mean (μ) and standard deviation (σ) of different efflux velocities V_0 between 10-70 seconds from the four CFD simulations are shown in the first 4 rows. The expected efflux velocity by the PIANC guidelines are shown in the following 2 rows. The instantaneous velocity at the end of every simulation is also added at the end of the table for every test case along with the ratio between the instantaneous tangential and axial velocities.	47
5.3	Mean (μ) of the maximum bottom velocity in y-direction between 10-70 seconds of the CFD results with the expected bottom velocity by PIANC for different efflux velocities	50
5.4	Wall jet thickness δ , non-dimensional wall jet thickness $\bar{\delta}$ and the maximum wall jet velocity U_m for different radial coordinates r	52
5.5	The tested parameters with the varying values	55

Nomenclature

Acronyms

ADCP	Acoustic Doppler Current Profiler
ADV	Acoustic Doppler Velocimeter
BC	Boundary Condition
BT	Bow Thruster
CAD	Computer-Aided Design
CFD	Computational Fluid Dynamics
CI	Confidence Interval
DNS	Direct Numerical Simulation
FDM	Finite Difference Method
FM	Field Measurements
FVM	Finite Volume Method
ITTC	International Towing Tank Conference
LES	Large Eddy Simulation
MSc	Master of Science
ODE	Ordinary Differential Equation
PDE	Partial Differential Equation
PIANC	Permanent International Commission for Navigation Congresses
PIV	Particle Image Velocimetry
RANS	Reynolds-Averaged Navier Stokes
RTS	Reynolds Stress Transport
SST	Shear Stress Transport
TKE	Turbulent Kinetic Energy
TU	Technische Universiteit

Greek Symbols

Δ	Virtual disk thickness	m
δ_{ij}	Kronecker delta	
κ	Empirical coefficient	
μ	Dynamic viscosity	Ns/m ²
$\bar{\mu}$	Mean	

μ_t	Eddy viscosity	m^2/s
ν	Kinematic viscosity	m^2/s
ρ	Density	kg/m^3
σ	Standard Deviation	
σ_ε	Turbulent Prandtl number for ε	
σ_k	Turbulent Prandtl number for k	
τ	Ratio between thrust and tunnel thrust	
τ_w	Wall shear stress	N/m^2
τ_{ij}''	Reynolds stress components	m^2/s^2
ε	Rate of viscous dissipation of turbulent kinetic energy	m^2/s^3

Roman Symbols

Δp	Pressure difference	N/m^2
Δx	Cell size	m
\dot{V}	Volume flux through actuator disk	m^3/s
\hat{n}	normal pointing outwards of surface	
\vec{f}	Body accelerations	m/s^2
\vec{u}	Fluid velocity vector	m/s
A_1	Cross-sectional area inlet actuator disk	m^2
A_2	Cross-sectional area outlet actuator disk	m^2
A_θ	Body Force Method constant	
A_p	Cross-sectional area propeller actuator disk	m^2
A_x	Body Force Method constant	
C	Coefficient	
C	Courant number	
c_f	Friction coefficient	
$C_{1\varepsilon}$	Constant $k - \varepsilon$ turbulence model	
$C_{2\varepsilon}$	Constant $k - \varepsilon$ turbulence model	
C_μ	Model constant for turbulent viscosity ($k - \varepsilon$ turbulence model)	
D_0	Jet diameter at the beginning of the jet	m
D_p	Propeller diameter	m
D_{thruster}	Thruster diameter	m
E'	Empirical coefficient	
$f_{b\theta}$	Body force component in tangential direction per unit volume	N/m^3
f_{bx}	Body force component in axial direction per unit volume	N/m^3

h_t	Distance between propeller axis and bed	m
I	Turbulence intensity	
J	Advance Ratio	
k	Turbulent kinetic energy	m^2/s^2
K_Q	Torque coefficient	
K_T	Thrust coefficient	
$K_{t,prop}$	Propeller thrust coefficient	
$K_{t,Tunnel}$	Ducted thrust coefficient	
L	Characteristic length	m
n	rotational speed	s^{-1}
O	Order of magnitude of truncation error	
p	Pressure	N/m^2
p_1	Pressure at the inlet actuator disk	N/m^2
p_2	Pressure at the outlet actuator disk	N/m^2
$P_{thruster}$	Installed thruster engine power	N/m^2
p_{p1}	Pressure at the inlet propeller	N/m^2
p_{p2}	Pressure at the outlet propeller	N/m^2
Q	Torque	$\text{N} \cdot \text{m}$
r	Radial distance from the jet axis	m
R_H	Hub radius	m
R_P	Propeller tip radius	m
Re	Reynolds number	
S	Control surface	
T	Thrust	N
t	Time	s
T_T	Tunnel thrust	N
T_{prop}	Propeller thrust	N
U	Free stream velocity	m/s
u^+	Dimensionless wall-tangential velocity component	
u_*	Velocity scale which is representative of the flow velocity in the near wall region	m/s
U_{ref}	local velocity magnitude	m/s
V_0	Efflux velocity	m/s
v_1	Velocity at inlet actuator disk	m/s
v_2	Velocity at outlet actuator disk	m/s

V_A	Advance velocity of propeller	m/s
v_p	Velocity at propeller actuator disk	m/s
V_{axis}	Flow velocity in the axis of the jet	m/s
$V_{b,max}$	Maximum bottom velocity	m/s
$V_{x,r}$	Flow velocity in the jet at location x,r	m/s
x	Horizontal distance from the outflow of the jet	m
y^+	Dimensionless wall distance	
y_{wall}	Wall distance	m

Introduction

The increasing demand for transport leads to an increase of larger inland vessels that navigate through the Dutch waterways. To keep the vessels maneuverable, with their increasing draught and dead-weight, the propeller powers need to increase too. In order to be independent of assistance from tugs during berthing operations, bow and stern thrusters are installed on the ships. These horizontal thrusters cause a hydraulic load on the quay walls and could eventually scour the bed next to the vertical quay wall, as illustrated in figure 1.1. This could lead to undesirable scour holes in the bottom, which affects the structural integrity of the quay. To protect the quays, bottom protection can be installed. The question that arises is what level of bottom velocities the bottom protection needs to withstand? The current design guidelines were derived for smaller ships and propellers and may not be valid for larger ships, with increased draughts and propeller powers.

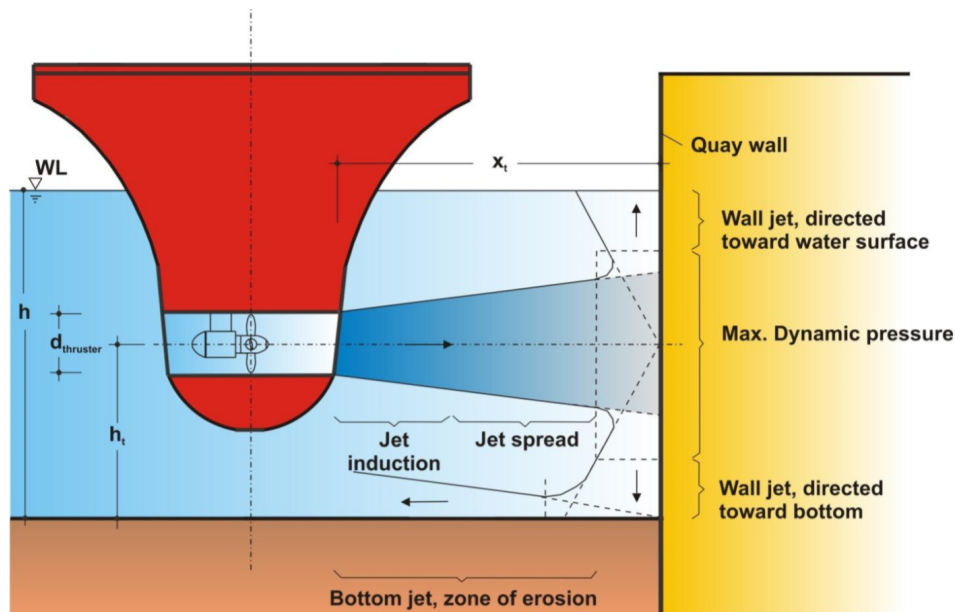


Figure 1.1: Bow thruster jet against quay wall (from PIANC [17])

The near-bed flow field induced by a bow thruster next to a quay is complex due to the phenomena of diffusion and turbulence. It becomes even more challenging when a vertical wall is deflecting the flow. Either the current quay walls with their bottom protections are under-designed, i.e., it could lead to failure, or the current quays are over-designed, which possibly means that the future quays can be designed more economically. To ensure that the design of the quay walls is suited for the near-bed flow field, more research is needed on this specific topic.

Rijkswaterstaat has started a study into the bow thruster jet next to quay walls. These studies are carried out by various companies, including Deltares. The goal of these studies is to gather more knowledge of the near-bed flow field next to quays induced by bow thrusters of inland vessels. This research will lead to improved design guidelines for quay walls. The study presented in this thesis, as part of the overarching research of Rijkswaterstaat, focuses on how a numerical model can be used to predict the near bed flow field next to a quay wall. Before the study can start, it is necessary to understand what is known from the literature about bow thruster jets next to quay walls.

1.1. State of the art

Several master theses at the TU Delft have researched the flow field at a quay wall. Bok [6] was the first researcher to look into this phenomena in 1996 and since the 2000s the Computational Fluid Dynamics (CFD) techniques are applied in the following theses; De Jong [9], Van der Laan [28], Nielsen [15], Van Blaaderen [2] and Van den Brink [27] developed a numerical model to simulate the flow next to a vertical quay wall. In addition, Veldhoven [31], Schokking [23], Van Doorn [29], De Jong [8] and Van Noort [30] did research related to bow thruster induced damage at open quay structures .

The research of Van den Brink [27] focused on the scour depth due to the thruster jet. To validate the CFD model, two cases were developed: a real size model test and a scale model test. The real size model was based on the dimensions of the full-scale experiments of an inland vessel. The scour holes of the physical full-scale experiments were compared to the scour hole depths obtained with the CFD and erosion model. Unfortunately, the bottom velocities were not measured during the full-scale experiments. For the scale model, the near bed velocities were compared with the results of the physical scale model tests done by Schmidt [22].

The goal of the research of Van Blaaderen [2], Nielsen [15] and Van der Laan [28] was to design a numerical model to simulate the flow field of a bow thruster. The flow velocities of the designed numerical model were verified by comparing them to the results of physical scale tests. The research of De Jong [9] expanded the research done by Van Veldhoven [31] and Schokking [23]. It calculated the bottom flow velocities induced by a bow thruster next to a vertical quay wall with a CFD model.

As mentioned, various research has been done into the flow field of a bow thruster next to a vertical quay wall. Most of the numerical models made were based on scale models, except for Van den Brink [27]. In this research, the full-scale numerical model scour depths were related to the full-scale experiment scour data. Due to the fact that the bottom velocities were not measured during the experiment, Rijkswaterstaat performed new full-scale field measurements with the focus on bottom velocities with the MTS Vorstenbosch in 2019. The flow velocities induced by the bow thruster of the Vorstenbosch were measured at the bottom of the Antarcicakade in the Port of Rotterdam. After Cantoni [7] compared these test results with the theory and guidelines, it was hypothesized that the guidelines suggested by PIANC [17] are conservative compared to the data obtained from the field measurements. Since the measurement data was not in line with the current theory and guidelines, a new field measurement was planned for September 2020. Parallel to this new field measurement, a new full-scale numerical simulation of a bow thruster induced flow next to a quay wall is made, which forms the objective of this thesis.

1.2. Objective and research questions

The main goal of this research is to develop a numerical model that simulates the full-scale field measurements of 2019. This means that a CFD analysis of the near-bed flow field induced by a ducted bow thruster of the MTS Vorstenbosch next to a vertical quay wall will be made. The used program for the numerical simulation is STAR-CCM+ (version 2020.1 15.02.007).

This research will help to further expand the knowledge of the physics behind the near-bed flow field induced by a bow thruster. This knowledge is valuable because it helps to improve the design guidelines of quays. It is expected that the quays are now overdesigned and with better knowledge of the exact flow field at quay walls, these quays could be designed more cost efficiently in the future.

Based on the main objective of this research the following research question is formulated:

How do the relative low bed flow velocities of the full-scale field measurements relate to the bed velocities of a numerical model and how does the bow thruster jet of an inland vessel evolve at the quay and bottom?

To help in answering this main research question, different sub-questions are established:

1. *What is the best way to implement the bow thruster propeller into the numerical model?*
2. *What turbulence model is best suited in this CFD model?*
3. *How does the numerical model relate to the field measurements of 2019 [7]?*
4. *How do the current PIANC guidelines relate to the obtained near-bed flow velocities of the numerical model?*
5. *What input parameter affects the total near-bed flow field the most?*

1.3. Outline

First, a literature study is executed to collect all the current knowledge of bow thruster jets in chapter 2. Also, the basics of CFD are covered in this chapter and it ends with conclusions drawn from the literature and answers already the first sub-question of the research. In chapter 3 the model of the virtual disk is validated based on the paper of Wei [36] and a convergence study is shown. This chapter compares different turbulence models and answers the second sub-question. In chapter 4 the developed CFD model for comparison with the field measurements and the PIANC theory is described and the results and comparisons are given in chapter 5. This chapter will answer the third and fourth sub-question. The last sub-question is answered in the parameter sensitivity test described at the end of chapter 5. A discussion of the results is presented in chapter 6, the conclusions are drawn in chapter 7 where the main research question is answered and this thesis ends with some recommendations in chapter 8.

2

Theory

In this chapter the theoretical background of a bowthruster is given and the concept of Computational Fluid Dynamics is introduced. This theory helps to identify the introduced problem, which could be beneficial to answer the research questions. The concept of a bow thruster is given in section 2.1 and this theory is based on the PIANC report 180 [17]. Section 2.2 presents the formulae to describe the velocity distribution in the jet from a propeller. The concept of CFD is shown in chapter 2.3 and the theory is based on Schaap [21], Nodeland [16], Ren [20], Versteeg & Malalasekera [34] and the user manual of STAR-CCM+ [24]. The most important findings of previous work from the TU Delft theses are presented in section 2.4. This chapter ends with some conclusive remarks in section 2.5.

2.1. Bow thruster

A transverse thruster is defined as a propeller mounted in a smooth tunnel through the hull, providing a transverse thrust, figure 2.1 and 2.2. This transverse thrust is useful in low-speed conditions, e.g. turning maneuvers in the harbor, when rudders are ineffective because they are not exposed to a slipstream. This allows the pilot to perform mooring operations without the help of tugs. The transverse thruster should be placed near the bow or near the stern, because here the generated moments will be maximum, which maximizes their maneuverability. Therefore, transverse thrusters are also known as bow and stern thrusters. The water is sucked into the tunnel at one side, because the water is accelerated by the rotation of the propeller and on the other side the water is expelled. The propeller can rotate in either clockwise or anticlockwise direction, enabling it to generate forces to both transverse directions, port and starboard.

Besides the well-known transverse tunnel thruster, there are other types of transverse thrusters. One of them is the pump jet thruster, see figure 2.3. This thruster has the intake at the keel and is originally designed as main propulsor for inland vessels, which need to operate in shallow water conditions. The outlet of a pump jet thruster can rotate in all directions, making it applicable for both propulsion oriented purposes and maneuverability purposes. Another version of this thruster is shown in figure 2.4. The MTS Vorstenbosch, which was used for the field measurements of 2019, has two four-channel transverse pump jet thruster systems, which is comparable to the transverse pump jet thruster.

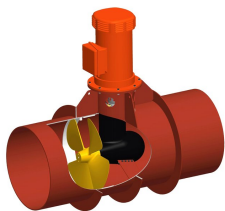


Figure 2.1: Tunnel thruster (from Veth [35])

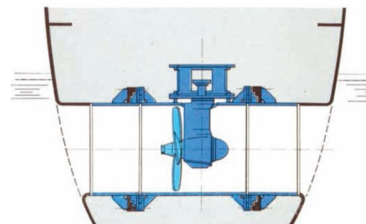


Figure 2.2: Tunnel thruster (from PIANC [17])

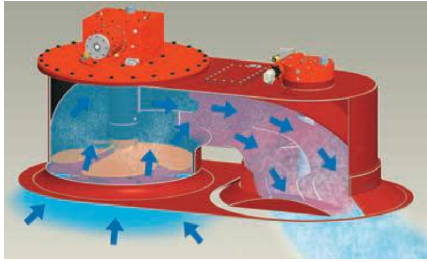


Figure 2.3: Pump jet thruster (from PIANC [17])

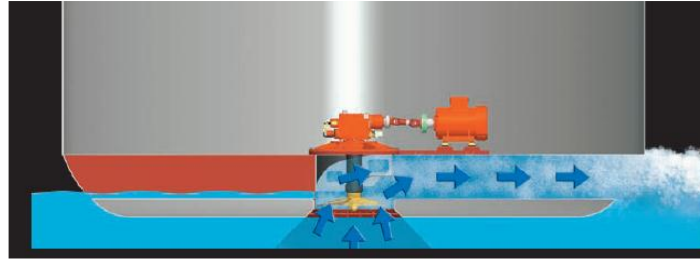


Figure 2.4: Transverse pump jet thruster (from PIANC [17])

2.2. Induced flow velocities

The jet of a propeller is a complex flow with axial, tangential and radial components of velocity. Generally jets generated by propellers can be compared with free jets. The definition of a free jet given in PIANC [17] is; *"the water flowing out of an orifice into the surrounding water without any disturbance by lateral boundaries or walls that may hinder the spreading of the jet"*.

2.2.1. Free jet velocity distribution

The free jet flow field can be divided into two regions: the zone of flow establishment close to the propeller and a zone of established flow further away from the propeller. In the zone of establishment, the core along the axis of rotation of the propeller jet has lower velocities due to the influence of the hub at the center of the propeller. The lateral velocity profile therefore has two peaks in the zone of flow establishment. The high velocities gradually penetrate into the low velocity core along longitudinal axis, which pushes the location of maximum velocity towards the center. At a certain distance downstream, the maximum velocity is located on the axis of rotation. From this point (x_0 in figure 2.5) onward, the flow is referred to as the zone of established flow.

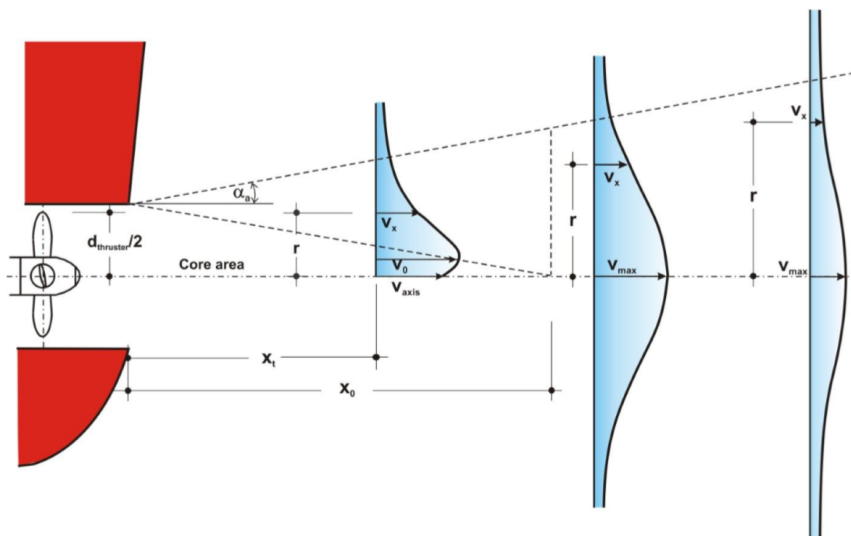


Figure 2.5: flow field development of a transverse thruster (from PIANC [17])

The distribution of the velocities in the zone of established flow is based on theories of Albertson et al. [1] and is also covered in Blaauw and van de Kaa [3] and is known as the Dutch approach. The flow field induced by a thruster is shown in figure 2.5. The governing equations for the flow distribution for propellers are shown in equations 2.1 and 2.2. The flow has a Gaussian distribution around the axis of rotation in the zone of established flow. The swirl in the jet could introduce more turbulence and mixing, which could lead to a shorter zone of establishment. There is also a German approach for the free jet velocity distribution and it can be found in appendix A.

$$V_{axis} = \frac{1}{2C} V_0 (D_0/x) \quad (2.1)$$

$$\frac{V_{x,r}}{V_{axis}} = \exp\left(-\frac{1}{2C^2} \frac{r^2}{x^2}\right) \quad (2.2)$$

where:

- V_{axis} = flow velocity in the axis of the jet [m/s]
- V_0 = efflux velocity [m/s], see section 2.2.3
- $V_{x,r}$ = flow velocity in the jet at location x, r [m/s]
- D_0 = initial jet diameter [m]
- x = horizontal distance from the outflow of the jet [m]
- r = radial distance from the jet axis [m]
- C = coefficient [-]

These formulae are now only valid in free flow situations, so without any lateral or depth limitation, such as a quay wall or riverbed. The effect of a rudder or duct on the propeller flow field is also not considered in these equations. Some indicative values of the coefficient C are addressed in the next section.

2.2.2. Transverse thruster velocity distribution

Because this research includes the effect of the bottom and the quay wall on the jet, the free jet formulae cannot be used directly. Therefore, two other approaches are introduced to approximate the bottom velocities induced by a transverse thruster jet against a vertical quay wall. These are the Dutch and German approach. The results of the velocity approximations of both methods could differ, but the formulae to translate these velocities into recommended bottom protection are also different, which results in similar design recommendations in the end. To obtain safe results, it is recommended to adopt just one approach for both the velocity estimations and the bottom protection calculations. The German method generally leads to higher bed velocities and this is compensated with smaller stone stability parameters. The Dutch method uses higher stability parameters to compensate for the lower bed velocities.

Dutch method

The Dutch method is based on work of Blaauw and van de Kaa [3], Verheij [33] and Blokland [5] [4]. The coefficient C of the free jet velocity distribution equations 2.1 and 2.2 is determined by Dutch researchers to be equal to 0.18 for ducted propellers. The bowthruster of the Vortstembosch is also ducted because there is a whole tunnel around the propeller, therefore the focus is on ducted coefficients. The flow velocity distribution equations become as in equation 2.3 and 2.4. The effective diameter is equal to $D_0 = D_p/\sqrt{2}$ for non-ducted propellers and for ducted propellers $D_0 = D_p$ according to Verhey [33]. D_p is here the propeller diameter. For propellers built in tunnels, the calculations can be based on the relation $D_0 = 0.85D_p$. However, the approach with the use of D_0 is not preferred since it is not a physical characteristic of the thruster or propeller. Thrusters are considered as free jets with an outflow opening $D_{thruster} = f_{thruster} D_p$ with $f_{thruster} = 1.02 - 1.05$.

$$V_{axis} = 2.8 V_0 (D_p/x) \quad (2.3)$$

$$\frac{V_{x,r}}{V_{axis}} = \exp\left(-15.4 \frac{r^2}{x^2}\right) \quad (2.4)$$

In absence of a quay wall, these equations can be used to calculate the flow velocities at the bed by substituting the distance between the propeller axis and the bed for parameter r . In situations with a vertical quay wall, the maximum bottom velocities $v_{b,max}$ can be calculated with equations 2.5 and 2.6.

$$v_{b,max} = 1.0 V_0 \frac{D_{thruster}}{h_t} \quad \text{for } L/h_t < 1.8 \quad (2.5)$$

$$v_{b,max} = 2.8 V_0 \frac{D_{thruster}}{L + h_t} \quad \text{for } L/h_t \geq 1.8 \quad (2.6)$$

Here is L the distance between the outflow opening and the quay wall and h_t is the height between the bed and the propeller axis, see figure 1.1.

German Method

The German method for a transverse thruster at a vertical wall is based on work of Fuehrer, Römisch & Engelke [10] and Schmidt [22], and is summarized in equations 2.7, 2.8 and 2.9.

$$V_{axis} = V_0 \quad \text{for } \frac{x}{D_{thruster}} < 1.9 \quad (2.7)$$

$$V_{axis} = 1.9 V_0 \left(\frac{D_{thruster}}{x} \right) \quad \text{for } \frac{x}{D_{thruster}} > 1.9 \quad (2.8)$$

Equation 2.7 and 2.8 are only valid between the thruster outflow and the quay wall, so $x \leq L$.

$$\frac{V_{b,max}}{V_{wall,thruster}} = a_L \left(\frac{D_{thruster}}{h_t} \right)^{1.15} \quad \text{with } a_L = 10.6 \left(\frac{D_{thruster}}{L} \right) \quad (2.9)$$

The maximum bottom velocity $v_{b,max}$ depends on the velocity at the wall $V_{wall,thruster}$ and the empirical value a_L . The wall velocity follows from equation 2.7 and 2.8. Equation 2.9 is shown in figure 2.6

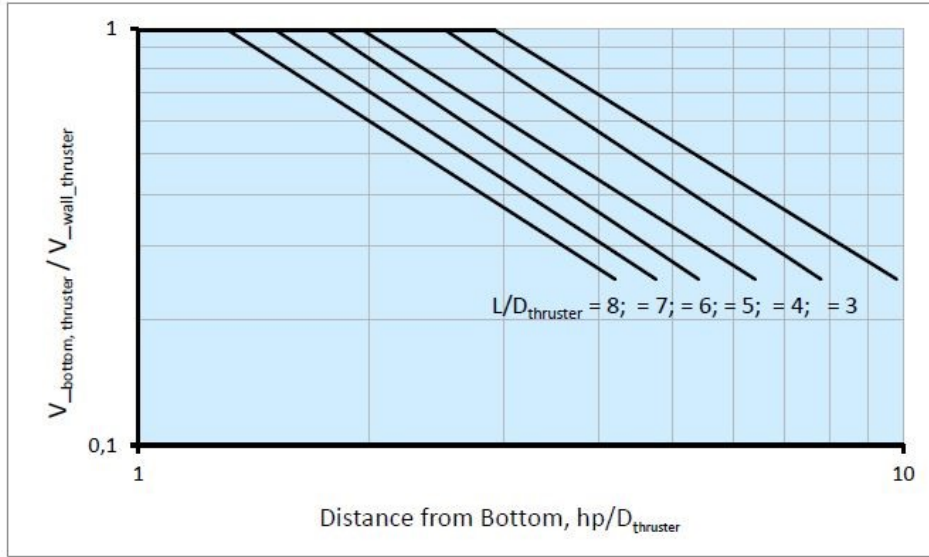


Figure 2.6: Bottom velocity as a function of the position of the thruster to the quay wall and the bottom (from Schmidt [22])

What can be concluded from equation 2.1 is that the variation of velocity is proportional with 1 over the length scale, $V_{axis} \propto \frac{1}{x}$. Rajaratman [19] confirms this relation for a circular turbulent jet, which is considered as a circular jet emerging from a nozzle with a uniform velocity into a large stagnant mass of the same fluid. The jet needs to have a significantly higher velocity than the surrounding fluid, so $V_{axis} \gg V_{surrounding}$. Whenever the surrounding fluid is in motion in the direction of the jet and the jet is considered weak, the relation becomes $V_{axis} \propto \frac{1}{x^{2/3}}$ [19].

The jet could also have a certain amount of swirl in it and this affects the velocity field. The swirl causes the jet to spread more rapidly with the consequence of the velocity field decaying much faster. Most of the time the axial velocities are far more significant than the tangential velocities ($V_{axis} \gg V_{tangential}$) and the relation is $V_{axis} \propto \frac{1}{x}$. If the tangential velocities are similar to the axial velocities $V_{axis} \sim V_{tangential}$, the relation of the velocity along the axis becomes $V_{axis} \propto \frac{1}{x\sqrt{x}}$ [19].

The flow induced by a small central source located on the wall, such as the transverse thruster induced flow against a quay wall, is spreading radially outwards. This is known as axisymmetric wall jets or radial wall jet. For radial wall jet velocities, the relation is $V_{max} \propto \frac{1}{x}$ [19].

2.2.3. Efflux velocity

The efflux velocity V_0 is the maximum induced jet velocity and can be computed with equation 2.10. The efflux velocity is constant in the potential core along the region of flow establishment. The derivation of this equation comes from the momentum theory. The velocity distribution throughout the diffusing jet is related to it, see section 2.2.1 and 2.2.2.

$$V_0 = 1.6 nD_p \sqrt{K_T} \quad (2.10)$$

The thrust coefficient K_T could be obtained from the open water propeller characteristics. However, these propeller characteristics are not always available, so another more practical relation is established for the efflux velocity, see equation 2.11. Here $P_{\text{thruuster}}$ is thruster power and ρ is the density of the water.

$$V_0 = 1.17 \left(\frac{P_{\text{thruuster}}}{\rho D_{\text{thruuster}}^2} \right)^{0.33} \quad (2.11)$$

2.3. CFD modelling

Fluid dynamics describe the flow of a fluid, including liquids and gases. It can be divided into two main categories, aerodynamics (motion of air) and hydrodynamics (motion of water). The fundamental laws in these studies are the conservation laws of physics:

- *Conservation of Mass*
The mass of a fluid is conserved.
- *Conservation of Momentum*
The rate of change in momentum is equal to the sum of the forces on a fluid particle (Newton's second law).
- *Conservation of Energy*
The rate of change in energy equals the total sum of heat addition and the work done on a fluid particle (First law of thermodynamics).

Applying these laws on a fluid will give the fundamental equations of fluid dynamics. The equations for conservation of mass and the conservation of momentum for an incompressible three-dimensional Newtonian fluid with a constant temperature in vector form can be seen in equations 2.12 and 2.13 respectively.

$$\nabla \cdot \vec{u} = 0 \quad (2.12)$$

$$\frac{\partial \vec{u}}{\partial t} + (\vec{u} \cdot \nabla) \vec{u} = -\frac{1}{\rho} \nabla p + \nu \nabla^2 \vec{u} + \vec{f} \quad (2.13)$$

where:

- \vec{u} = Velocity vector [m/s]
- ρ = Density [kg/m³]
- p = Pressure [N/m²]
- ν = Kinematic viscosity (= μ/ρ) [m²/s]
- \vec{f} = Body accelerations acting on continuum, for example gravity [m/s²]

These two basic mechanical laws form a set of coupled, non-linear partial differential equations, the Navier-Stokes Equations. For most engineering problems, these equations are not analytically solvable, but for a variety of these engineering problems it is possible to obtain a computer-based approximate solution. The application of computer-based numerical methods to solve problems involving fluid flows is known as Computational Fluid Dynamics (CFD).

CFD is applicable to a wide variety of industries, because it can be more cost-effective than physical tests. However, complex flow simulations are challenging and error-prone, so it takes a lot of engineering expertise to obtain validated solutions.

The first and most important step in CFD is the analysis of the problem, find a suitable physical model and make the right assumptions and setting up all the input parameters of a flow problem correctly into a CFD program. This is the pre-processor phase in constructing a CFD model. The computational domain needs to be build up with a definition of the geometry in the region of interest. This domain needs to be subdivided into an amount of smaller non-overlapping domains: a grid of cells. This process is called meshing and is part of the pre-processor phase. The boundary conditions for cells at the domain boundary and the fluid properties need to be specified. In this pre-processing part it is required to choose the right physical phenomena to model which are linked to several assumptions. Two important assumptions have been mentioned before: the fluid is considered as incompressible and Newtonian. Incompressibility means that the density ρ of the fluid is constant and we speak of a Newtonian fluid whenever the viscosity is assumed to be constant, so independent of the amount of shear applied to the fluid. These assumptions make the set of equations easier to solve.

The second part of the CFD code is the solver, where the governing equations of fluid flow are integrated over the control volumes of the domain. These integrals are converted into a system of algebraic equations, which is called discretization. The solution of these algebraic equations is found by an iterative method.

In the third part of the CFD analysis, the post-processing, the solution of the problem is visualized. CFD packages are equipped with several tools to visualize the solution, including surface plots, vector plots and particle tracking.

2.3.1. Meshing

Splitting the flow domain into smaller sub-domains is an important part in the pre-processor phase. Poor meshing can lead to instabilities and even non-convergence, but a large number of cells can lead to a big increase in computing time. Also, the time-steps involved are of importance for the stability and convergence of the iterative solution. The dimensionless Courant number is a helpful indication for selecting the time step size. The definition of the Courant number C is shown in equation 2.14. Here is Δt the time step, u is the velocity and Δx is the length of a cell.

$$C = \frac{u\Delta t}{\Delta x} \quad (2.14)$$

The Courant number relates the time step to the interval length of each spatial coordinate. A maximum Courant number limits the speed that information can travel in the physical space and is especially related to the advection term of the Navier-Stokes equations. An explicit unsteady solver with a Courant number above one will be unstable. Implicit solvers have fewer issues with instabilities because these are generally more stable. This is due to the fact that explicit solvers only use information from the last time step, but implicit solvers use unknown information from the current time step as well. Choosing the Courant number equal to 1, means that a convected particle can travel one cell distance Δx in a single time step Δt .

2.3.2. Wall functions

During the meshing process, extra attention is needed to model the big gradients of velocity close to a wall, see figure 2.7. The typical velocity profile approaches zero on the wall and free stream far away from the wall. The gradients near the wall get steeper and steeper and to capture these gradients a fine mesh is needed here locally. This means that the cells need to get thinner and thinner in the direction normal to the wall to accurately resolve those steep gradients by a piece-wise linear approach.

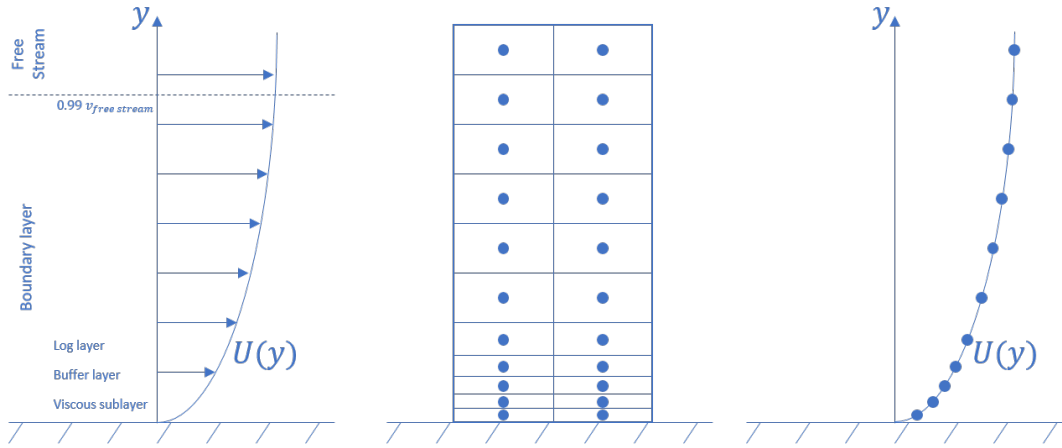


Figure 2.7: Fine grid resolution is needed near the wall to accurately solve the steep gradients

Instead of applying the piece-wise linear approach, it is also possible to have a non-linear approach, which allows for much larger cells. Wall functions are empirically obtained functions that fit the observed behavior of the flow of a developed boundary layer over a flat plate. In figure 2.8, the non-dimensional tangential velocity u^+ is plotted against the non-dimensional wall normal distance y^+ and the circles shown the observed flow behavior from a Direct Numerical Simulation (DNS), which is the desired solution, see section 2.3.3 for more information. The orange lines are the empirical function that can fit parts of DNS flow behavior. The profile is commonly split into three regions, the viscous sub-layer for $y^+ < 5$, a buffer layer for $5 < y^+ < 30$ and the log-law region for $30 < y^+ < 200$. Note that the horizontal axis is in log scale, this means that the linear blue line has a logarithmic profile and the blue line which fits the red line well in the viscous sub-layer is actually linear.

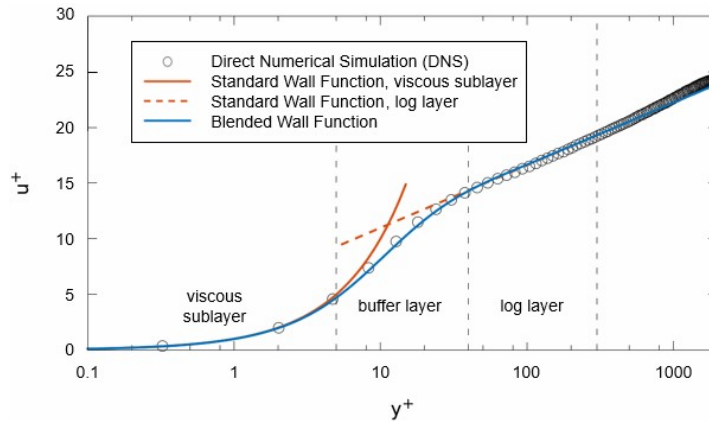


Figure 2.8: Law of wall (from Simcenter STAR-CCM+ [24])

The standard wall functions for the viscous sub-layer and the log layer are shown in equation 2.15 and 2.16 respectively. Where κ and E are empirical coefficients: 0.42 and 9 in STAR-CCM+ [24].

$$u^+ = y^+ \quad y^+ < 5 \quad (2.15)$$

$$u^+ = \frac{1}{\kappa} \log(Ey^+) \quad 30 < y^+ < 200 \quad (2.16)$$

In the buffer layer between the log-law region and the viscous sub-layer, neither of the orange lines give a good representation of the observed behavior. To ensure that the wall stress is calculated correctly, it is recommended to place the y^+ value either in the viscous sub-layer or in the log-law region, use $y^+ < 5$ or $30 < y^+ < 200$ respectively. The y^+ value is the dimensionless wall distance and is defined in equation 2.17. The dimensionless wall-tangential velocity component u^+ is defined in equation 2.18.

$$y^+ = \frac{\rho u_* y_{wall}}{\mu} \quad (2.17)$$

$$u^+ = \frac{u}{u_*} \quad (2.18)$$

Where:

y^+ = non dimensional wall distance [-]

u^+ = non dimensional wall-tangential velocity component [-]

ρ = density [kg/m^3]

u_* = velocity scale which is representative of the flow velocity in the near wall region [m/s]

y_{wall} = wall distance [m]

μ = dynamic viscosity [Ns/m^2]

u = wall-tangential component of velocity vector [m/s]

If we want the y^+ value outside the buffer layer, then distance to the wall y_{wall} needs to be chosen wisely. One uncertainty here is the representative flow velocity near the wall u_* , because this parameter is unknown beforehand, but can be approximated with a flat plate boundary layer model. This model starts with calculating the Reynolds number Re , defined in equation 2.19.

$$Re = \frac{\rho UL}{\mu} \quad (2.19)$$

The Reynolds number is a dimensionless number which represents the ratio between the inertial forces and the viscous forces. Here ρ is the density, U is the free stream velocity (characteristic velocity), L is the characteristic length of the geometry that is modelled and μ is the dynamic viscosity. These parameters are mostly known in advance of the CFD calculation, so the Reynolds number can be calculated beforehand.

The Reynolds number is used to estimate the skin friction coefficient c_f . There are many empirical $c_f - Re$ relations available in literature, such as the International Towing Tank Conference (ITTC) [12] relation, equation 2.20, which is well known in the marine industry. In STAR-CCM+, the Blasius friction factor correlation in equation 2.21 is used [24].

$$c_f = \frac{0.075}{(\log_{10}(Re) - 2)^2} \quad (2.20) \quad c_f = 0.0791Re^{-0.25} \quad (2.21)$$

The wall shear stress τ_w is calculated with this skin friction coefficient c_f , equation 2.22.

$$\tau_w = \frac{1}{2} \rho U^2 c_f \quad (2.22)$$

This wall shear stress τ_w is used to calculate representative velocity near the wall u_* , equation 2.23.

$$u_* = \sqrt{\frac{\tau_w}{\rho}} \quad (2.23)$$

Now the equation of y^+ , equation 2.17, can be rearranged to calculate the wall distance, see equation 2.24. The value for y^+ can now be chosen to be $y^+ < 5$ or $30 < y^+ << 200$.

$$y_{wall} = \frac{y^+ \mu}{u_* \rho} \quad (2.24)$$

The wall distance y_{wall} can be used for the initial guess of the wall adjacent cell sizes. The base size of a cell is the height of the whole cell, so $2y_{wall}$, see figure 2.9.

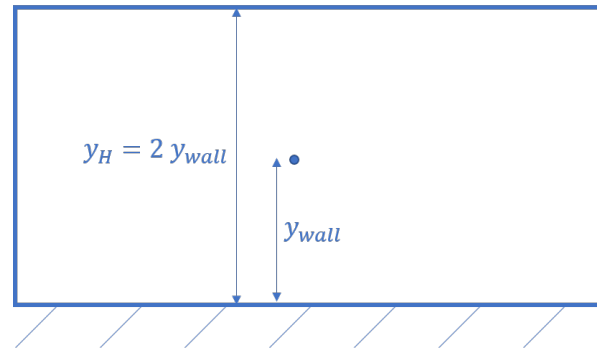


Figure 2.9: Base size y_H and wall distance y_{wall} definition

After the CFD simulation has run, the y^+ needs to be checked and there is a possibility that the y^+ value is still in the undesired buffer region. If this is the case in the region of interest, the cell size needs to be adjusted or blended wall functions need to be applied, which cover all three of the sub-layers.

2.3.3. Turbulence Modelling

There are two states of flow and they are radically different from one another, the two states are: laminar flow and turbulent flow. Laminar flow is characterized by a smooth velocity field in space and time, as the turbulent flow is chaotic and contains quasi-random fluctuations in space and time. These fluctuations are due to instabilities that grow until nonlinear interaction breaks them down into eddies that dissipate by viscosity. The state of the flow depends on several parameters, such as the velocity U , the viscosity μ and the characteristic length L . These parameters are combined in the dimensionless Reynolds number, see equation 2.19.

Laminar flow typically occurs at low to moderate Reynolds numbers, so the viscous forces are dominant. On the other hand, turbulence occurs at the opposite limit of high Reynolds numbers, with dominant inertial forces.

In a turbulent flow many eddy sizes exist. The largest eddies transport energy to the smaller eddies and the smaller eddies are dissipated into heat due to the viscosity. Correctly modelling the turbulence is of great importance in obtaining reliable CFD results. Generally, three main approaches can be used to simulate turbulence:

- **Direct Numerical Simulation (DNS)**

The Direct Numerical Simulation resolves a turbulent flow by solving the Navier-Stokes equation directly, which makes this method unrivalled in accuracy. However, the computational costs are extremely high. Due to the wide range of temporal and spatial scales, the mesh size and time steps need to be small. This makes this approach practically inapplicable for complex fluid structures.

- **Large Eddy Simulation (LES)**

During a Large Eddy Simulation the largest scales of turbulence are resolved directly, while the smaller scales are spatially filtered out. The filtering is done based on the mesh size; the dissipation of the flow scales smaller than the grid size are modelled by a sub grid model of extra viscosity.

- **Reynolds-Averaged Navier Stokes (RANS)**

In the Reynolds-Averaged Navier Stokes approach an averaging operation is applied to the Navier-Stokes equation to obtain mean values of the fluid flow. These RANS equations are similar to the original Navier Stokes equations but have an additional unknown Reynolds stress term in the momentum equations. This Reynolds stress term requires additional modelling, which can be done by many different turbulence models. These turbulence models are simplified equations that predict the statistical evolution of turbulent flows.

RANS modelling is the most common and widespread approach in industrial applications but has its limitations due to modelling assumptions. Generally it can be said that the DNS approach resolves the physics, and the RANS approach is modelling the physics, but computational costs of DNS are much higher compared to RANS, see figure 2.10.

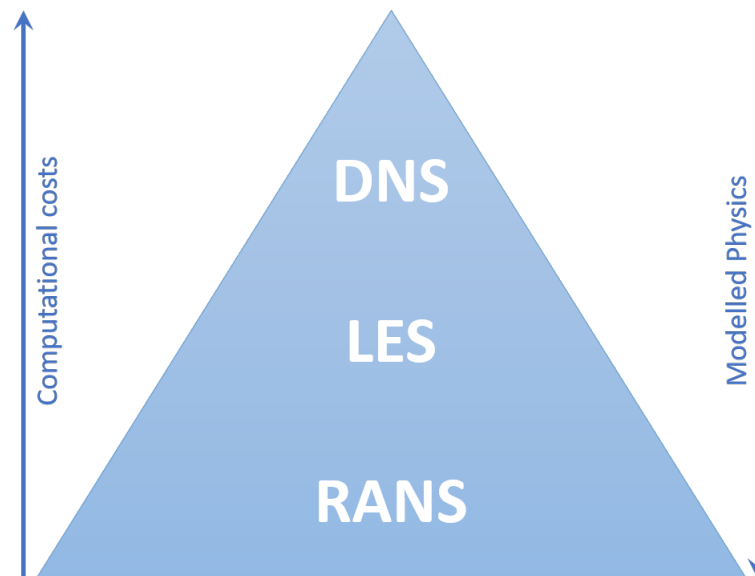


Figure 2.10: Turbulence models in CFD

Since the numerical model of the vertical quay wall is quite complex and with high Reynolds numbers, it is chosen to use the RANS equations with a suitable turbulence model to keep the computing times moderate. Therefore, the RANS equations are more thoroughly explained in the next section.

2.3.4. RANS

The turbulent flow is modelled as a time averaged value $\bar{\phi}$ plus a fluctuating value $\phi'(t)$, so the turbulent flow is modelled with $\phi(t) = \bar{\phi} + \phi'(t)$. This principle is called the Reynolds decomposition, see figure 2.11. The time-average of the fluctuating part is by definition zero, $\overline{\phi'(t)} = 0$. This Reynolds decomposition is applied to the velocity and pressure term, $u(t) = \bar{u} + u'(t)$ and $p(t) = \bar{p} + p'(t)$ respectively, in the Navier-Stokes equations 2.12 and 2.13.

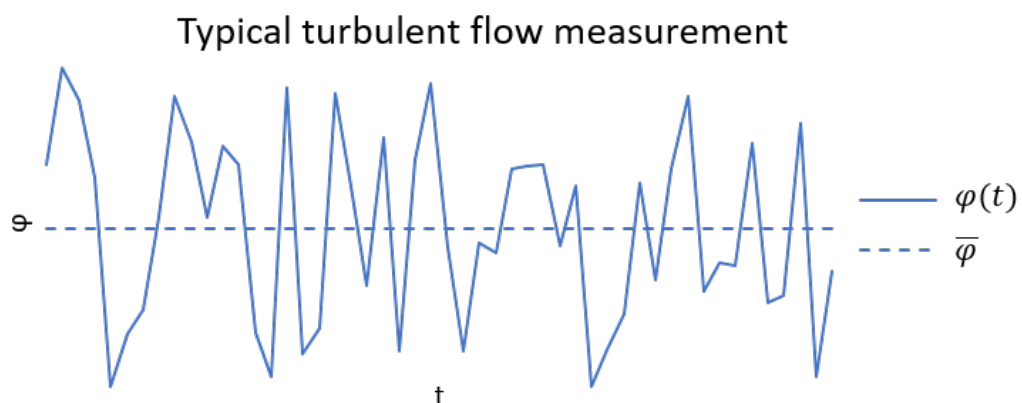


Figure 2.11: Reynolds decomposition in typical flow measurement

Conservation of mass:

$$\frac{\partial u_i}{\partial x_i} = 0 \quad (2.25)$$

Substitute $u_i = \bar{u}_i + u'_i$:

$$\frac{\partial}{\partial x_i} (\bar{u}_i + u'_i) = 0 \quad (2.26)$$

Take the time average of the whole equation:

$$\lim_{T \rightarrow \infty} \frac{1}{T} \int_{t_0}^{t_0+T} \frac{\partial}{\partial x_i} (\bar{u}_i + u'_i) dt = 0 \quad (2.27)$$

$$\frac{\partial}{\partial x_i} (\overline{\bar{u}_i + u'_i}) = 0 \quad (2.28)$$

Since the average of the average $\overline{\bar{u}_i}$ is still the average \bar{u}_i and the average of the fluctuating part is zero by definition $\overline{u'_i} = 0$, the equation becomes:

$$\frac{\partial}{\partial x_i} (\bar{u}_i) = 0 \quad (2.29)$$

The average flow field obeys the continuity and if equation 2.29 is substituted back into equation 2.26:

$$\frac{\partial u'_i}{\partial x_i} = 0 \quad (2.30)$$

So the unsteady velocity fluctuations also obeys continuity.

Conservation of momentum:

Another expression of the conservation of momentum, without the body forces is:

$$\frac{\partial u_i}{\partial t} + \frac{\partial}{\partial x_j} (u_j u_i) = -\frac{1}{\rho} \frac{\partial p}{\partial x_i} + \nu \frac{\partial^2 u_i}{\partial x_j^2} \quad (2.31)$$

Substitute $u = \bar{u} + u'$ and $p = \bar{p} + p'$ and take the time average:

$$\frac{\partial \overline{\bar{u}_i + u'_i}}{\partial t} + \frac{\partial}{\partial x_j} (\overline{(\bar{u}_j + u'_j)(\bar{u}_i + u'_i)}) = -\frac{1}{\rho} \frac{\partial \overline{\bar{p} + p'}}{\partial x_i} + \nu \frac{\partial^2 \overline{\bar{u}_i + u'_i}}{\partial x_j^2} \quad (2.32)$$

Since $\overline{\bar{u}_i} = \bar{u}_i$, $\overline{u'_i} = 0$, $\overline{\bar{p}} = \bar{p}$ and $\overline{p'} = 0$ the equation becomes:

$$\frac{\partial \bar{u}_i}{\partial t} + \frac{\partial}{\partial x_j} (\overline{\bar{u}_j \bar{u}_i + \bar{u}_j u'_i + u'_j \bar{u}_i + u'_j u'_i}) = -\frac{1}{\rho} \frac{\partial \bar{p}}{\partial x_i} + \nu \frac{\partial^2 \bar{u}_i}{\partial x_j^2} \quad (2.33)$$

The nonlinear convective term in the equation can be simplified, because the first convective term $\frac{\partial \overline{\bar{u}_j \bar{u}_i}}{\partial x_j} = \bar{u}_j \frac{\partial \bar{u}_i}{\partial x_j}$ due to continuity. The second and third term are zero, $\frac{\partial \overline{\bar{u}_j u'_i}}{\partial x_j} = 0$ and $\frac{\partial \overline{u'_j \bar{u}_i}}{\partial x_j} = 0$, because $\bar{u} = const$ and $\overline{u'} = 0$. The fourth convective term $\overline{u'_i u'_j}$ is the Reynolds stress term (the Reynolds-stress tensor divided by the density). This term incorporates the effects of turbulent motions on the mean stresses and results in diffusion of momentum. The Reynolds stress tensor is symmetric, the components on the diagonal are normal stresses and the off-diagonal terms are shear stresses.

The Reynolds-Averaged Navier-Stokes equations without the external body forces become:

$$\frac{\partial \bar{u}_i}{\partial t} + \bar{u}_j \frac{\partial \bar{u}_i}{\partial x_j} = -\frac{1}{\rho} \frac{\partial \bar{p}}{\partial x_i} + \nu \frac{\partial^2 \bar{u}_i}{\partial x_j^2} - \frac{\partial}{\partial x_j} (\overline{u'_i u'_j}) \quad (2.34)$$

$$\frac{\partial \bar{u}_i}{\partial x_i} = 0 \quad (2.35)$$

The Reynolds stress term $\overline{u'_i u'_j}$ is shown in equation 2.36 in Cartesian coordinates. It is in this form not really a stress term, because the dimension is now velocity squared. If the whole equation 2.34 is multiplied with the density, the Reynolds stress term unit becomes also a stress. This term in the RANS equations accounts for the turbulent shear but has introduced 6 additional unknown stresses into the problem, due to the fact that the fluctuating velocity terms are not known. Therefore three unknown normal stresses $\tau_{xx} = -\rho \overline{u'^2}$, $\tau_{yy} = -\rho \overline{v'^2}$ and $\tau_{zz} = -\rho \overline{w'^2}$ and three unknown shear stresses $\tau_{xy} = \tau_{yx} = -\rho \overline{u'v'}$, $\tau_{xz} = \tau_{zx} = -\rho \overline{u'w'}$ and $\tau_{yz} = \tau_{zy} = -\rho \overline{v'w'}$ are introduced, which is called the closure problem.

$$\tau''_{ij} = - \begin{bmatrix} \overline{u'^2} & \overline{u'v'} & \overline{u'w'} \\ \overline{v'u'} & \overline{v'^2} & \overline{v'w'} \\ \overline{w'u'} & \overline{w'v'} & \overline{w'^2} \end{bmatrix} \quad (2.36)$$

These unknown Reynolds stresses need to be modelled to close the equations. The common approach is to assume that the Reynolds Stresses are proportional to the mean flow quantities. The most common on used in industry is the Boussinesq approximation, equation 2.37.

$$-\rho \overline{u'_i u'_j} = \mu_t \left(\frac{\partial \bar{u}_i}{\partial x_j} + \frac{\partial \bar{u}_j}{\partial x_i} \right) - \frac{2}{3} \rho k \delta_{ij} \quad (2.37)$$

The k in this equation is the turbulent kinetic energy, which is the kinetic energy of the fluctuating velocities in x- y- and z-direction u' , v' and w' , see equation 2.38.

$$k = \frac{1}{2} (\overline{u'^2} + \overline{v'^2} + \overline{w'^2}) \quad (2.38)$$

The μ_t in the Boussinesq hypothesis (equation 2.37) is the eddy viscosity, which relates the Reynolds stresses to the mean velocity gradients. It is necessary to model this eddy viscosity μ_t in some way, so the system of equations can be closed. This is done with the use of a turbulence model. There are several turbulence models developed and they all vary in accuracy and in computation time.

In short, the Reynolds Stress term $-\rho \overline{u'_i u'_j}$ in the RANS equations needs to be modelled as a function of the mean flow, removing any reference to the fluctuating part of the velocity. This is known as the closure problem and Boussinesq proposed to do this by introducing the concept of the eddy viscosity μ_t . This eddy viscosity is subsequently modelled by one of the many developed turbulence models. They all vary in accuracy and computation time and some of them are discussed with their advantages and disadvantages below.

Mixing length model

The older RANS turbulence models used the mixing length approach to calculate the eddy viscosity. The mixing length physically represents an indicative size of the turbulent eddies that exist in the flow. The Prandtl mixing length hypothesis supposes that the maximum size of the eddies is limited by the presence of a wall. This means that the mixing length and so the eddy viscosity is only depending on the fixed distance to the wall.

Since the turbulence is convected and diffused throughout the flow and definitely not static and fixed which is implied by this hypothesis, this approach could be improved. Therefore, the transport equations are introduced.

$k - \varepsilon$ Turbulence model

The $k - \varepsilon$ turbulence model uses two transport equations, one for the turbulent kinetic energy κ and one for the dissipation rate ε . Once the transport equations are solved, the eddy viscosity μ_t can be computed as a function of k and ε . With the known μ_t , the Boussinesq approximation can be used to come up with the Reynolds stresses. The governing equations of the $k - \varepsilon$ turbulence model can be seen in section 2.3.5. The $k - \varepsilon$ turbulence model is widely used for high Reynolds number situations in

The adjustable constants $C_\mu, \sigma_k, \sigma_\varepsilon, C_{1\varepsilon}$ and $C_{2\varepsilon}$ are empirical determined for the standard $k - \varepsilon$ model:

$$C_\mu = 0.09 \quad \sigma_k = 1.00 \quad \sigma_\varepsilon = 1.30 \quad C_{1\varepsilon} = 1.44 \quad C_{2\varepsilon} = 1.92$$

The σ_k and σ_ε are Prandtl numbers and connect the rate of diffusion of k and ε to the eddy viscosity μ_t . The production rate k and destruction rate ε are related to each other: the dissipation rate ε is large whenever the production rates k are large. The constants $C_{1\varepsilon}$ and $C_{2\varepsilon}$ regulate the correct proportion between the terms in the k - and ε -equations.

To account for the viscosity in the viscous sub layer which is reducing the effective size of the eddies, it is necessary to have some way of damping the dissipation rate close to the wall. This is done with the low-Re formulation of the $k - \varepsilon$ model and works based on damping functions. There are various damping functions for the standard $k - \varepsilon$ model, the original damping functions from Launder and Sharam [13] are shown in equation 2.42, 2.43 and 2.44.

$$f_1 = 1 \quad (2.42)$$

$$f_2 = 1 - 0.3 \exp(-Re_T^2) \quad (2.43)$$

$$f_\mu = \exp\left(\frac{-3.4}{(1 + (Re_T/50))^2}\right) \quad (2.44)$$

Where the turbulent Reynolds number Re_T is defined as in equation 2.45. Near the wall it is expected that the turbulent kinetic energy k will be small and the dissipation rate ε high, so the turbulent Reynolds number will be small. This means that the viscous forces are dominating the turbulent forces.

$$Re_T = \frac{\rho k^2}{\mu \varepsilon} \quad (2.45)$$

The specific damping functions f_1, f_2 and f_μ are applied to the model coefficients $c_{1\varepsilon}, c_{2\varepsilon}$ and C_μ . This means that the eddy viscosity is in the low-Re formulation computed with equation 2.46.

$$\mu_t = f_\mu C_\mu \frac{\rho k^2}{\varepsilon} \quad (2.46)$$

In a cell far away from the wall, so with high Reynolds number, f_μ is going to tend to one, so we have the original form of the eddy viscosity. In a situation near the wall, the eddy viscosity is reduced, which is physically expected.

2.3.6. Turbulence Intensity

The turbulence intensity is an important parameter for the design of bottom protection at a quay wall. The turbulence intensity is defined by equation 2.47 [14].

$$I = \frac{\sqrt{\frac{1}{3}(\overline{u'u'} + \overline{v'v'} + \overline{w'w'})}}{U_{ref}} = \frac{\sqrt{\frac{2}{3}k}}{U_{ref}} \quad (2.47)$$

Where:

I = Turbulence intensity [-]

$\overline{u'u'}$ = X-component of turbulence fluctuations [m/s]

$\overline{v'v'}$ = Y-component of turbulence fluctuations [m/s]

$\overline{w'w'}$ = Z-component of turbulence fluctuations [m/s]

k = Turbulent kinetic energy [m²/s²]

U_{ref} = Local velocity magnitude $\left(U_{ref} = \sqrt{u_x^2 + u_y^2 + u_z^2}\right)$ [m/s]

2.3.7. Propeller model

The propeller of the bowthruster could be modelled in a CFD code in several ways. One option is to include the propeller in a moving reference frame. This means that the actual propeller geometry is rotating in the CFD code. This requires a detailed resolution of the blade geometry, which leads to a large number of cells, so longer computing times. Another simplified option is to simulate the propeller by adding volumetric body forces to the momentum equations, which is known as the Virtual Disk model. The body forces created by the propeller are distributed over a cylindrical disk volume. So, the virtual disk model has influence in the flow field by adding an extra momentum source, which is divided over the virtual disk. The big advantage of the Virtual Disk model is that the exact geometry of the propeller does not have to be resolved, which saves computing time. There are three different Virtual Disk model approaches within STAR-CCM+: The Body Force Propeller method, the Blade Element Method and the 1D Momentum Method.

The 1D Momentum theory is mainly used to model the effects of a wind turbine and the Blade Element Method is primarily designed to model the effects on the flow field of a helicopter rotor. The Body Force Propeller Method is suitable for simulating marine propellers because this method models the effects of thrust and torque of a propeller. As this Body Force Method is applied in this thesis it is further explained.

The Body Force Method imposes a uniform volume force distribution f_b , which can vary in radial direction, over the cylindrical virtual disk. The radial distribution of the force is determined based on the Goldstein optimum, equations 2.48 - 2.52.

$$f_{bx} = A_x r^* \sqrt{1 - r^*} \quad (2.48) \quad f_{b\theta} = A_\theta \cdot \frac{r^* \sqrt{1 - r^*}}{r^* (1 - r'_h) + r'_h} \quad (2.49)$$

$$r^* = \frac{r' - r'_h}{1 - r'_h} \quad (2.50) \quad r'_h = \frac{R_H}{R_p} \quad (2.51) \quad r' = \frac{r}{R_p} \quad (2.52)$$

Where:

- f_{bx} = Body force component in axial direction per unit volume [N/m³]
- $f_{b\theta}$ = Body force component in tangential direction per unit volume [N/m³]
- r = Radial coordinate [m]
- R_H = Hub radius [m]
- R_p = Propeller tip radius [m]
- A_x, A_θ = Constants [N/m³]

The constants A_x and A_θ are computed as equation 2.53 and 2.54.

$$A_x = \frac{105}{8} \cdot \frac{T}{\pi \Delta (3R_H + 4R_p) (R_p - R_H)} \quad (2.53) \quad A_\theta = \frac{105}{8} \cdot \frac{Q}{\pi \Delta R_p (3R_H + 4R_p) (R_p - R_H)} \quad (2.54)$$

Where:

- T = Thrust [N]
- Q = Torque [Nm]
- Δ = Virtual disk thickness [m]

The virtual disk model requires certain input parameters, such as the position of the disk, the direction of the thrust and the propeller handedness. Another important input parameter is to determine the operation point on the open water propeller diagram. This propeller performance curve needs to be specified with the dimensionless thrust coefficient K_T , the torque coefficient K_Q as a function of the advance ratio J , defined in equations 2.55, 2.56 and 2.57.

$$K_T = \frac{T}{\rho n^2 D_p^4} \quad (2.55) \quad K_Q = \frac{Q}{\rho n^2 D_p^5} \quad (2.56) \quad J = \frac{V_A}{n D_p} \quad (2.57)$$

Where:

- K_T = Thrust coefficient [-]
- K_Q = Torque coefficient [-]
- n = Rotation rate of propeller [rps]
- V_A = Advance velocity of propeller [m/s]
- D_p = Propeller diameter [m]

The operating point can be chosen, for which the simulation is performed, by specifying either the rotation rate n , the thrust T or the torque Q of the propeller.

2.4. TU Delft Theses

In this section the most important findings from previous MSc theses from the TU Delft are discussed regarding thruster jets at quay walls.

De Jong [9] concludes that the propeller jet can be modelled in the CFD program PHOENICS by adding a swirl and a core to the jet. The radius of the core of the jet needs to be $0.3D_p$ and the ratio between the tangential and axial velocities at the propeller needs to be 0.8. The standard $k - \varepsilon$ model gives good results for modelling the turbulence further away from the propeller. The obtained bottom velocities at a vertical quay wall are about 1,5 times bigger than equation 2.6 from the PIANC guidelines prescribes.

Van der Laan [28] models the propeller in two ways: as a simple water jet and as a 'fan' in the CFD program Phoenix. The 'fan' is comparable to a virtual disk because it works as an impulse source. The turbulence is also modelled with the $k - \varepsilon$ model. He recommends modelling the inlet of the tunnel thruster with some attention because it could be of influence. He also recommends varying the keel and quay clearance to provide more insight in the flow field. The numerical model did not produce an accurate representation of the outcome of the physical model, but not much can be said about the whole flow field as only three point measurement were made.

Nielsen [15] builds on to the research of Van der Laan and especially improves the physical model. The numerical model shows a similar flow pattern as the physical model in his work. The order of magnitude is also the same. In the area under the ship, the flow of the numerical model shows a different behavior than the flow of the physical model. This should be further investigated.

Van Blaaderen [2] did a sensitivity analysis and concludes that a change in turbulence model is of little influence of the results of the numerical model and justifies the use of the $k - \varepsilon$ model. The keel clearance on the other hand has a big influence on the velocity distribution. Smaller keel clearance results in a less symmetric flow distribution on the bottom. In addition, the model is insensitive to a deviation in wall roughness and the turbulent energy level is higher for the physical model than for the numerical model.

Van Blaaderen argues that the most important aspect of the numerical model is to model the outflow of the bowthruster correctly. The analytical model of Van Blaaderen predicts that the low-velocity core behind a thruster collapses within a distance between $2D_p - 3D_p$, but recommends to measure the situation beyond these distances. To model a similar outflow of the bowthruster, Van Blaaderen adds a center plate to the propeller to simulate the propeller hub.

Van den Brink [27] used the open source CFD package OpenFOAM in combination with Matlab to develop a 3D numerical model in which he simulates the scour due to bow thrusters over time. A Boundary adjustment technique is successfully applied to move the mesh near the scoured bed. The turbulence is included with a Realizable $k - \varepsilon$ model in OpenFOAM. The bow-thruster is modelled by putting a circular velocity field on the boundary of the numerical domain with a constant velocity component of 8 m/s. The radial spreading of this flow underestimates the actual radial spreading of a bow thruster jet, due to the absence of the swirling flow and vorticity induced by the propeller. This resulted in an overestimation of near bed velocities near the quay, and an underestimation of the near bed velocities further away from the quay. This deviation becomes more significant for an increasing quay clearance.

One recommendation of Van den Brink was to improve the modelling of the propeller to include the effect of radial spreading and turbulence on the flow. Another improvement could be made with the mesh near the bed in order to obtain sufficient low y^+ values to involve near wall treatment in the simulation.

2.5. Conclusive remarks from literature

This literature review is meant to define the knowledge gap. A lot of research into the free jet flow and its velocity field has been performed in the past. In addition, previous research came up with equations for the bottom velocity at quay walls. Since the field measurements of 2019 with the MTS Vorstenbosch were not in line with the PIANC guidelines, it is interesting to check whether these equations are still valid. A numerical model could help to verify the field measurements and the current PIANC equations. If it turns out that these equations need to be updated, the findings from Rajaratnam could be used to find more suitable correlations.

In this research, the choice is made to use the RANS equations, because these are preferred over the DNS or LES method due to their advantageous computing time. Since the $k - \varepsilon$ model is commonly used in industry to simulate the jet of a marine propeller, this model will be studied in this thesis, along with other turbulence models. Different turbulence models will be compared to each other in a later stage of the thesis, hereafter a conclusion can be made for the best suited turbulence model for this specific application.

The propeller will not be modelled with a moving reference frame, because the exact geometry of the bow thruster propeller of the MTS Vorstenbosch is not available and the computing time will be not suited for this project duration. Therefore, the propeller is modelled in this research with a virtual disk. The propeller in the bow thruster will be modelled with the Body Force Method, which adds momentum and swirl to the water. This virtual disk method is best suited for marine applications.

3

Virtual disk

This chapter shows how the virtual disk is implemented in the CFD code and how this virtual disk model is subsequently validated based on the paper of Wei [36] and the PIANC report 180 [17]. A Convergence study is done in section 3.4 and four different turbulence models are compared to each other in section 3.5.

3.1. Reference experiment

The virtual disk will be validated based on velocity data from Wei [36]. This paper experimentally investigated the mean and turbulent flow fields of a propeller impinging on a vertical quay wall using a Particle Image Velocimetry (PIV) technique. The tests of Wei were conducted in a recirculating flume tank with dimensions of 11 m length, 0.6 m width and 0.6 m depth. Due to the placement of a plate with the dimensions of 0.6 m height and 0.6 m width to model the quay wall, the flow was not recirculating anymore. Wei performed the test for a varying wall clearance, i.e., longitudinal distance between the propeller and the vertical wall, by varying the longitudinal position of the propeller. The wall clearances that were tested are $1D_p$, $2D_p$, $3D_p$ and $4D_p$. The characteristics of the five-bladed Wageningen B-series propeller can be found in table 3.1.

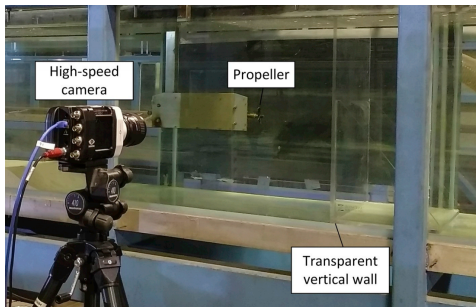


Figure 3.1: Photo of experimental setup of Wei (from Wei [36])

Propeller diameter D_p	0.075 m
Hub diameter D_h	0.01 m
Revolutions per minute n	545 rpm
Thrust coefficient K_T	0.46
Torque Coefficient K_Q	0.06
Advance Ratio J	0

Table 3.1: Propeller characteristics

3.2. CFD implementation

The propeller is modelled in STAR-CCM+ with the Body Force Propeller Method. First the domain is defined: It is chosen to use a rectangular box with a cross section of 0.6 m by 0.6 m, which is identical to the dimension of the PIV experiment of Wei. The length of the domain is chosen to be 1 m, which is sufficient to fit in all the different wall clearances with an additional margin. The inlet side of the domain is relatively far away, to make sure that the propeller induced flow is negligible over there and it is modelled with a pressure outlet boundary condition where the pressure is equal to the atmospheric pressure: 1.01325 bars. On the other side, the wall is modelled with a no-slip boundary condition. The side walls are modelled with a no-slip wall boundary condition as well, with an exception for the free surface, this boundary is modelled with a slip wall.

The trimmer mesh option in STAR-CCM+ is applied with certain volumetric controls, which can make the mesh finer at the locations of interest, in this case the area behind the propeller. The prism layer mesher is used to include the effects of the boundary layer. The mesh used can be seen in figure 3.2 with the different locations of the virtual disk. The total number of cells is around 3.9 million.

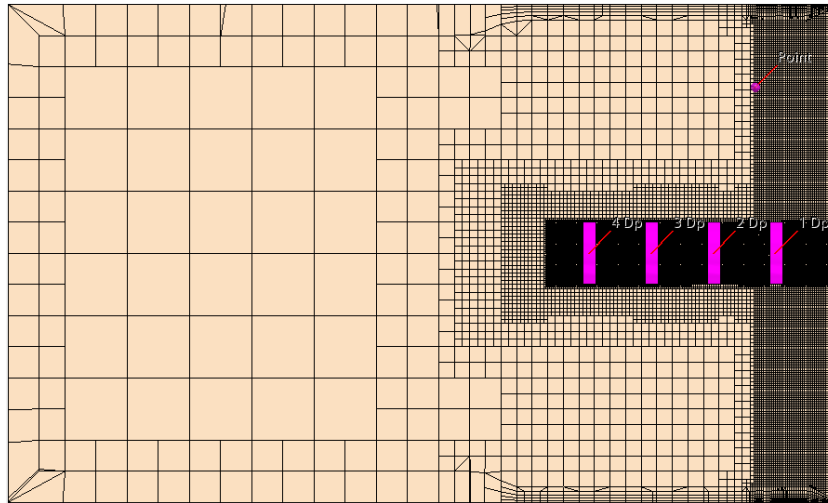


Figure 3.2: Mesh on a section for the simulation of the Wei experiments

The virtual disk has the same dimensions as the propeller in Wei; the inner diameter, which represents the influence of the hub, is equal to 1 cm and the outer diameter is 7.5 cm. The thickness of the virtual disk is chosen to be equal to 0.015 m. The disk needs a certain thickness to divide the momentum over a certain number of cells in the direction of its thickness. With the chosen mesh size in the volume control, there are 10 cells over the thickness of the virtual disk. Normally a propeller curve is necessary to model the propeller, but since the ship is considered stationary, the bollard pull conditions are satisfied ($v_a = 0$). This means that only one thrust coefficient K_T and one torque coefficient K_Q needs to be implemented. With equation 2.55 and a known rotation rate n , the propeller thrust can be calculated. Table 3.1 shows an overview of the implemented values in STAR-CCM+.

The inflow of the propeller is specified with a constant inflow value of 0 m/s and the propeller handedness is left-handed. The implicit unsteady solver is used in the CFD in combination with the segregated flow solver and the k-epsilon turbulence model. The default solver settings in STAR-CCM+ have not been adjusted. Since an implicit unsteady solver with a time step of 0.001 seconds is used, a monitor is placed at a point in the top right corner to monitor the convergence, see point in figure 3.2. When the velocity becomes constant over time at one point, the steady state is assumed to be reached.

3.3. Results

The obtained velocity fields for the four different wall distances are shown in figure 3.3. The 2D velocity magnitude is plotted: $\sqrt{v_x^2 + v_y^2}$, which is obtained with a field function in STAR-CCM+. The velocity fields from Wei are shown in figure 3.4, which is also a 2D velocity, because the PIV measurement could only measure 2D velocities. The 2D streamlines are also added in the figures to help visualize the flow field.

At a first glance the pictures look quite similar, but with a critical look some differences stand out. The jet spreads out more radially in the PIV experiments of Wei in comparison with the CFD results, especially for the small wall clearances. The jet spreads out due to the presence of the wall. In the experiments of Wei, the spreading of the jet starts directly behind the propeller. It looks like the virtual disk in the CFD model is forcing the jet to start in axial direction, i.e., the CFD model adds relatively too much momentum in the axial direction compared to the radial direction. As a result, the 2D streamlines

of the jet only start to deflect closer to the wall. The re-circulation of the streamlines inside the jet is also much more visible in the experiment of Wei, especially for the smaller wall clearances. In the CFD simulation the circulation is only to be noted in the $1D_p$ situation. For the other wall clearances, there is not enough space within the jet for re-circulation in these CFD results.

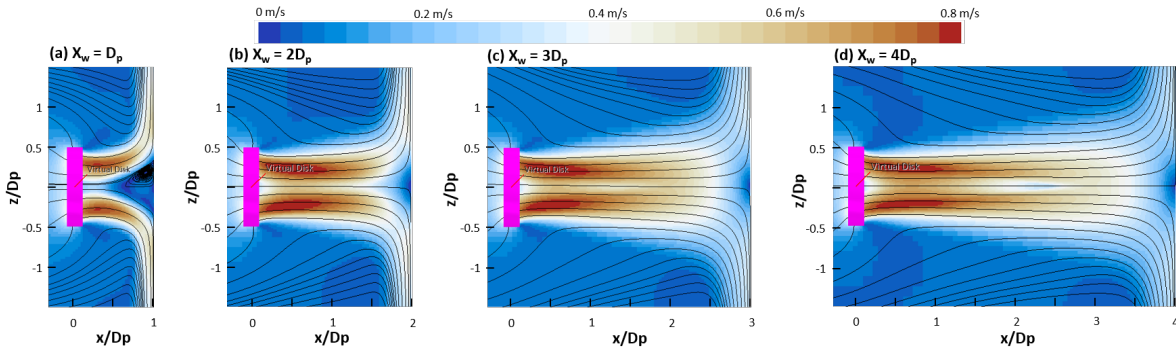


Figure 3.3: Velocity field obtained from CFD for different wall clearances

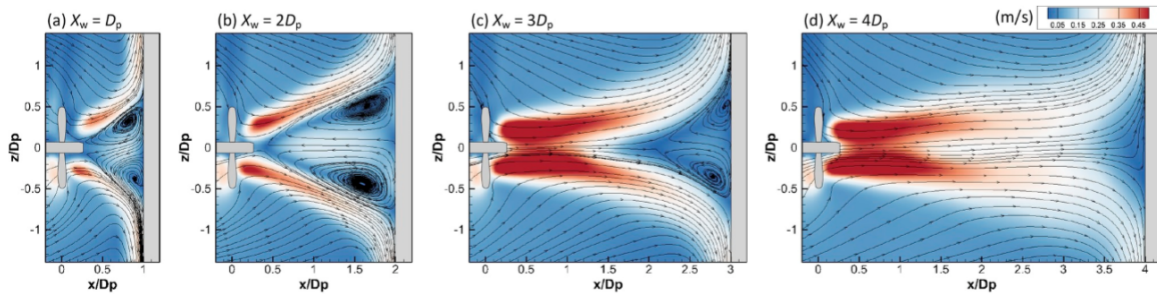


Figure 3.4: Velocity field obtained from Wei [36] for different wall clearances

To make this qualitative validation more quantitative, the maximum velocities obtained in the CFD analysis are compared to the efflux velocities from the PIV measurements in table 3.2.

	$1D_p$	$2D_p$	$3D_p$	$4D_p$
Maximum 2D velocity CFD (Constant inflow) [m/s]	0.778	0.813	0.814	0.830
Wei Efflux velocity [m/s]	0.47	0.52	0.59	0.60
Theoretical Efflux velocity [m/s]	0.74	0.74	0.74	0.74

Table 3.2: Velocity comparison

Generally, it can be said that the velocities of the CFD model are higher than the velocities from the Wei experiment. The table also shows the theoretical efflux velocity from PIANC [17]. This is a constant value for a varying wall clearance because the formula is valid for free flow conditions. This means without any interference of a wall. However, this efflux velocity is subsequently used to calculate the theoretical bottom velocities of the flow field with the interference of a quay wall. Especially the Wei experiment shows large differences in the efflux velocity between the different wall clearances; over 25% differentiation between $1D_p$ and $4D_p$.

The two main discrepancies of the virtual disk in the CFD model in comparison with the propeller in the experiment are the velocity and the spreading of the jet. The velocities are higher for the virtual disk and there is less spreading of the jet, in comparison with the experiment of Wei. It is expected that for a ducted propeller, which is the case for the simulations with the Vorstenbosch in the next chapters of this thesis, the spreading will be less pronounced. The expectation is that the flow out of the tunnel of the Vorstenbosch will be more uniform.

In the actual model of the tunnel thruster, the specific thrust and torque coefficients are unknown, so

we do not know the exact input parameters for the virtual disk. However, the total thrust delivered by the propeller is known. In combination with a known rotation rate, this will give the thrust coefficient needed. Another option could be that the thrust- and torque coefficients are calibrated with the efflux velocity. However, since the efflux velocities were not measured during the field measurements of 2019, only the theoretical efflux velocity is known. It is uncertain if these theoretical free flow efflux velocities are in line with the actual efflux velocities from the tunnel thruster next to a quay wall.

3.3.1. Free flow

Since the initial comparison with the Wei experiments is not sufficiently convincing, the free flow of the virtual disk is studied and the results are shown in figure 3.5. The free flow means that the flow is not deflected by anything, so the vertical quay wall is located further away ($>10D_p$). Three different wall clearances, $10D_p$, $15D_p$ and $20D_p$, are modelled to study at which wall clearance the free flow situation is reached. These CFD results are compared to the free flow velocity field equations prescribed by PIANC [17], which are the equations of the Dutch (equations 2.3 and 2.4) and German (equations A.1-A.3) method.

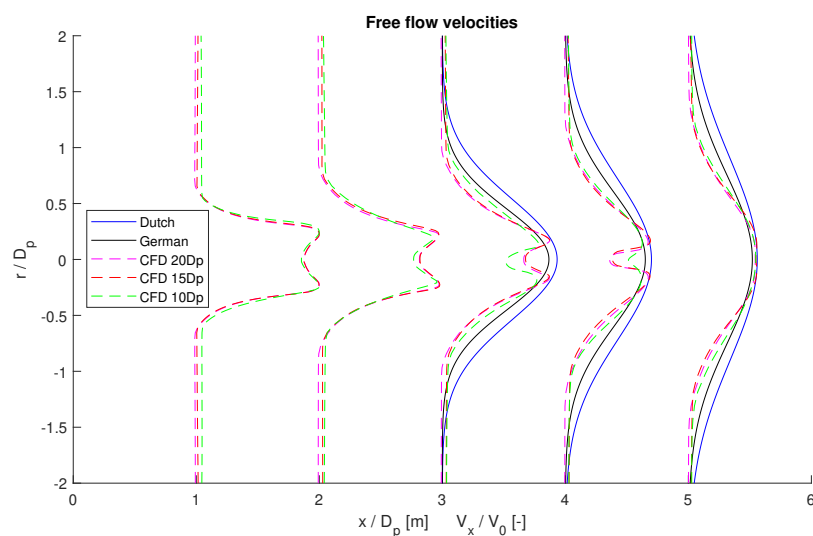


Figure 3.5: The free flow velocity comparison (with wall clearances of 10-20 D_p)

The non-dimensional radial coordinate r/D_p is shown on the y-axis and on the x-axis the non-dimensional longitudinal coordinate x/D_p is plotted with the non-dimensional axial velocity V_x/V_0 . For the German and Dutch method, the theoretical efflux velocity V_0 , from equation 2.10 is used. The CFD results in figure 3.5 are non-dimensionalized by dividing the velocities by the maximum velocity obtained in the domain (0.85 m/s) and the Dutch and German plots are non-dimensionalized by the theoretical efflux velocity (0.74 m/s). These maximum velocities of the CFD results came out somewhat higher than the theoretical efflux velocity, as discussed in section 3.3.

The plots for the Dutch and German method are not included for $x/D_p = 1$ and $x/D_p = 2$, because these equations are not valid for the velocity field in the zone of establishment. What can be seen from the CFD plots, is that the flow is fully developed after $x/D_p > 5$, because from here on the velocity drop in the core of the propeller axis has disappeared. The obtained velocity field from CFD is less radially distributed in comparison with the Dutch and German method, which is because the virtual disk is mainly adding momentum in the axial direction, which underestimates the spreading.

The total area beneath a data curve is representative for the amount of momentum which is added by the propeller. From figure 3.5 it seems that the virtual disk from the CFD analysis adds significantly less momentum into the flow than the German and Dutch methods prescribe. But this needs to be considered with nuance, this plot compares different non-dimensional velocities, so the actual magnitude of the momentum cannot be compared.

Since the velocity field of the $15D_p$ and $20D_p$ are almost identical and the $10D_p$ CFD result is somewhat distinct, it is concluded that the free flow condition is satisfied somewhere between $15D_p$ and $10D_p$. It is hard to draw a line where the exact turning point of free flow is located, because the transition takes place gradually.

Disregarding the facts that these CFD results take a longer distance to fully develop and that the CFD results are less radially distributed, the obtained free flow velocity fields are quite similar to the theory.

3.3.2. Solution for discrepancies

The conclusion from section 3.3 was that the virtual disk adds too much momentum to the flow in comparison with the experiment of Wei. The amount of thrust which is delivered by the virtual disk could be adjusted by changing the thrust coefficient K_t . The value of K_t which is used in figure 3.3 is chosen because it is the open water thrust coefficient at bollard pull conditions of the propeller used in the experiment of Wei. Since the experiment does not have open water conditions, this open water thrust coefficient could be misleading. The thrust coefficient of the virtual disk of the CFD model of the Vorstenbosch will be chosen on the basis of the total delivered thrust by the propeller, because this is a known value and the efflux velocity is not measured during the field tests of 2019.

The spreading of the virtual disk is expected to be less of a problem for the advanced model with a tunnel thruster. This is due to the fact that a long tunnel would give a more uniform distribution of the velocities at the outflow. Especially with a square shaped duct with a considerable length, it is expected that the swirl at the outlet is smaller in comparison with an open propeller.

Nevertheless, it is studied if it is possible to enlarge the swirl of the virtual disk and therefore enhance the spreading. This is examined by increasing the torque which is imposed by the virtual disk into the flow field. In figure 3.6 three plots are shown, the leftmost figure is the same as the $2D_p$ plot of figure 3.3. The rightmost figure is the same as the $2D_p$ situation of Wei (figure 3.4). The plot in the middle has a doubled K_q input value in comparison with the leftmost figure. The effect of this doubled K_q value is that there is more spreading in the flow and there is also some circulation in the core of the jet at the wall. This circulation is also visible at the experimental results of Wei. Pay attention to the fact that the color-bar range is different for each plot.

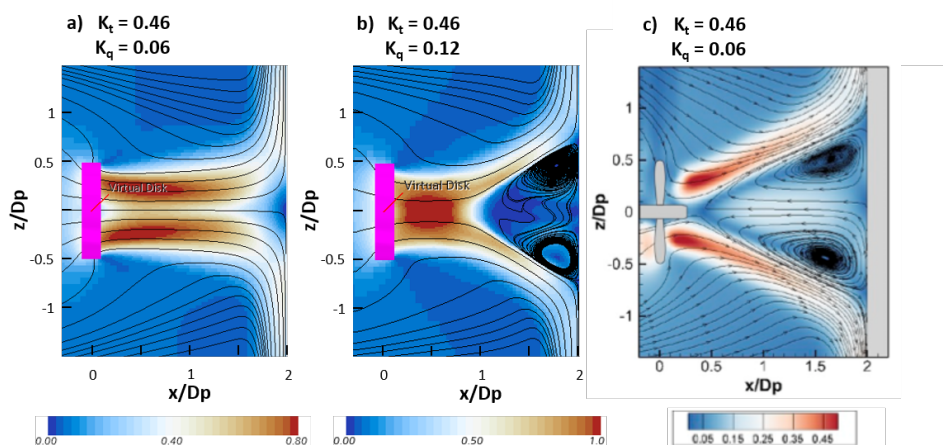


Figure 3.6: 2D velocity field for three different cases where the influence of K_q on the spreading of the jet is studied

The ratio between the surface averaged tangential and surface averaged axial velocity at the outflow of the virtual disk is 0.57 for the original situation ($K_t = 0.46$ & $K_q = 0.06$). This same ratio is with the doubled K_q value equal to 0.91, which means that the tangential velocities are more present for higher K_q values.

3.4. Convergence study

With CFD it is quite easy to obtain some results, but the question remains whether this result is an adequate solution. Convergence can be monitored in several ways. The first thing to check after the simulation has run, is the residual plot, which could help to judge the convergence. The residuals are a measure of the numerical error for each equation, they give a scaled average value over the entire domain of how good the conservation laws are met by the discretized solution. Generally, the residuals need to be as low as possible and as flat as possible. However, the residuals do not necessarily reflect the convergence of the quantity of interest. This study is interested in the maximum velocity and therefore this quantity needs to be monitored. It is necessary to do two convergence checks with implicit unsteady CFD calculations: check whether the quantity of interest has converged in time and check whether the mesh size is refined sufficiently. Missing convergence is caused by bad discretization in space or time.

The $2D_p$ model is used for this convergence study because this non-dimensional wall clearance is comparable to the situation of the Vorstenbosch. The dimensions of the Vorstenbosch will be much bigger, and with that, also the mesh size, but the same proportions of the thruster diameter can be used.

3.4.1. Convergence in time

For unsteady CFD solvers it is necessary to check whether the solution has reached steady state. This is done by monitoring the velocities over time, see figure 3.7. The orange line is the maximum measured 2D velocity in the whole domain. The maximum 2D velocity starts from zero and after 25 seconds it is steady around 0.8 m/s. The blue line is the monitored velocity in y direction at a certain point in the domain, see figure 3.2 for the location of the point. The y-velocities are plotted on the right vertical axis. The velocity in this point reaches convergence after 40 seconds, from then on the velocity is around 0.015 m/s. Since both curves have reached a certain plateau after 40 seconds, it is concluded that the steady state condition for the $2D_p$ case is reached after 40 seconds.

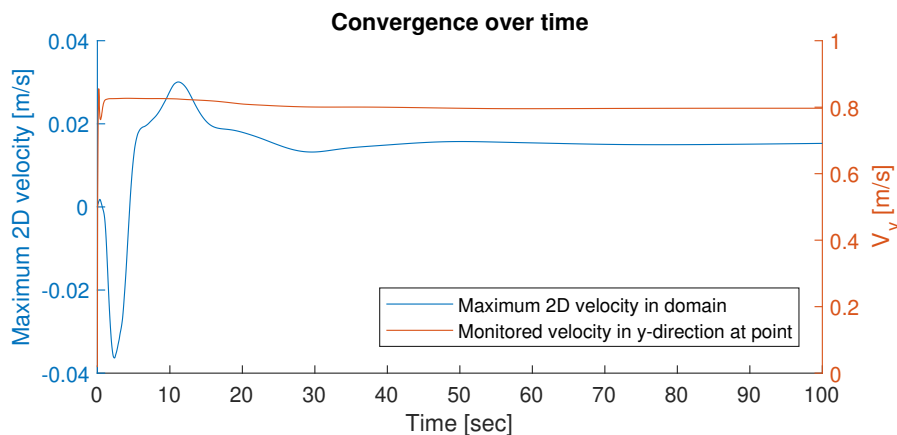


Figure 3.7: Velocity monitors that show the convergence over time

To make a rough estimation of the required solution time to reach convergence, the through flow time can be used. The through flow time can be estimated by estimating the distance the flow has to cover and what the mean velocity is of the flow. The distance $2D_p$ between the propeller and the wall is 15 cm, the distance along the wall is 30 cm and the flow back on the floor will proceed for approximately 30 cm. So, the total distance is 0.75 m and the mean velocity over the covered distance is less than 0.8 m/s, so the through flow is around 1 second. To achieve steady state, it is recommended to use at least 10 times the through flow time, which is amply achieved after 40 seconds.

3.4.2. Mesh convergence

This section shows that the results of the finite volume method converge to a certain solution which is independent of the mesh size. Several meshes are tested and the results are compared to each other to determine how many elements are required in the model to ensure that the result is not affected by changing the mesh size. The convergence criteria are met whenever an additional mesh refinement does not lead to a difference in the result, so additional mesh refinement is unnecessary.

The mesh sizes which are used for the convergence study vary between 130 thousand cells and almost 7 million cells. The solution time for all the different runs in this section is 40 seconds since this is the time necessary to reach the steady state solution. The base size for the smallest number of cells is equal to the radius of the propeller and the mesh size is systematically refined by varying the base size from 50% of D_p till 12.5% of D_p , with steps of 6.25%. Volumetric controls are used to refine the areas of interest, and it is chosen to use two of them which cover the whole width and height of the block. The first one covers 40 cm from the wall and the mesh size is here 50% of the base size. The second volumetric control covers 20 cm from the wall and the mesh size is here 25% of the set base size. The prism layer thickness is depending on the set base size, with the same percentage as the volumetric control of the base size. This means that the prism layer thickness varies with every mesh size. The smallest number of cells, 130.000 has a base size of 50% D_p and can be seen in figure 3.8. The highest number of cells tested has almost 7 million cells, the base size is here 12.5% of D_p and the cross section of the mesh can be seen in figure 3.9.

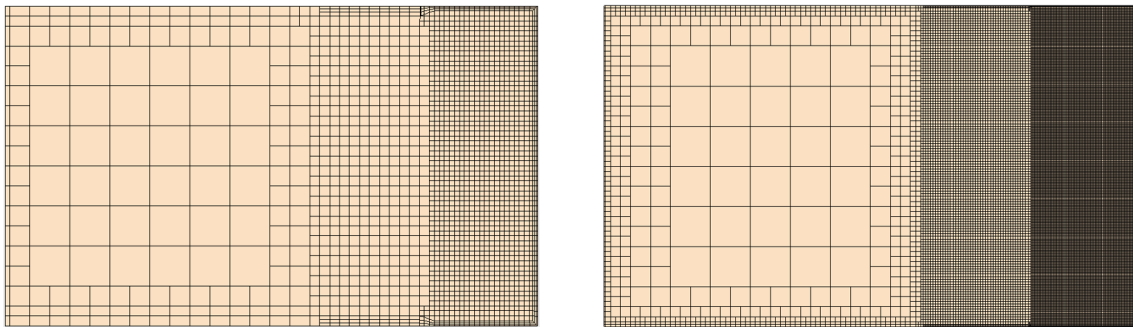


Figure 3.8: Mesh used for convergence study (130.705 cells) Figure 3.9: Mesh used for convergence study (6.787.659 cells)

The results of the convergence study can be seen in figure 3.10. The maximum 2D velocity in the domain is varying much more between the smaller number of cells, which means that these results are not reliable. But the differences between the results become much smaller with a larger number of cells. At the end a certain plateau is reached in the maximum 2D velocity in the domain, which is an indication that the solution is converged. The last additional mesh refinement does not affect the maximum 2D velocity, both 0.807 m/s. This means that the 2 million mesh can be considered as converged. With a base size of 18.75% of D_p and due to the volumetric control in the area of interest of 25% of the base size, the mesh size is 4.6875% of D_p in the area around the virtual disk. It is recommended to use the same mesh size of 4.6875% of D_p in the area of interest for the Vorstenbosch model.

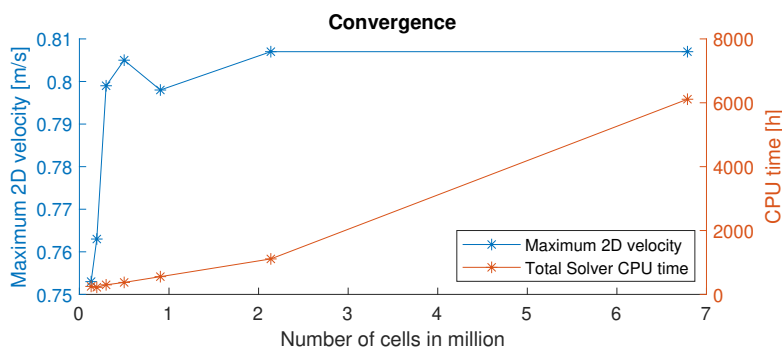


Figure 3.10: Mesh convergence

The process time of the finest mesh is more than 6000 CPU hours, which in this case came down to almost two weeks of running on the cluster of Deltares. The first half of the week, the simulation has run on 4 nodes of the cluster and the second half on 8 nodes of the cluster. This is also the reason that CPU time plot, the orange line in figure 3.10, is not fully linear at the end. It is expected that the CPU time plot would be linear for increasing mesh size, if all the simulations were run on the same number of nodes.

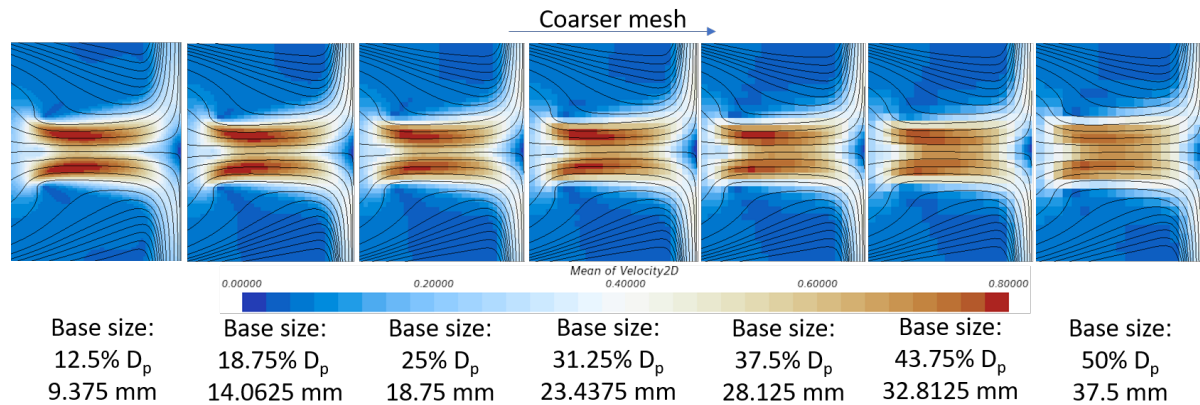


Figure 3.11: Obtained 2D velocity field for every mesh size

Figure 3.11 shows the different velocity plots at 40 seconds solution time for the different mesh sizes. During the simulation it was observed that there is much more spreading in the beginning of the simulation and that this spreading slowly disappears between 25-30 seconds of the solution time. It is expected that this has something to do with the re-circulation from the jet to the wall and the side walls/floor back into the virtual disk. Due to the different inlet conditions of the virtual disk, the jet loses its spreading.

Therefore, it is interesting to look at the influence of the location of the floor and side walls into the flow field. If the floor and walls are placed further away, the influence of re-circulation back into the virtual disk should be less for the same solution time of 40 seconds. And indeed, as figure 3.12 indicates, this is the case, the spreading is much more and therefore the close floor and side walls are causing the more axial flow for the used $k - \epsilon$ turbulence model.

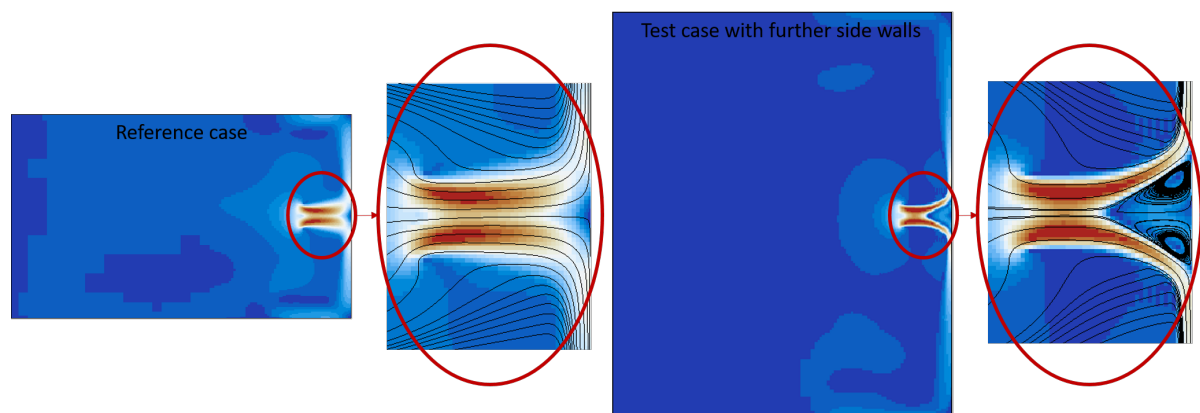


Figure 3.12: Reference 2D velocity field on the left and on the right the velocity field obtained with the side walls and floor further away. The spreading is significantly more present when the side walls and floor are placed further away from the jet.

3.5. Turbulence models

In this section some different turbulence models are discussed and compared to each other. Since the use of the $k - \varepsilon$ is most common in the literature found and it is recommended by STAR-CCM+ for marine applications, this turbulence model is used for all the simulations reported in the previous sections of this thesis.

The $2D_p$ case from the convergence study, described in section 3.1, is used to see the effect of the different turbulence models on the induced flow field. The mesh consists of some local refinements around the jet and wall area. The total number of cells in the mesh is almost 2 million. The only input parameter which has been changed in the $2D_p$ simulation, is the used turbulence model. The Realizable $k - \varepsilon$ two layer, the Shear Stress Transport $k - \omega$, the Reynolds Stress Turbulent model and the standard Spalart-Allmaras have been simulated for 40 seconds and the 2D velocity flow fields are shown in figure 3.13.

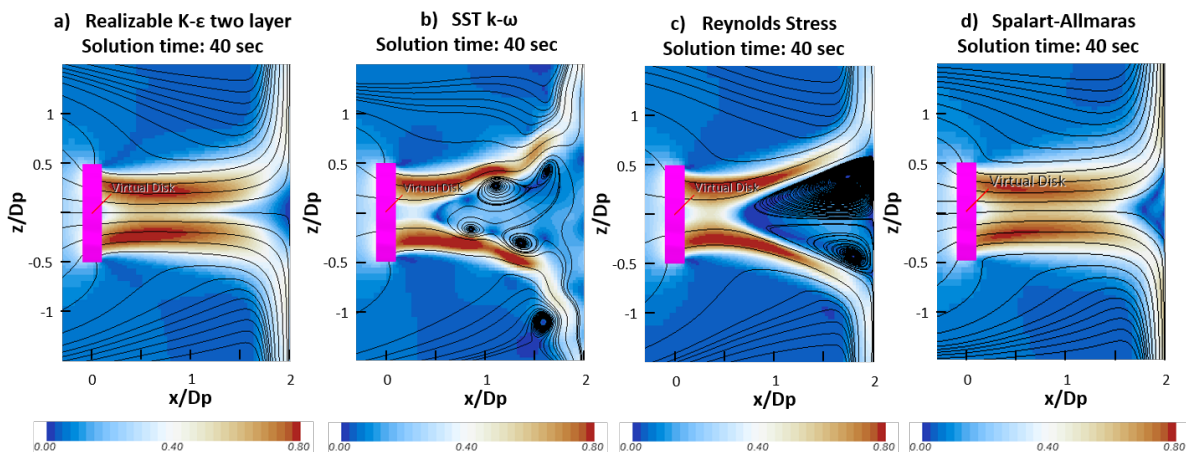


Figure 3.13: 2D velocity field of different turbulence models at solution time of 40 s

The plot of the Realizable $k - \varepsilon$ model has been seen and discussed before in figures 3.3 and 3.11. In the starting phase the spreading is present but collapses after 25-30 seconds. The spreading after 40 seconds is not similar to the $2D_p$ velocity field from Wei, see figure 3.4. As mentioned in section 3.3.2, the ratio between the tangential and axial velocities is 0.57.

The standard Spalart-Allmaras model shows roughly the same velocity field, but with slightly lower velocities. The spreading is also present for the first 25 seconds and collapses thereafter just like the Realizable $k - \varepsilon$ model. The ratio between tangential and axial velocities is 0.52 at the outflow of the virtual disk after exact 40 seconds.

The Reynolds Stress turbulence model adds a qualitatively accurate spreading to the jet, but this turbulence model is computationally expensive. The ratio between tangential and axial velocities is 0.60.

The velocity field of the $k - \omega$ turbulence model shows some spreading, but the streamlines consist of multiple smaller vortices. These vortices are changing over time and are locally deforming the jet. The jet is not stable over time and therefore it is chosen to average the flow over time for all the different turbulence models. The ratio between tangential and axial velocities at the outflow of the virtual disk is 0.55. In figure 3.14 the mean 2D velocity field within the time slot of 20-40 seconds is shown. The meandering in the jet of the $k - \omega$ turbulence model has disappeared because of the averaging.

In comparison with the $k - \varepsilon$ and Spalart-Allmaras turbulence model, the $k - \omega$ and Reynolds Stress turbulence model show a better spreading of the jet in the steady state condition. The mean velocity field of the SST $k - \omega$ model and the Reynolds Stress model show similarities to the $2D_p$ velocity field from Wei. The re-circulation of the jet from the side walls of the flume back into the virtual disk seems to cause some irregularities for the $k - \varepsilon$ and Spalart-Allmaras turbulence model. Due to the small

wall and keel clearances in the Vorstenbosch comparison, re-circulation is definitely expected. It is not beneficial to use the Reynolds Stress model because of its high computing costs. Therefore, it is chosen to use the $k - \omega$ turbulence model in the remainder of this study to make sure this re-circulation does not cause irregularities in the simulation.

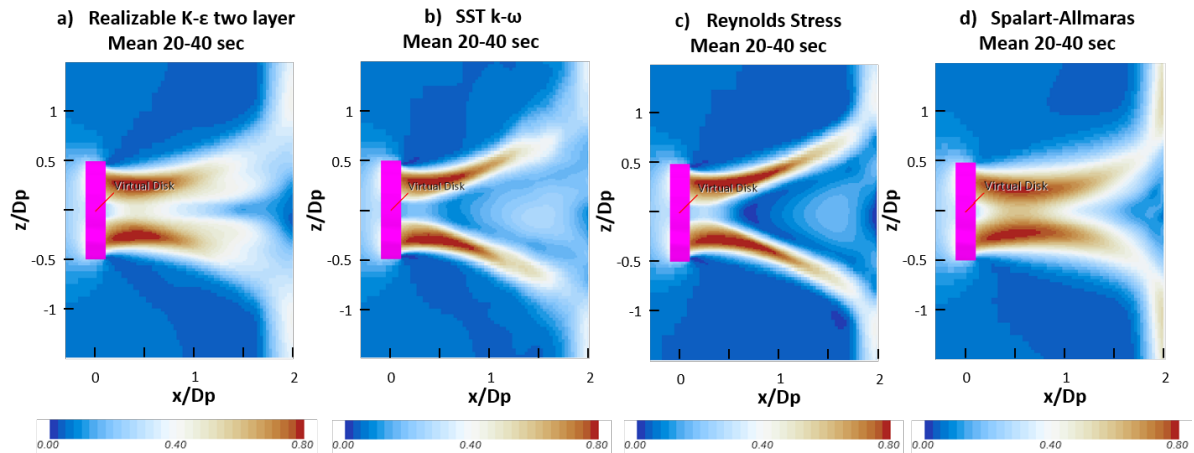


Figure 3.14: Mean 2D velocity field of different turbulence models (20-40 sec)

3.5.1. Convergence of k-omega turbulence model

The $k - \omega$ turbulence model shows an unsteady behavior and therefore it is good to check the convergence in time and space. Besides the convergence study of the $k - \epsilon$ turbulence model, discussed in section 3.4, another convergence study is done with the $k - \omega$ turbulence model. The same conditions are used for this $k - \omega$ turbulence mesh convergence study, as for the $k - \epsilon$ mesh convergence, discussed in section 3.4.2, except the applied turbulence model. The same solution time of 40 seconds is applied, the same meshes are run, except the prism layer is improved and therefore refined. The finest mesh of almost 7 million cells is skipped here due to the excessive computing time. The results of the maximum 2D velocities for different mesh sizes can be seen in figure 3.15.

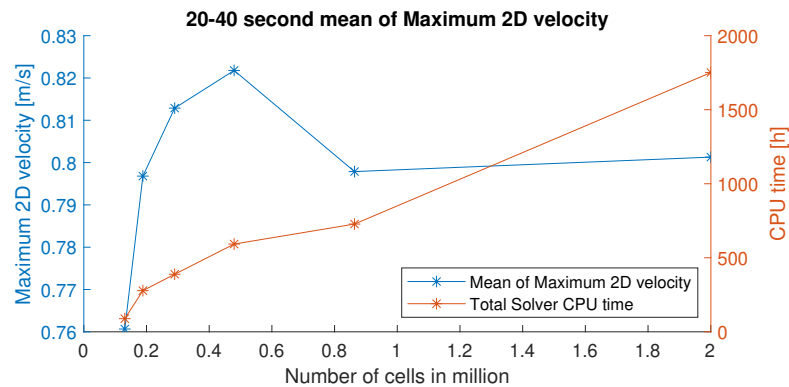


Figure 3.15: Mesh convergence of $k - \omega$ turbulence model

The difference in the obtained maximum velocity in figure 3.15 is from the second-last to the last less than 0.5%, and the solution can be considered as converged. The figure plots the averaged maximum obtained 2D velocity between 20-40 seconds. This averaging is necessary because the solution of the 2 million cells run is not fully stable over time, see figure 3.16. It is interesting that the fluctuation of the maximum obtained velocity only appears for very fine meshes. The turbulence and the unstable flow field of the jet can only be picked up by the exceptionally fine meshes within a CFD simulation. The total CPU time plot is not completely linear, because the runs were done on a different number of cores/nodes.

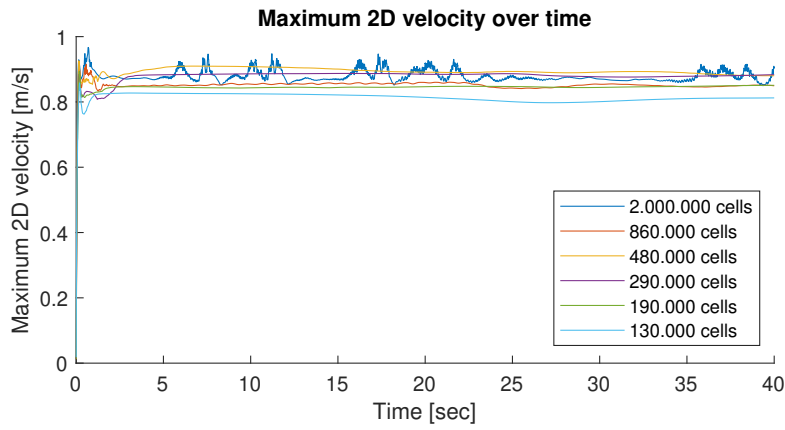


Figure 3.16: Maximum 2D velocity over time for the finest two meshes

The solution is not stable anymore because the mesh is from 2 million cells on, fine enough to include the small vortices in the velocity field, which can be seen from figure 3.17. These small vortices within the jet can deform the jet locally and change over time. These unstable small vortices explain the fluctuations in the maximum 2D velocity plot of figure 3.16. These fluctuations do not disappear after time, so the mean of the velocity fields over the last 20 seconds of solution time can be considered as the "steady" state condition.

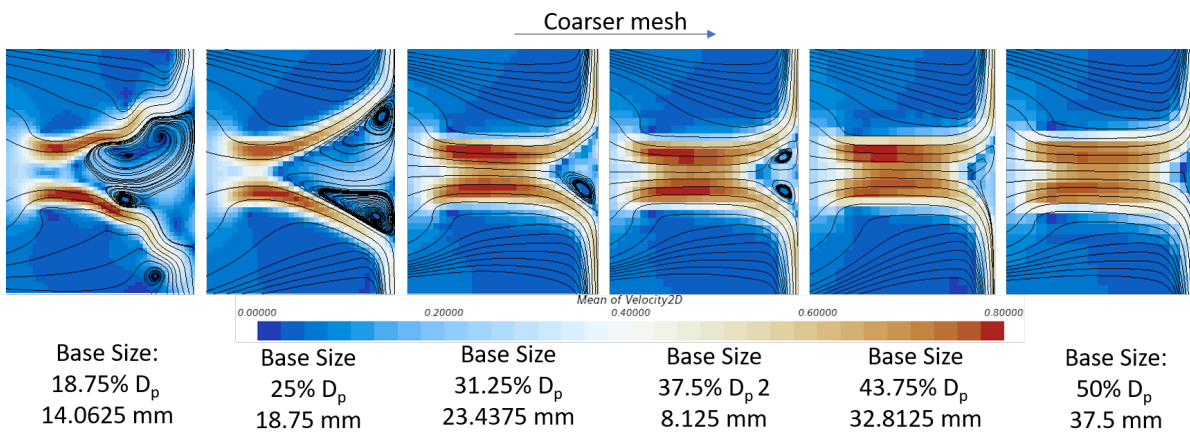
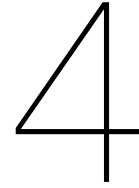


Figure 3.17: Obtained 2D velocity field for every mesh size of $k - \omega$ turbulence model



Vorstenbosch model

In this chapter the CFD models are discussed, which are built to compare the CFD results with the field measurements of the MTS Vorstenbosch done in 2019. These same CFD models are also used to compare with the theory provided by PIANC [17]. With some additional CFD models a parameter sensitivity analysis can be performed.

4.1. Built models

In this thesis different models are built to compare the model with field measurements or the theory under different conditions. There are many conditions/input parameters that can be adjusted, but all the models are based on the same basis model, which will be discussed in section 4.2. In this section the adjusted input parameters are discussed to compare more than one specific situation.

4.1.1. Comparison Cantoni

The goal of this thesis is to simulate the situation during the field measurements of 2019 in a numerical model. During the field measurements 23 different tests were performed to measure the reflected flow from the bowthruster against a quay wall. During these tests, the ship position, the water depth, the used bowthruster and the applied power were varied. For an extensive description of the test cases and their results, a reference is made to Cantoni [7]. This study attempts to simulate four of these test cases in a CFD model and compare the CFD results with the results of Cantoni. The four test cases which are compared to each other are listed in table 4.1 with their specific characteristics.

	Bowthruster activated	Wall clearance	Keel clearance
Test 1	BT1	330 cm	103 cm
Test 2	BT2	600 cm	103 cm
Test 11	BT1	330 cm	257 cm
Test 13	BT1 & BT2	330 cm & 600 cm	288 cm

Table 4.1: Test cases

4.1.2. Comparison PIANC guidelines

Subsequently, these same four CFD simulations as in table 4.1 are compared to the PIANC theory. This comparison is made to check whether these CFD results comply with the current guidelines. It is important to have simulations with different wall clearances and keel clearances, because the similarities/differences between different conditions can be checked.

4.1.3. Parameter sensitivity tests

Some additional CFD simulations are done to check the influence of three different parameters on the maximum bottom velocity present in the domain. These simulations extend the range of parameters beyond those investigated during the field measurements of 2019. Two of the tests in table 4.1 are reused for the parameter sensitivity analysis, test 1 and test 11, and four new models are simulated.

The specified parameter which is analyzed and the quantity that belongs to these parameters can be seen in table 4.2.

Parameter	Specification	Existing / new run
Keel clearance	1.03 m	Test 1
	2.57 m	Test 11
	4.11 m	New
Wall clearance	3.30 m	Test 11
	4.50 m	New
	5.70 m	New
Rotation rate	100 % rpm	Test 11
	50 % rpm	New

Table 4.2: Parameters that are varied to check their influence on the maximum bottom velocity

4.2. Model setup

In this section the input parameters of the base CFD model are discussed, the mentioned models discussed before are all based on the model discussed in this section. First the imported ship geometry is discussed in section 4.2.1, which is followed by the geometry of the tunnel of the bowthruster in section 4.2.2. The applied boundary conditions are shown in section 4.2.3 and the mesh is shown in section 4.2.4.

4.2.1. Ship geometry

The MTS Vorstenbosch is a big inland tanker built in 2011 and the main dimensions are listed in table 4.3. Since there was no 3D CAD (Computer-Aided Design) model available of the MTS Vorstenbosch, another 3D CAD model of an inland tanker is used, which is re-scaled to the dimensions of the Vorstenbosch. This 3D CAD model is downloaded from the 3D warehouse of Sketchup [11], which is a 3D modeling computer program. The model is shown in figure 4.1. The downloaded *.dae* file has been converted to a *.stl* format, which is readable by STAR-CCM+.

Dimension	Value
Length over all (L_{OA})	147.5 m
Beam (B)	22.8 m
Maximum draught (T)	5.4 m

Table 4.3: Main dimensions of MTS Vorstenbosch

Dimension	Value
Length over all (L_{OA})	113 m
Beam (B)	14.4 m
Maximum draught (T)	3.4 m

Table 4.4: Main dimensions of the original 3D model [11]

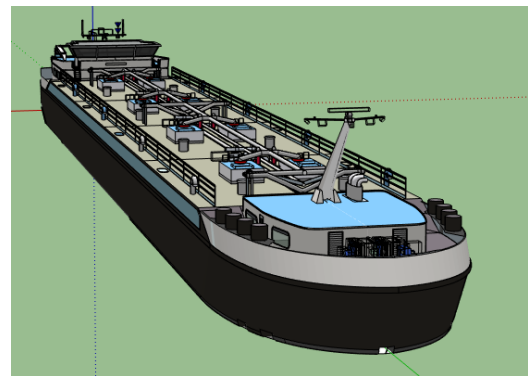


Figure 4.1: Tanker 3D CAD (from 3D Warehouse [11])

The reference system which is used has the x-axis in the longitudinal direction, positive in bow direction. The positive y direction is towards portside and the positive z direction is upward. The 3D model needed to be scaled non uniformly to obtain the same dimensions of the Vorstenbosch, see table 4.3 and 4.4. The scale factors in x, y and z-direction were respectively 1.31, 1.58 and 1.59.

Another adjustment which is needed, is the removal of the tunnel system for the bowthruster in the CAD model to make space for the tunnel geometry of the MTS Vorstenbosch. This removal is done by making a new 3D CAD which exactly fits in the bow of the ship, and combining both 3D model parts, see figure 4.2.

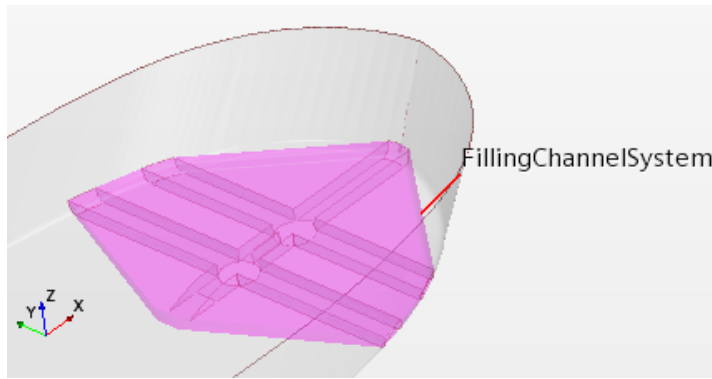


Figure 4.2: Filling of old bow thruster channel system in 3D CAD

4.2.2. Tunnel thruster

Two Veth 4-channel bowthrusters are installed in the MTS Vortenvosch, both of the type Veth Jet4-K-1400. The main characteristics of the bowthrusters can be seen in table 4.5.

Characteristic	Value
Maximum power	618 kW
Nominal revolutions	1800 rpm
Reduction	4.909:1
Propeller diameter	1420 mm
Thrust	60 kN

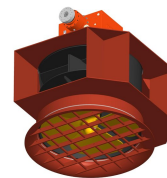


Table 4.5: Bowthruster characteristics (from Veth and Cantoni[7])

Figure 4.3: Veth jet (from Veth [35])

The dimensions and location of both thrusters are adopted from the general dimensions document received from Veth and the MSc Thesis of Cantoni [7]. Since the shape of the hull of the 3D CAD is not the same as the hull of the Vorstenbosch, the x locations of the tunnels do not correspond with the corresponding wall clearances, see figure 4.4. Therefore, it is chosen to adjust the hull shape by re-scaling in x-direction in such a way that the x locations of the tunnels match the wall clearances of the Vorstenbosch, see figure 4.5. A scale factor of 1.33 is used in x-direction only, which means that the total length of the CAD model does not match the total length of the Vorstenbosch anymore, but since only the forward part of the ship is modelled in the domain, this does not cause any problems. The distance between the quay wall and the ship was constant during the field measurements and therefore the same quay wall clearance of 0.5 m is adopted.

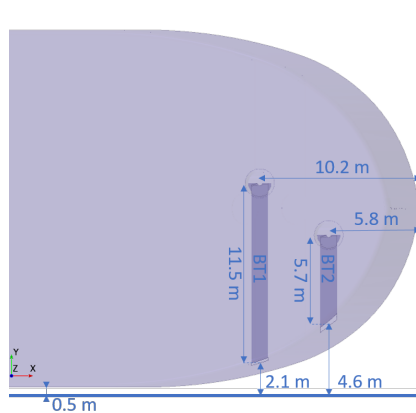


Figure 4.4: Top view of old hull, with wrong wall clearances

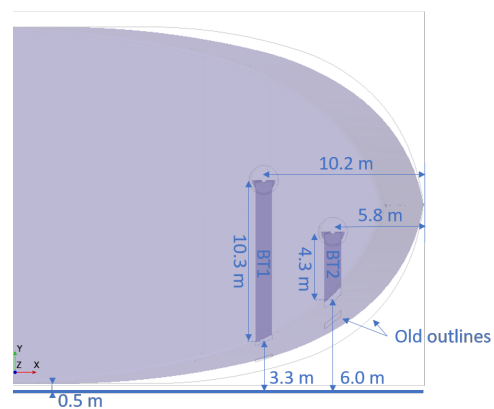


Figure 4.5: Top view of new hull, with correct wall clearances

The bowthruster positioned more towards the stern is bowthruster 1 (BT1) and the one more towards the bow is bowthruster 2 (BT2). Only one of the four channels for each thruster is included in the 3D model, because the other three were not of influence during the tests. There are also some details of the shaft and flow deflectors above the propeller included in the model, see figure 4.3 and 4.6. The exact dimensions of the round shapes of the flow deflectors are not known, so these are drawn by the author's own discretion. The shaft diameter is equal to the inner radius of the virtual disk: 280 mm.

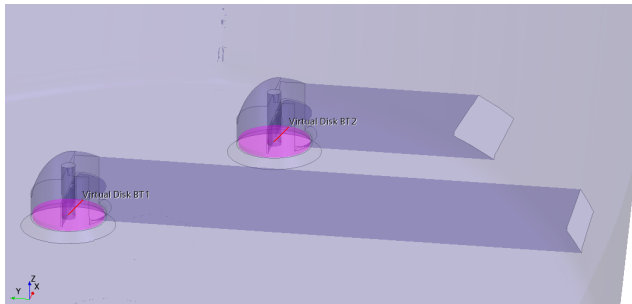


Figure 4.6: 3D view of both channels in CAD model

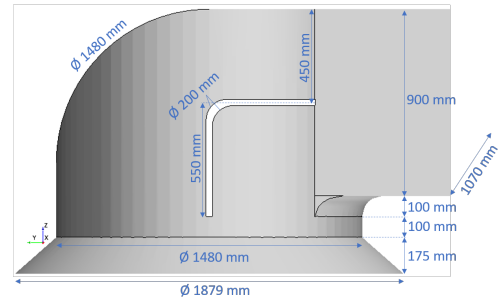


Figure 4.7: Tunnel dimensions

The pink parts in figure 4.6 are the virtual disks, which represent the propellers which sucks up the water from beneath the keel. The virtual disks have a diameter of 1420 mm and rotate with $1800/4.909 = 366.67$ revolutions per minute. It is chosen to calibrate the thrust coefficient on the total thrust which the actual propeller delivers, instead of more obvious calibration method with the efflux velocity. This decision is made, because the efflux velocity of the MTS Vorstenbosch is not measured during the tests, so only the theoretical efflux velocity is known from equation ???. However, it is unclear if this equation is representative for the efflux velocity out of a long tunnel since the parameters in the equations are only dependent on the power and diameter of the propeller and not on the dimensions of the tunnel. The thrust coefficient K_t is determined based on the relation in equation 2.55 with the total thrust of 60 kN. The used input parameters are equal for both virtual disks and can be seen in table 4.6.

Input parameter	Value
Inner Radius	140 mm
Outer Radius	710 mm
Thickness	300 mm
Inflow Plane Radius	781 mm
Inflow Plane Offset	71 mm
Propeller Handedness	Right-handed
Rotation Rate	366.67 rpm
Thrust coefficient	0.385
Torque coefficient	0.035

Table 4.6: Input parameters virtual disk

4.2.3. Boundary conditions

To keep the number of cells in the mesh moderate, the domain is limited to about 20 meters in front and behind (in x direction) of the tunnel outflow, see figure 4.8. Every boundary is a no-slip wall, except the free surface which is a slip wall, and the orange boundaries are pressure outlets with a hydrostatic pressure profile, which makes sure that there is no pressure gradient over the boundary and therefore the velocities are ideally zero at these locations.

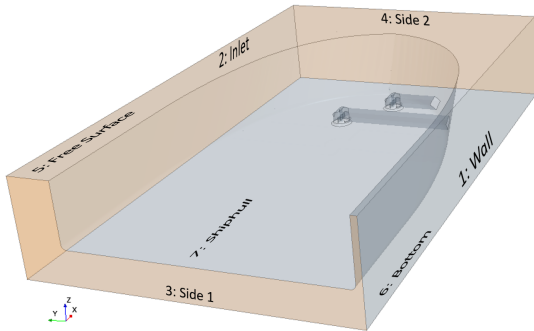


Figure 4.8: The domain of the CFD model (Test 13)

Boundary	Type	Specification
1: Wall	Wall	No-slip
2: Inlet	Pressure Outlet	101325.0 Pa
3: Side 1	Pressure Outlet	101325.0 Pa
4: Side 2	Pressure Outlet	101325.0 Pa
5: Free Surface	Wall	Slip
6: Bottom	Wall	No-slip
7: Ship hull	Wall	No-slip

Table 4.7: Boundary condition specification

4.2.4. Mesh

The mesh consists of a surface remesher, trimmed cell mesher and a prism layer mesher. Some of the default controls are adjusted and they are listed in table 4.8. The mesh includes five surface controls and four volumetric controls around the area of interest to refine the mesh locally. The surface controls are shown in table 4.9 and the control volumes are visualized in figure 4.9 and the input parameters can be found in table 4.10.

Base size	0.5 m
Minimum surface size	0.005 m
Nr of prism layers	2
Prism layer stretching	1.5
Prism layer thickness	33.33% of BS

Table 4.8: Default controls for meshing

Surface	Thruster Inlet	Tunnel	Wall	Bottom	Ship
Target surface size	0.02 m	0.0625 m	0.0625 m	0.0625 m	0.0625 m
Minimal surface size	0.01 m	0.03125 m	0.03125 m	0.03125 m	0.03125 m
Nr of prism layers	4	4	12	12	3
Prism layer total thickness	0.025 m	0.025 m	0.05 m	0.05 m	0.025
Prism layer stretching	1.5	1.5	1.1	1.1	1.5

Table 4.9: Surface controls

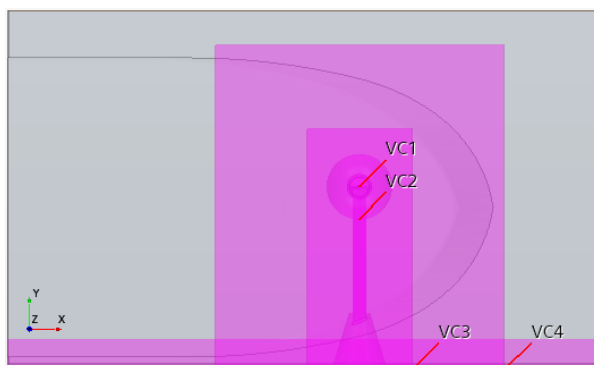


Figure 4.9: Control volumes in which the mesh is refined

	Absolute size	% of base
VC 1	0.03125 m	6.25 %
VC 2	0.0625 m	12.5 %
VC 3	0.125 m	25 %
VC 4	0.25 m	50 %

Table 4.10: Volumetric control input parameters

With all these settings, the mesh of figure 4.10 is obtained for Test 11. For the other tests, the mesh is comparable, but for Test 1 and Test 2, the amount of cells is smaller due to the smaller keel clearance.

Test 13 has more cells because two bow thrusters need to be refined with volumetric controls. The total number of cells for the tests can be found in table 4.11.

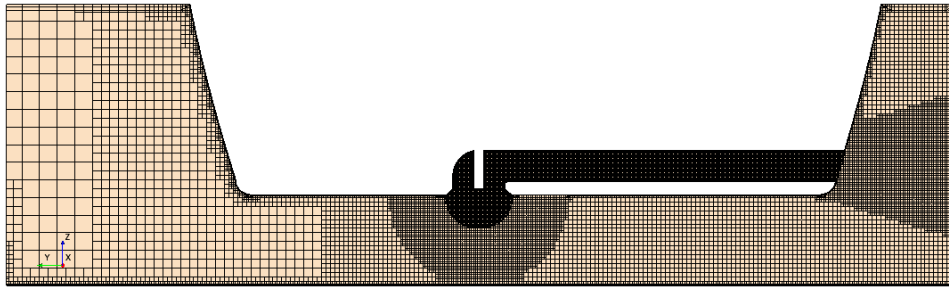


Figure 4.10: Mesh in cross section through tunnel thruster (Test 11)

	Test 1	Test 2	Test 11	Test 13
Nr. of cells	7,978,007	7,959,402	8,448,497	10,170,975

Table 4.11: Number of cells in mesh of each test

These same 4 tests are used to compare to the guidelines presented in PIANC [17] and to the field measurements. These four tests are referred to as the first series of runs. The second series of runs are regarding the parameter sensitivity test. For the parameter sensitivity test the same model is used as basis and the domain is expanded to compute different wall and keel clearances. The power is changed by adjusting the rotation rate of the virtual disk.

5

Results

In this chapter the bottom velocities induced by the bowthruster of the Vorstenbosch are analyzed.

The instantaneous velocity field of test 11, see table 4.1 for details, at a solution time of 81 seconds is shown in figure 5.1. The velocity field of the other three tests that are meant to be compared to the field measurements of the Vorstenbosch can be found in appendix B.

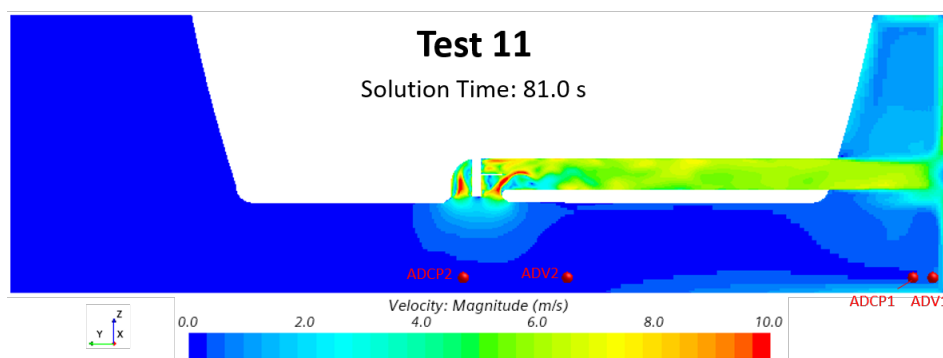


Figure 5.1: Instantaneous velocity field Test 11

The water is sucked in at the inlet from beneath the ship and subsequently deflected into the tunnel. The outflow of the tunnel is quite uniform, the tangential velocities are reduced because of the long square shaped tunnel. This causes that jet out of the tunnel to remain initially square shaped, but the jet accelerates the surrounding fluid as well. The jet is deflected radially outwards when it hits the quay wall. The jet that follows the walls and later also the bottom is quite thin and it seems that the sensor locations are not placed at a height that catches the maximum bottom velocity.

Since this is an unstable solution over time, it is necessary to check the convergence over time, which is done in section 5.1. The velocities at the locations of the sensors during the test are discussed in section 5.2. The maximum near-bed velocities are compared to the given theory in the PIANC report in section 5.3. The independence of the location of the boundaries is checked in section 5.4. In section 5.5 the wall jet thickness is discussed and related to the theory of Rajaratnam. The turbulence intensity of the flow field is shown in section 5.6. The chapter ends with the results of the parameter sensitivity tests in section 5.7.

5.1. Convergence over time

Since this study focuses on the velocities at the location of the placed sensors during the field measurements in 2019 and the maximum bottom velocities, the velocities are monitored over time. The horizontal velocities at the sensor locations are plotted over time for test 13 in figure 5.2. The horizontal

velocity is equal to $V_{hor} = \sqrt{V_x^2 + V_y^2}$ and excludes the velocity in z-direction. Test 13 has run on 8 nodes and hence the solution time is further in comparison with the other tests, which ran on only 4 nodes. The other test case results can be found in appendix C.

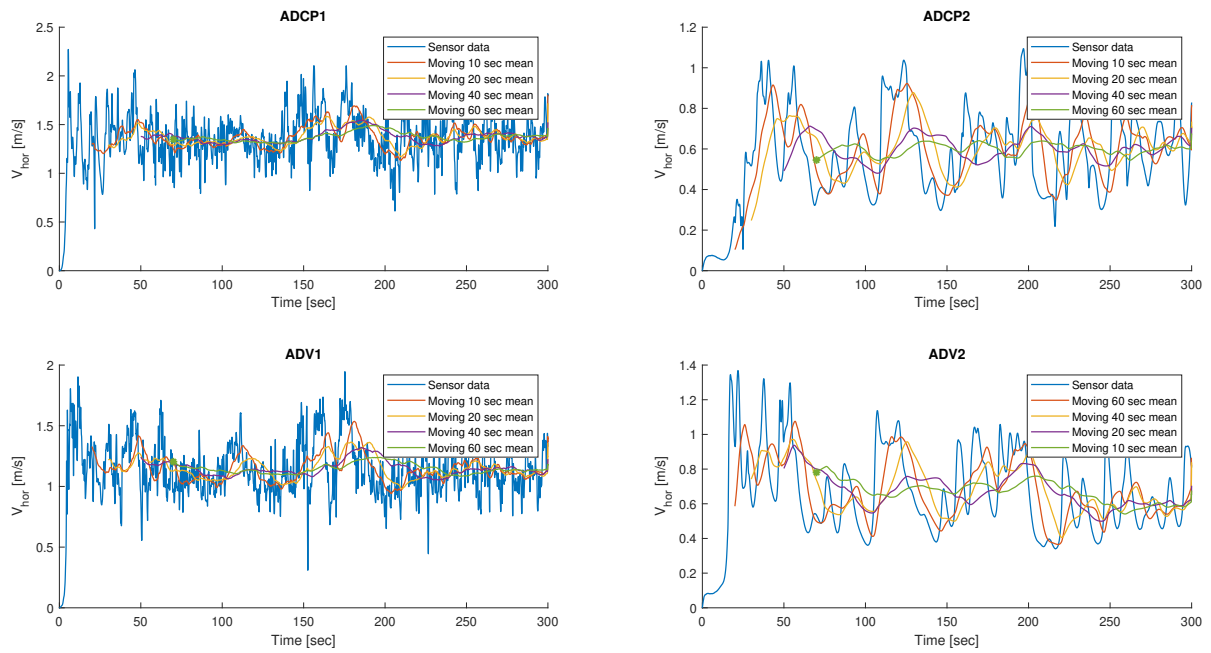


Figure 5.2: CFD results for the horizontal velocity at sensor location over time for test 13

Figure 5.2 shows that the velocities obtained at the sensor locations fluctuate over time, which is as expected. The ADCP1 & ADV1 are located more towards the corner of bottom and quay wall and here the velocities do vary at a high frequency. The sensor location further away from the quay wall, and more towards the inlet of the bowthruster, ADCP2 & ADV2, do also vary, but with a lower intensity.

To compare these results with the results of the field measurement, it is necessary to average the velocities over a certain time frame. In the MSc thesis of Cantoni [7] the data is averaged over the total time frame of each test, which lasted 2 minutes. There is not a certain starting period considered in the post-processing of the data. The CFD analysis should include a certain starting phase, especially the sensors further away from the wall experience the jet after some startup time. Since the field experiments are build up with 2 min test with subsequently 25%, 50%, 75% and 100% of the power, so the 100% power test does not start with a zero-velocity field. The CFD analysis does start with a zero-velocity field, because the engine goes from 0% power to 100% power at $t = 0$ seconds, so there needs to be a certain startup time which is excluded in the data processing. The sensors ADCP1 & ADV1, located more towards the wall, have a startup-time of less than 10 seconds. The sensors further away from the wall, ADCP2 & ADV2, have larger startup-times, because the jet from the wall takes more time to reach these locations.

Due to the computing time of the numerical model, a solution time of 120 seconds for every test run is not feasible. This would mean that all the simulations need to run for more than 2 months. Therefore, it is chosen to average over a shorter time period, taking into account that this includes a certain averaging error margin.

What can be seen from figure 5.2 is that the sensors more towards the corner (ADCP1 & ADV1), show a high frequency fluctuation and also some lower frequency fluctuation. It is necessary to catch both fluctuations in the mean velocity over time. A Fast Fourier Transform (FFT) analysis is applied to give more insights in which frequencies are most present, but the FFT analysis did not gave a good representation. Therefore, the moving averages of 10, 20, 40 and 60 seconds are plotted in figure 5.2. The 10 seconds mean plot contains many fluctuations over time, so a 10 second mean will not

give a good representative value for the velocity over time. With the moving 60 second mean these fluctuations seem to be flattened out over time and even the low frequency fluctuations are flattened out to a certain extent. For ADCP1 the 60 seconds mean fluctuates between 1.308 and 1.462 seconds and for ADV1 the 60 seconds mean fluctuates between 1.095 and 1.216. This means an averaging error margin for ADCP1 and ADV1 of 5.6% and 5.2% respectively for this data set. The 60 seconds mean of the horizontal velocity for ADCP2 and ADV2 fluctuate between 0.543-0.641 and 0.637-0.815 respectively. The averaging error margins are 8.3% and 12.3% respectively.

The error margins are much higher for the sensor locations further away from the wall, which is in line with the expectation, looking at the data sets. Therefore, the sensors ADCP1 & ADV1 are considered as more valid than the other two data sets. The error margin will become less, when the averaging time will increase, but since a limited computing time is also desirable in this study, the 60 second mean error margin is considered as acceptable.

The data sets of the other test are also unstable, see appendix C. The data sets are plotted with a mean value of the horizontal velocity between 10 - 70 seconds, so 60 seconds mean with the exclusion of the startup time of 10 seconds. For test 1, 2 and 11, a peak velocity at the moment of impact of the jet at the bottom in the corner is visible for ADCP1 & ADV1. After the starting phase, the data starts to fluctuate around a certain value with a high frequency. The lower frequency fluctuations for tests 1,2 and 11 seem to be less in comparison with test 13. This is due to the fact that test 13 has two bowthrusters activated, which causes that the jets have to interact and this causes extra fluctuations. The data sets are compared to the field measurements in section 5.2.

Since the direction of the jet fluctuates at a low frequency, the velocities at a fixed location fluctuate in a lower frequency. Therefore, it is interesting to look at the maximum obtained velocity in a certain control volume at the bottom. This control volume covers 8 meters in normal direction from the wall and has a height of 0.2 m. The length of this control volume covers the full length of the domain. The monitored maximum velocity in y-direction in this control volume represents the maximum bottom velocity and can be seen over time in figure 5.3 for the different test cases.

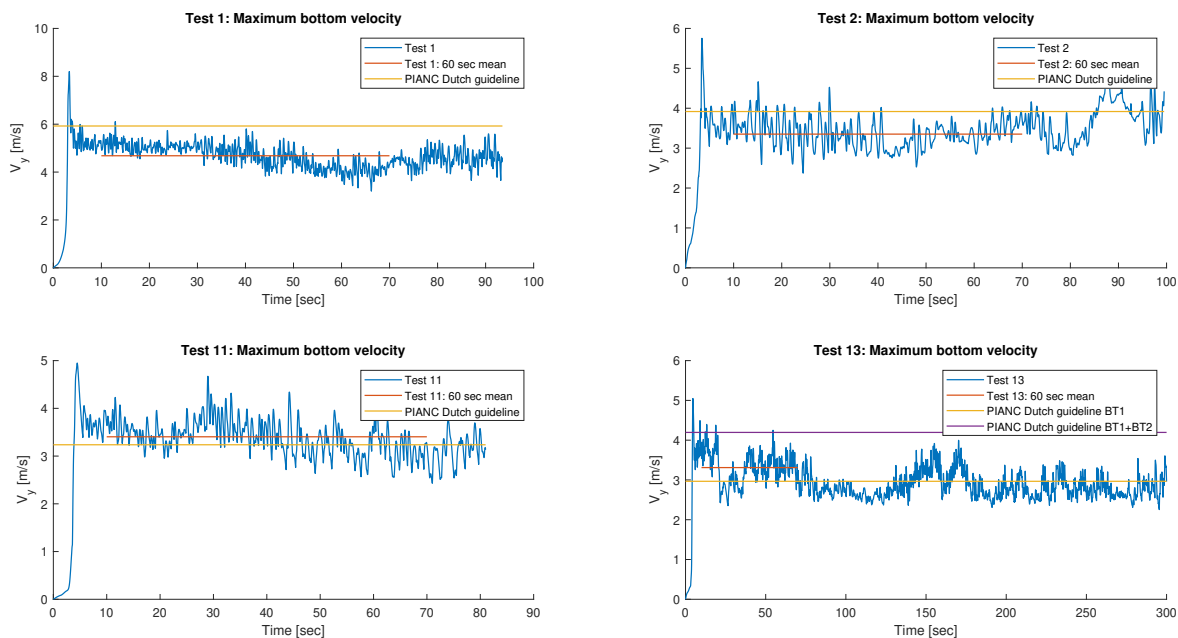


Figure 5.3: CFD result for the maximum bottom velocity in y-direction for each test

Test 13 has run for a much longer period than the other tests and it seems that the 60 second mean between 10-70 seconds is not representative for the whole dataset, because the mean between 200-300 seconds is lower. But to be consistent for every test, the mean value between 10-70 seconds is used in the rest of this thesis.

5.2. Comparison with field measurements

The velocities measured with sensors during the field measurements will be compared to the measured velocities at the sensor locations for the CFD simulations in this section. Since the sensor locations at the wall show smaller averaging errors, these locations are considered as more valid. Therefore, the focus will be on the near wall sensor locations: ADCP1 & ADV1.

Since these locations are positioned at a velocity gradient $\partial u/\partial z$, the exact location is important for the measured velocity, see figure 5.1. A few centimeters above or below and the velocity could be doubled or halved. Therefore, it is insightful to plot the velocity profiles over the whole height for the sensor locations, see figure 5.4. The velocity profiles of the other tests can be found in appendix D.

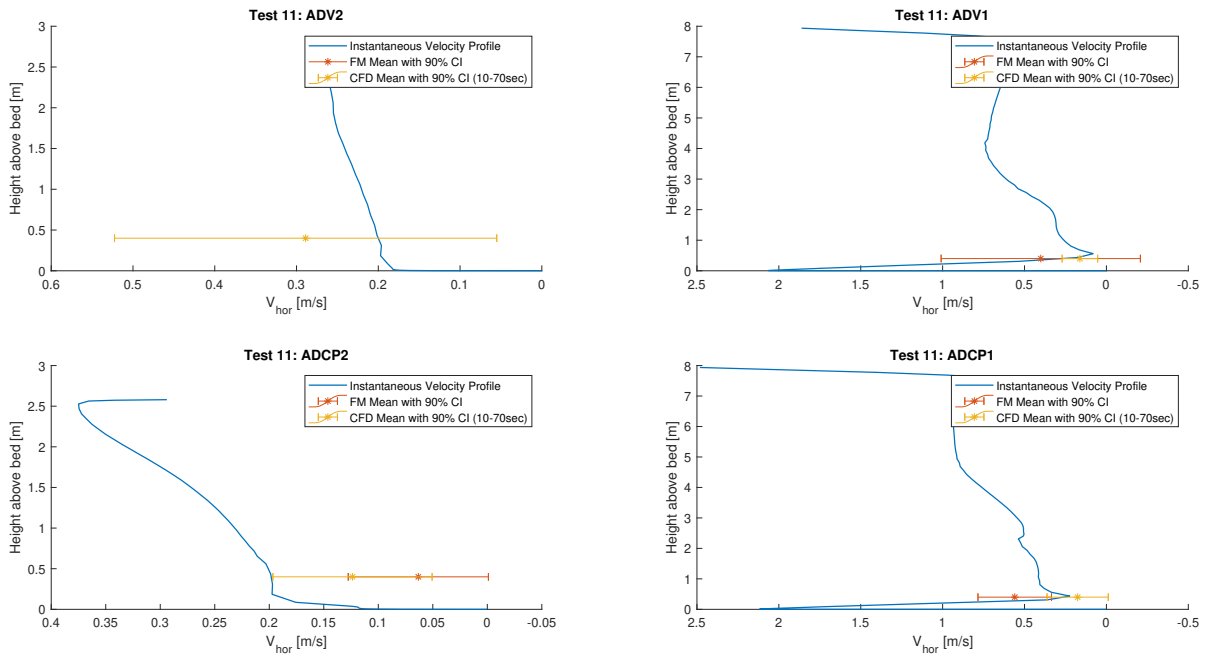


Figure 5.4: Velocity profile through sensor locations Test 11 at 81s. The mean value of the CFD results and the field measurements (FM) are plotted with their 90% confidence interval (CI).

The mean value of the CFD results and the mean value from the field measurements (FM) are plotted with a 90% confidence interval (CI). The 90% confidence interval is obtained by multiplying the standard deviation by the value 1.645. The CFD standard deviation is based on the data in the time interval 10-70 seconds.

The field measurement data of sensor ADV2 is unfortunately missing for tests 11 and 13. The sensors located near the wall, ADCP1 & ADV1, seem to miss the peak velocity at the bottom looking at the velocity profile obtained from the CFD results. This could be an explanation for the relatively low velocities obtained during the field measurements.

The confidence intervals of both the field measurements and the CFD results are overlapping for most of the test cases. However, it is good to note here that there is quite some uncertainty in these mean values and the mean values of the CFD and field measurements can differ a lot from each other, see table 5.1. The uncertainty is present for four reasons. First the averaging of the data over 60 seconds includes an error and secondly the velocity is sensitive to the height at which it is measured. If the sensor location were actually positioned 10 cm lower, the obtained CFD velocity could be more than doubled, due to the high velocity gradient. The third reason for uncertainty is that the bottom is simulated as a smooth wall, while the bottom is actually rough during the field measurements. The exact depth is also varying locally due to the loose rocks on the bottom. The last reason for the uncertainty is the unknown efflux velocity during the field measurements.

The comparison in table 5.1 is visualized in figure 5.5. The velocities at the sensor locations in the CFD analysis are most of the time higher than measured during the field tests, except for the ADCP1 and ADV1 sensor of test 1 and 11. Test 2 has on the other hand much higher velocities for ADCP1 and ADV1 during in the CFD analysis compared to the field measurements. But as mentioned, the table and plot alone with the mean values could be misleading, due to the sensitivity on the height. The velocity profiles in figure 5.4 and appendix D give more insight with a high velocity gradient at the bottom for ADCP1 and ADV1.

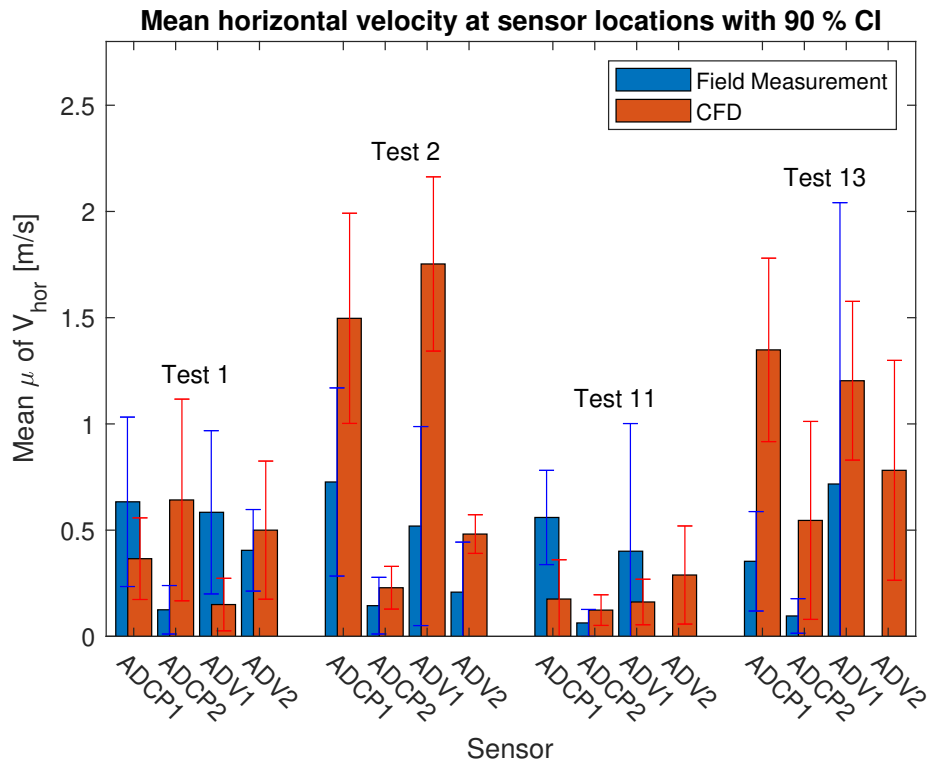


Figure 5.5: Plot with the mean velocity of each sensor with a 90% Confidence Interval

Test nr	Sensor	CFD Results		Field Measurements		Difference $\Delta \mu$ [m/s]
		μ [m/s]	σ [m/s]	μ [m/s]	σ [m/s]	
Test 1	ADCP1	0.37	0.12	0.63	0.25	-0.27
	ADCP2	0.64	0.29	0.13	0.07	0.52
	ADV1	0.15	0.08	0.58	0.24	-0.43
	ADV2	0.50	0.20	0.41	0.12	0.10
Test 2	ADCP1	1.50	0.30	0.73	0.27	0.77
	ADCP2	0.23	0.06	0.14	0.08	0.08
	ADV1	1.75	0.25	0.52	0.29	1.23
	ADV2	0.48	0.06	0.21	0.14	0.27
Test 11	ADCP1	0.18	0.11	0.56	0.14	-0.38
	ADCP2	0.12	0.04	0.06	0.04	0.06
	ADV1	0.16	0.07	0.40	0.37	-0.24
	ADV2	0.29	0.14	-	-	-
Test 13	ADCP1	1.35	0.27	0.35	0.14	1.00
	ADCP2	0.55	0.29	0.10	0.05	0.45
	ADV1	1.20	0.23	0.72	0.81	0.49
	ADV2	0.78	0.32	-	-	-

Table 5.1: Mean (μ) and standard deviation (σ) of measured V_{hor} between 10-70 seconds

5.3. Comparison with PIANC theory

In this section the efflux velocity out of the tunnel will be discussed and compared in subsection 5.3.1 to the theoretical efflux velocity from PIANC [17]. Thereafter in subsection 5.3.2, the focus will be on the comparison of the maximum bottom velocities from the PIANC and the CFD results.

5.3.1. Efflux velocity

The efflux velocity is defined as the maximum velocity at the exit of the propeller and is already extensively described in section 2.2.3. The formulae in this section are based on ducted propellers, but this is different from a square shaped tunnel with a length of 10.3 meter, which is used in this study. Therefore, it is interesting to look at the differences between the theory and the CFD result. The influence of the length of the tunnel can be analyzed by comparing the efflux velocity out of bowthruster 1 and bowthruster 2. This is done by comparing the efflux velocity out of the tunnel for test 1 and test 2, see figure 5.6.

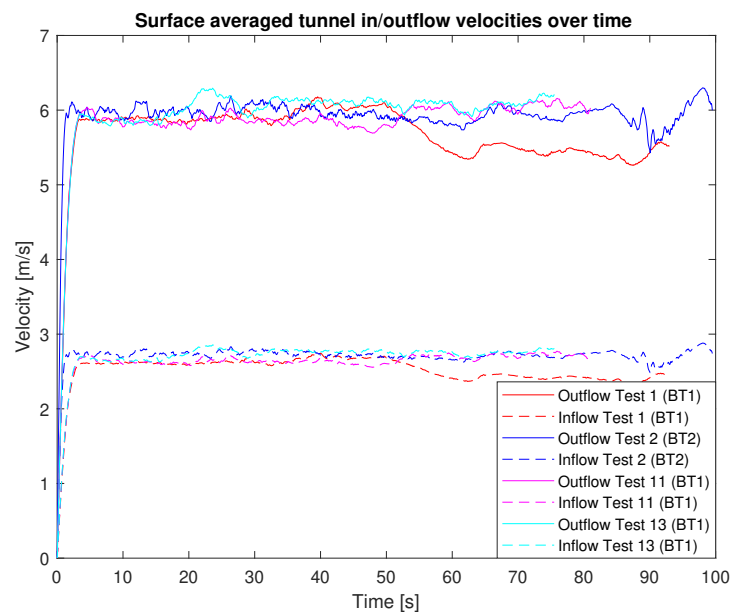


Figure 5.6: Tunnel velocities over time for Test 1 & Test 2

Figure 5.6 shows the surface averaged outflow plane velocities out of all the tunnel thrusters. There is no significant difference in the surface averaged efflux velocity, they all fluctuate around 6 m/s. The inflow velocity is over time exactly 2.2 times smaller than the outflow velocity, which is also the ratio between the surface area of the in- and outflow plane. This ratio is constant due to the mass balance in and out of the tunnel.

The inflow velocity of test 1 drops a little bit after 50 seconds and due to the constant ratio, the efflux velocity drop follows. This has probably something to do with the re-circulation of the jet back into the thruster in combination with the small keel clearance. Test 2 shows more fluctuation in the in- and outflow velocities between 85-100 seconds solution time.

There is no significant difference of the mean value μ between 10-70 seconds of the surface averaged CFD velocity at the outflow plane between both bowthrusters, see table 5.2. However, there is a significant difference in the averaged maximum outflow velocity over time. The maximum outflow velocity is for test 2, which has BT2 activated, much higher in comparison with the other tests, which use BT1. The averaged maximum outflow for test 2 is almost 2 m/s higher than the surface averaged velocity, which is an indication for a non-uniform outflow field. For the tests with BT1 activated, the maximum velocity is less than 1 m/s more than the surface averaged velocity. Unfortunately the surface averaged efflux velocity is not saved over time for BT2 in test 13, so this value misses in table 5.2. The PIANC efflux velocities from both equations 2.11 and 2.10 are also shown in this table. The values

do not differ for the different test cases because the input parameters of the formulae do not change for BT1 and BT2. . The first one, from equation 2.11 is considered as more accurate and is therefore used in the remainder of this thesis for V_0 .

The instantaneous surface averaged tangential velocities in the outflow planes, here $\sqrt{V_x^2 + V_z^2}$, are also given in table 5.2. These tangential velocities are an indication of the amount of swirl in the jet. Unfortunately there were no mean values of the tangential velocities calculated during the simulation. What can be seen is that the tangential velocities are more significant for the shorter tunnel thruster, BT2. This is also indicated by the higher ratio of the tangential over axial velocities for BT2 in comparison with the ratios of BT1. This means that there is more swirl present in the jet out of a shorter tunnel.

		Test 1	Test 2	Test 11	Test 13 [m/s]	
		BT1 [m/s]	BT2 [m/s]	BT1 [m/s]	BT1 [m/s]	BT2 [m/s]
Surface averaged CFD	μ	5.83	5.96	5.89	6.06	-
	σ	0.21	0.09	0.10	0.11	-
Max outflow velocity	μ	6.80	8.87	6.73	7.03	8.63
	σ	0.35	0.59	0.24	0.31	0.42
PIANC efflux velocity	Eqn. 2.11	7.74	7.74	7.74	7.74	7.74
	Eqn. 2.10	8.62	8.62	8.62	8.62	8.62
Instantaneous tangential velocity		0.21	1.58	0.27	0.10	0.63
Ratio $\frac{V_{tangential}}{V_{axial}}$		0.04 [-]	0.26 [-]	0.05 [-]	0.02 [-]	0.11 [-]

Table 5.2: Mean (μ) and standard deviation (σ) of different efflux velocities V_0 between 10-70 seconds from the four CFD simulations are shown in the first 4 rows. The expected efflux velocity by the PIANC guidelines are shown in the following 2 rows. The instantaneous velocity at the end of every simulation is also added at the end of the table for every test case along with the ratio between the instantaneous tangential and axial velocities.

The Reynolds numbers out of the tunnel are between 7.2 - 7.5 million for the different tests, calculated with the surface averaged mean outflow velocity and the characteristic length of the representative diameter of the tunnel, see equation 5.3.

The velocity profiles at the outflow of the tunnels are compared to each other in figures 5.7 and 5.8. The velocity profile of BT1 is more uniform in comparison with the velocity profiles of BT2, since the tunnel of BT1 is much longer and takes out almost all the swirl. The swirl increases the spreading of the jet and this phenomenon can be seen in the velocity fields of the cross sections through the tunnels in figure B.1 in appendix B. There is more spreading out of BT2 compared to the spreading out of BT1.

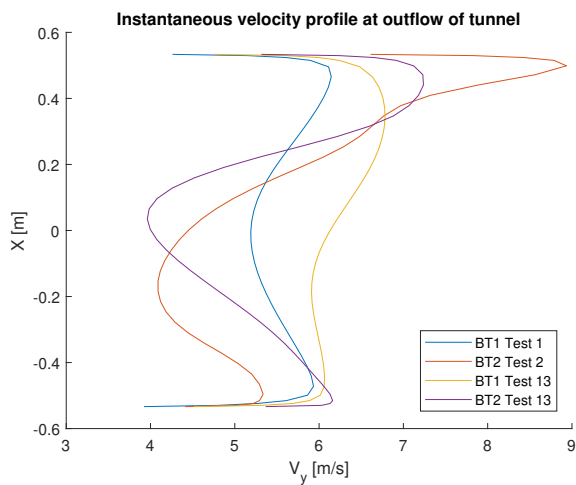


Figure 5.7: Instantaneous velocity profile in x-direction at the outflow plane of tunnel for different tests

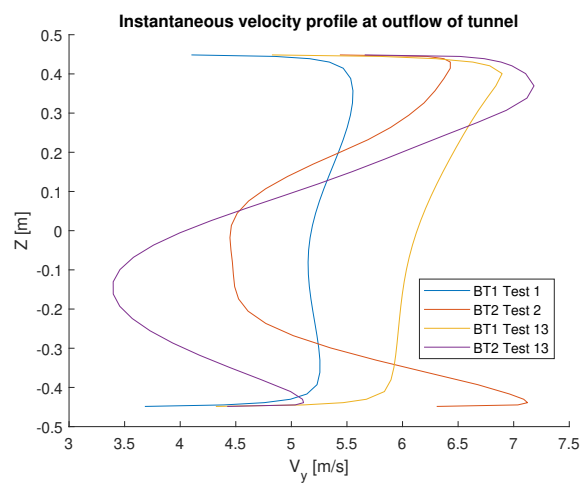


Figure 5.8: Instantaneous velocity profile in z-direction at the outflow plane of tunnel for different tests

Now we know the velocity profile within the tunnel thruster, it is interesting to look at how the flow develops if the jet flows out of the tunnel. The axial velocities for four different planes, each two meters apart, are plotted in figure 5.9. The plane within the tunnel of the ship has a uniform axial flow, only very close to the tunnel walls the velocity drops to zero. The last plane is located 20 centimeter from the wall and as a result the axial velocity drops significantly at this location, because the jet starts to deflect in radial direction.

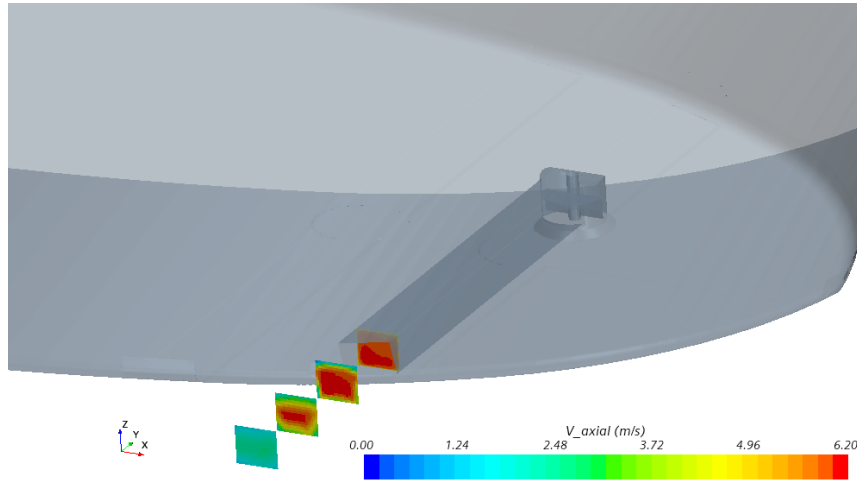


Figure 5.9: Axial velocity distribution at the outflow of the tunnel of BT1

The velocity profiles at the outflow planes of long square shaped tunnels is different from the outflow plane shown in figure 2.5. The flow velocity distribution in the zone of establishment is far more uniform for the 10 meter long bowthruster, see figure 5.10. The blue line represents the last velocity profile within the tunnel and the rightmost red line is 20 centimeter away from the wall and here the velocities are dropped significantly.

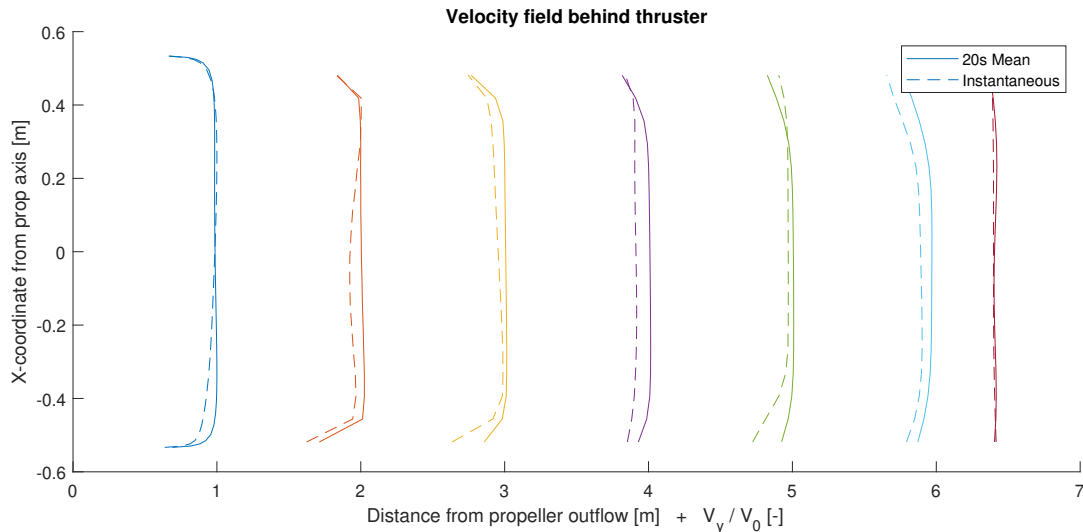


Figure 5.10: The 20s mean and the instantaneous velocity distribution behind BT1

5.3.2. Maximum bottom velocity

The jet flowing out of the tunnel orifice of BT 1 has 3.30 meters before it will hit the quay wall. The jet is spreads radially outwards. The flow which goes downward is subsequently deflected by the bottom after 3.4 meter for the specific case of test 11. The bottom velocity in y- and x-direction of test 11 after 81 seconds is shown in the figures 5.11 and 5.12 respectively.

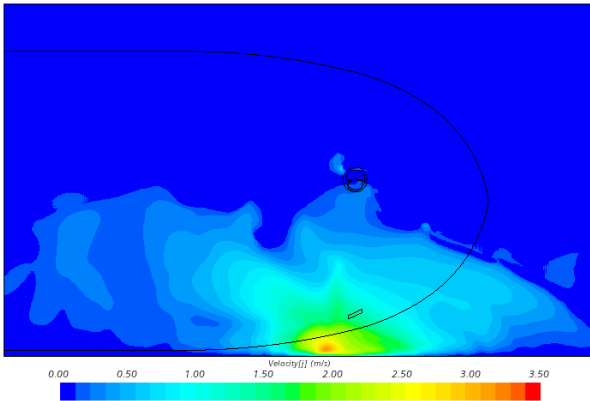


Figure 5.11: Velocity in y-direction 0.5 cm above the bed for Test 11 after 81s

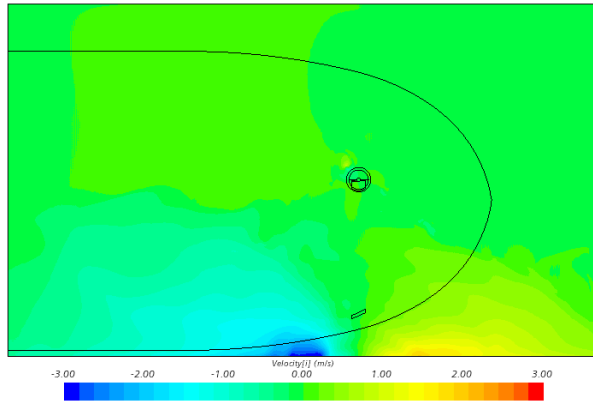


Figure 5.12: Velocity in x-direction 0.5 cm above the bed for Test 11 after 81s

What can be seen is that the maximum velocity is not located right below the bowthruster for test 11, see also figure E.3 in appendix E. Due to the asymmetric hull shape around the tunnel thruster, the volume of water behind the tunnel thruster is much smaller than the volume in front of the tunnel thruster (left and right side of the tunnel in the figures). The mass flow needs to go through a smaller volume, so the velocities become higher. This is also visible in the velocity in x-direction plot in figure 5.12, the velocity in negative x-direction is more significant compared to the positive x-direction velocity. Generally, it can be seen in the simulation that there is a mass flux from right to left at the bottom right corner of the figures over the whole height of the domain. This is also visualized with the near wall velocities in appendix F. The asymmetric hull shape is also the explanation why the maximum bottom velocity in y-direction is not located exactly below the tunnel thruster, but 2.27 meter behind the center line through the tunnel. The other instantaneous near bed velocity fields are also shown in appendix E and for smaller keel clearances, test 1 and 2, the maximum velocity stays more underneath the tunnel.

The maximum bottom velocity obtained from the CFD results are shown in table 5.3 and visualized in figure 5.13 along with the theoretical maximum velocity from equation 2.5 and 2.6 for different efflux velocities. The used efflux velocity in these two equations is of great importance, because it has a significant influence in the theoretical maximum bottom velocity. Only for test 2 the condition of $L/h_t \geq 1.8$ is met.

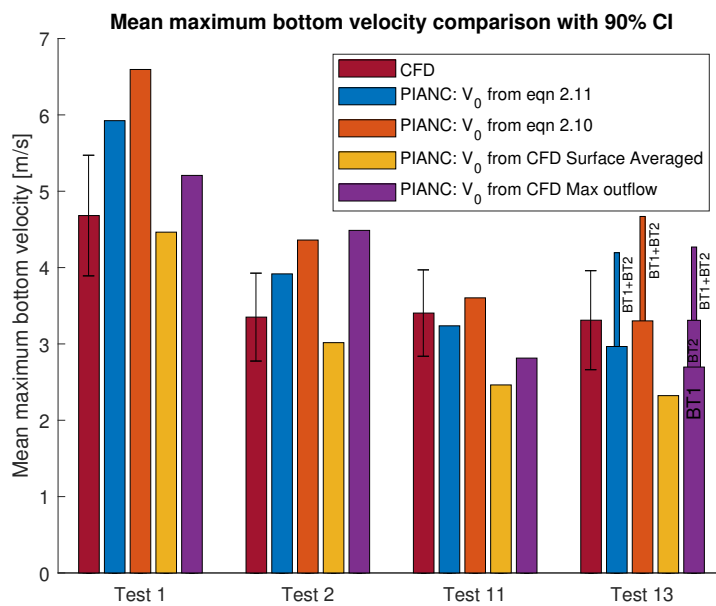


Figure 5.13: Mean of the maximum bottom velocity present on the bottom with 90 % CI for CFD results compared to the PIANC guidelines with different efflux velocities V_0 as input parameter

	V_0	Test 1 [m/s]	Test 2 [m/s]	Test 11 [m/s]	Test 13 [m/s]	
CFD	-	4.68	3.35	3.40	3.17	
PIANC	Eqn. 2.11	5.92	3.92	3.24	BT1:	2.97
					BT2:	2.97
					$\sqrt{BT1^2 + BT2^2}$	4.19
PIANC	Eqn. 2.10	6.59	4.36	3.60	BT1:	3.30
					BT2:	3.30
					$\sqrt{BT1^2 + BT2^2}$	4.67
PIANC	CFD: Surface averaged	4.46	3.02	2.46	BT1:	2.32
					BT2:	-
					$\sqrt{BT1^2 + BT2^2}$	-
PIANC	CFD: Maximum outflow	5.21	4.49	2.81	BT1:	2.70
					BT2:	3.31
					$\sqrt{BT1^2 + BT2^2}$	4.27

Table 5.3: Mean (μ) of the maximum bottom velocity in y-direction between 10-70 seconds of the CFD results with the expected bottom velocity by PIANC for different efflux velocities

Another interesting thing to look at is the velocity degradation following a specific path shown in figure 5.14. The velocity degradation is plotted against the distance travelled in figure 5.15. Along the line Pos 1, the velocity is not decreasing, until it is very close to the wall and goes to zero because of the stagnation point at the center of the wall jet impingement. The velocity along the wall and the bottom is decreasing significantly due to the transfer of momentum to surrounding fluid through turbulence and shear stress as a result of the influence of the wall and bottom. The green plot in figure 5.15 is a translated position 3 line which goes through the maximum bottom velocity. The maximum bottom velocity seems to correspond with the PIANC theory, but keep in mind that these are instantaneous velocities. The results of the other tests, except test 13, can be found in appendix G.

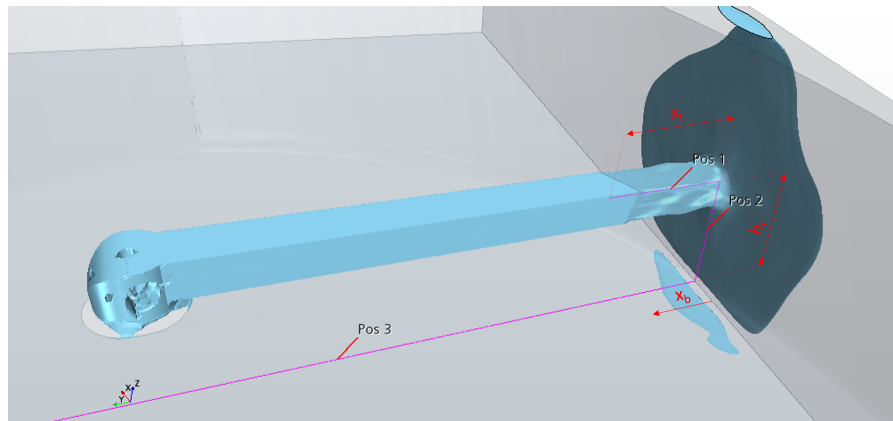


Figure 5.14: Line following a flow direction of the jet for Test 11 after 81s. Here $x_t = 3.30\text{m}$ and $h_t = 3.40\text{m}$.

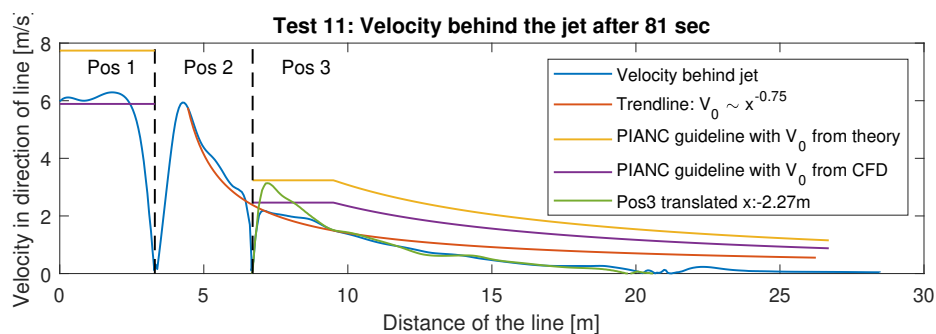


Figure 5.15: Instantaneous velocity degradation along line in Test 11 after 81s

The PIANC guidelines provide two formulae for the maximum velocity in position 1 and 2: equation 2.5 and 2.6. The velocity of the indirect jet along the bottom, position 3, for an increasing x_b can be computed with equation 5.1 and 5.2.

$$V_{b,\max} = 1.0 V_0 \frac{D_{\text{thruster}}}{h_t} \quad \text{for } (L + x_b)/h_t < 1.8 \quad (5.1)$$

$$V_{b,\max} = 2.8 V_0 \frac{D_{\text{thruster}}}{L + h_t + x_b} \quad \text{for } (L + x_b)/h_t \geq 1.8 \quad (5.2)$$

5.4. Independence of location of boundaries

The location of the boundaries could be of influence on the final result of the CFD model. Therefore, it is necessary to check whether the maximum bottom velocity is independent on the location of the imposed boundary conditions. The side boundaries and the boundary on port side are all shifted 5 meters outwards. The whole domain becomes much bigger, and therefore the computing times are also larger, which is disadvantageous. In figure 5.16 the maximum bottom velocity is plotted over time for both the original test 1 and the new model with the boundaries placed further away. Also, the mean values between 10-70 seconds are plotted for the original test case and the new one with further boundaries, the mean values are 4.6815 m/s and 4.7137 m/s respectively, so a 0.7% difference.

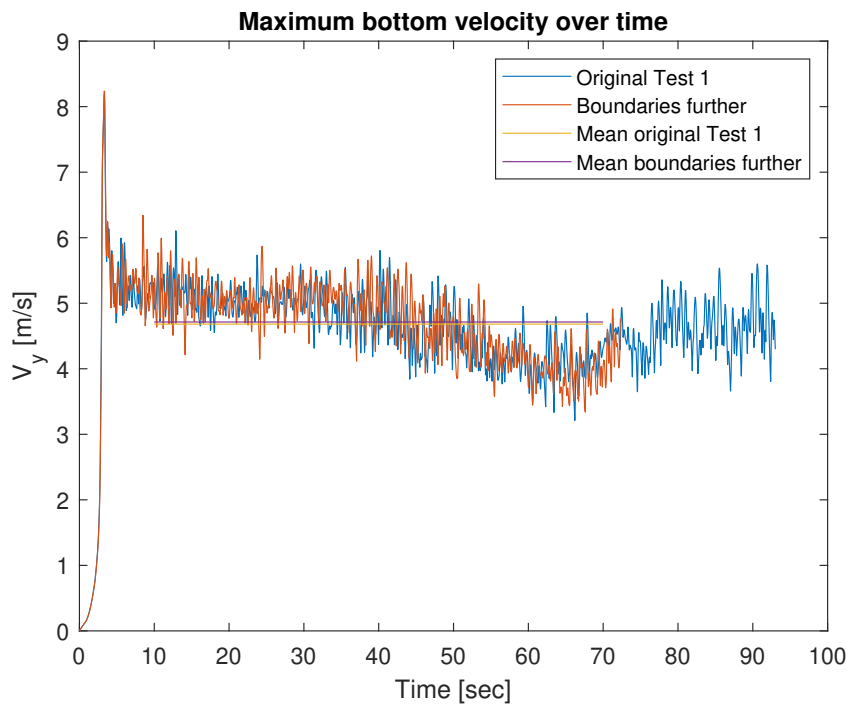


Figure 5.16: Difference in maximum bottom velocity over time with boundaries located further away

The difference between the original run and the new run with the boundaries placed 5m further away is negligible. The same trend over time is observed from figure 5.16 and the mean values differ barely. So, it can be concluded that the boundaries of the original tests are already placed far enough from the momentum source and the influence of the location of the boundary is negligible.

5.5. Wall jet thickness

In this section the wall jet thickness is analyzed and compared to the theory of Rajaratnam [19]. In figure 5.17 the vector field on the x-y plane at a height of the tunnel is plotted. The jet comes out of the tunnel and expands due to shear by the surrounding stagnant water. The jet impinges the quay wall and is deflected radially outwards.

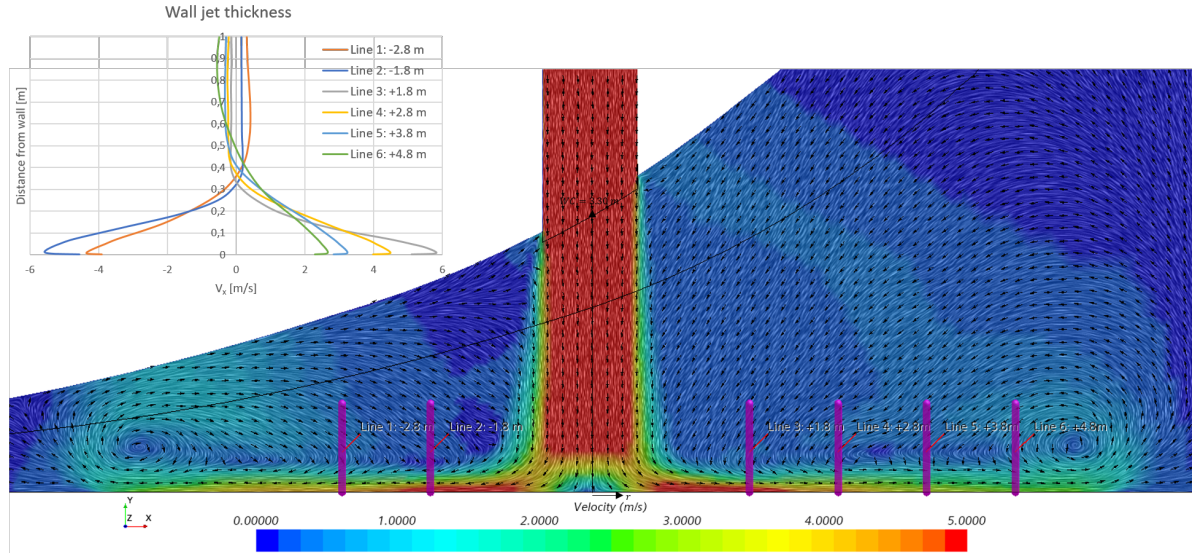


Figure 5.17: Wall jet thickness Test 1 after 7 seconds solution time. In the top left corner a velocity profile for different radial coordinates over the wall normal direction.

The thickness of the wall jet δ is defined as the wall normal distance from the wall to the point where the velocity is half the maximum velocity U_m . The different wall jet thicknesses δ for different radial coordinates r from the jet center line can be found in table 5.4. The non-dimensional wall jet thickness $\bar{\delta}$ is obtained by dividing the thickness by the radius of the initial jet. There is not a defined radius of the jet because the jet is square shaped. Therefore a representative radius is used, see equation 5.3. Here the W_{jet} and H_{jet} are the width and the height of the jet.

$$r_{square} = \sqrt{\frac{W_{jet} \cdot H_{jet}}{\pi}} \quad (5.3)$$

$$\delta = WC \cdot 0.098 \cdot \left(\frac{r}{WC}\right)^{0.9} \quad (5.4)$$

r	δ	$\bar{\delta}$	U_m
1.8 m	0.120 m	0.22 r	5.83 m/s
2.8 m	0.165 m	0.30 r	4.49 m/s
3.8 m	0.203 m	0.37 r	3.24 m/s
4.8 m	0.215 m	0.39 r	2.67 m/s

Table 5.4: Wall jet thickness δ , non-dimensional wall jet thickness $\bar{\delta}$ and the maximum wall jet velocity U_m for different radial coordinates r

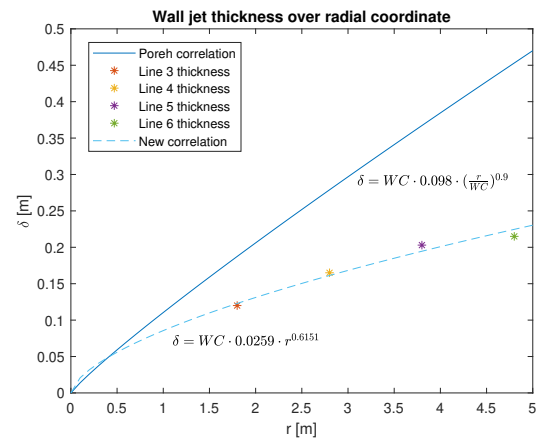


Figure 5.18: Wall jet thickness over radial coordinate

The representative radius for this square shaped jet with the dimensions 1070 x 900 mm is 0.55 meter. The non-dimensional wall thicknesses for the different radial coordinates are shown in the third column of table 5.4. The wall jet thickness becomes bigger with an increasing radial coordinate, because of the shear with the surrounding water. The maximum radial velocity U_m goes down with an increasing radial coordinate, because of dissipation.

Turbulent Jets by Rajaratnam [19] is a collection of many experimental results regarding turbulent jets. The experiments with the radial wall jet produced by an impinging circular jet are presented for the first time by Poreh [18]. The correlation of the thickness that was found can be seen in equation 5.4, WC is here the wall clearance and for test 1 it is equal to 330 cm. The radial wall jet becomes thicker for an increasing radial coordinate. The wall jet thicknesses for different radial coordinates are plotted in figure 5.18 in combination with the correlation found in Poreh. The wall jet in the correlation of Poreh

is thicker compared to the obtained wall thicknesses from the CFD analysis. The peak velocity U_m is located closer to the wall for the CFD results than was found in the experiments of Poreh, this is also visualized in figure 5.19. This figure shows the non-dimensionalized velocity over the radial coordinate. The radial coordinate r is here non-dimensionalized by dividing it with the wall jet thickness δ and the velocity U is normalized by the maximum wall jet velocity U_m .

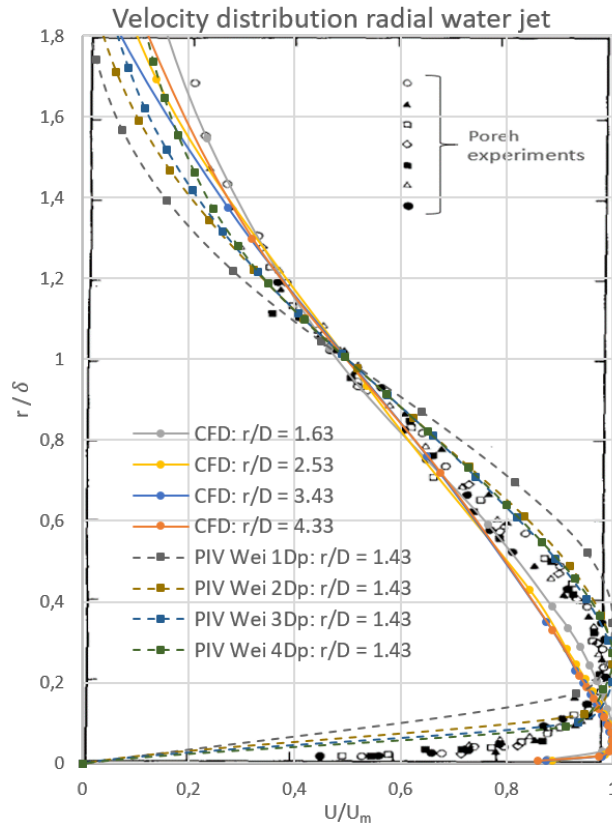


Figure 5.19: Velocity distribution over wall normal direction

Figure 5.19 shows that the CFD results show a significant thinner inner layer thickness of the wall jet in comparison with the experiments of Poreh. The inner layer thickness y_m is the wall normal distance to the location of the maximum wall jet velocity U_m . To increase the validity of the Poreh experiments, the wall jet thickness of the PIV measurements of Wei from chapter 3 are also plotted in figure 5.19, see the dotted lines. For the PIV measurements with a wall clearance of more than $1D_p$, the experiments of Wei show similar inner layer thicknesses as the experiments of Poreh. For the small wall clearance $1D_p$, the inner layer wall jet is significantly thicker, also in comparison with the Poreh experiments. Normally the wall jet thickness δ becomes thicker for an increasing radial coordinate. This is probably due to the fact that the propeller is located too close to the wall and the normal trends are now not visible anymore. For an increasing wall clearance, the wall jet thickness increases.

The scale of the experiments of Poreh [18] is significantly smaller than the scale of the CFD analysis of the Vorstenbosch. The Reynolds number is generally lower at smaller scales, and therefore the viscous forces are generally more dominant than the inertial forces. At larger scales, such as the Vorstenbosch, the inertial forces become more dominant and the Reynolds number goes up. The difference in Reynolds number could explain the difference in the velocity distribution of the radial wall jet, because the viscous forces are more dominant for the smaller scales and therefore the wall jet thickness becomes larger. This theory is invalidated by the fact that the small scale CFD simulation of the Wei experiment also show significant thinner wall jets. So the difference in scale is not the reason for the difference in the wall jet.

The difference in wall jet thickness could be explained by the fact that the walls are simulated as flat boundaries without any roughness and in the real world experiments the walls always have some sort of roughness. Even a rather smooth acrylic plate, in the case of the Wei experiment, has some sort of roughness. From Tachie [26] it is known that the roughness effects the turbulent plane wall jet; an increasing surface roughness enlarges the inner layer thickness y_m of the wall jet.

The wall jet thickness in the CFD analysis could also be influenced by the location of the hull. The volume between the wall and the hull of the ship is limited and therefore the wall jet thickness could become thinner. To draw conclusion about the thickness of the wall jet, more research is needed into this topic.

5.6. Turbulence Intensity

This research focuses on the flow near the bottom because this is of interest for the bottom protection stability. The most important parameter for stone stability is the velocity, but the level of turbulence is also of importance. Figure 5.20 and figure 5.21 show the instantaneous turbulent kinetic energy k and the turbulence intensity I respectively.

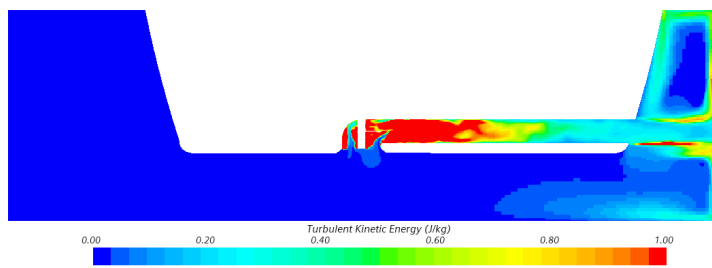


Figure 5.20: Turbulent kinetic energy k for Test 11 after 81s

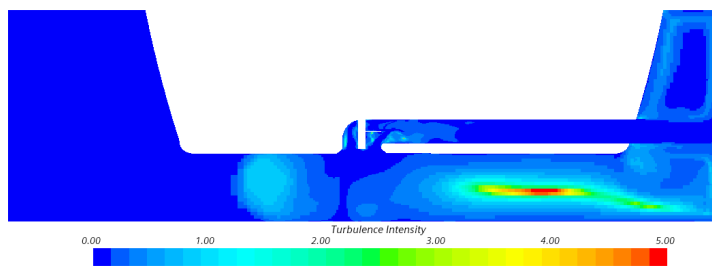


Figure 5.21: Turbulence intensity I for Test 11 after 81s

The turbulent kinetic energy k is especially present within the tunnel and at the boundaries of the jet, because it represents the mean kinetic energy per unit mass associated with eddies in turbulent flow. The turbulent kinetic energy k is below 0.5 J/kg near the bottom.

The turbulence intensity I is the ratio between the turbulent kinetic energy k and the local velocity magnitude, see equation 2.47. Figure 5.21 shows that the turbulence intensity I is high at the locations where the velocity is low. Figure 5.22 shows the turbulence intensity I plotted over the height of the water column at the location of the ADCP1 sensor. The velocity profile is also plotted in this figure, and from this plot it is seen that the turbulence intensity is high at the boundaries of the jet at the surface and especially at the bottom.

In figure 5.23 the turbulent kinetic energy k and the wall shear stress τ_w is plotted at the bottom. The turbulence intensity I could not be plotted at the bottom, because the velocities are zero here. The bed-shear stress could be used to predict the stone stability at the bottom.

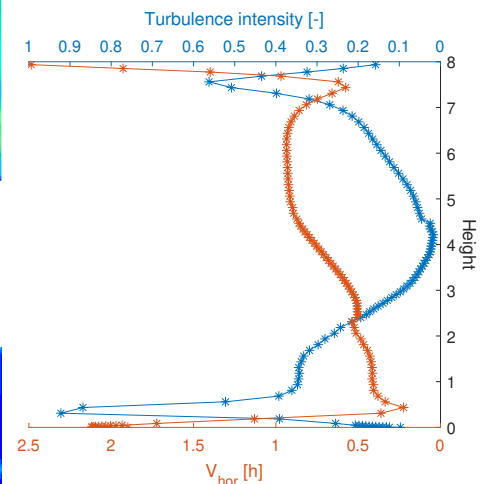


Figure 5.22: Turbulence intensity over height through ADCP1 location of Test 11 after 81s. Note here that this is not in the same plane as shown in figure 5.21.

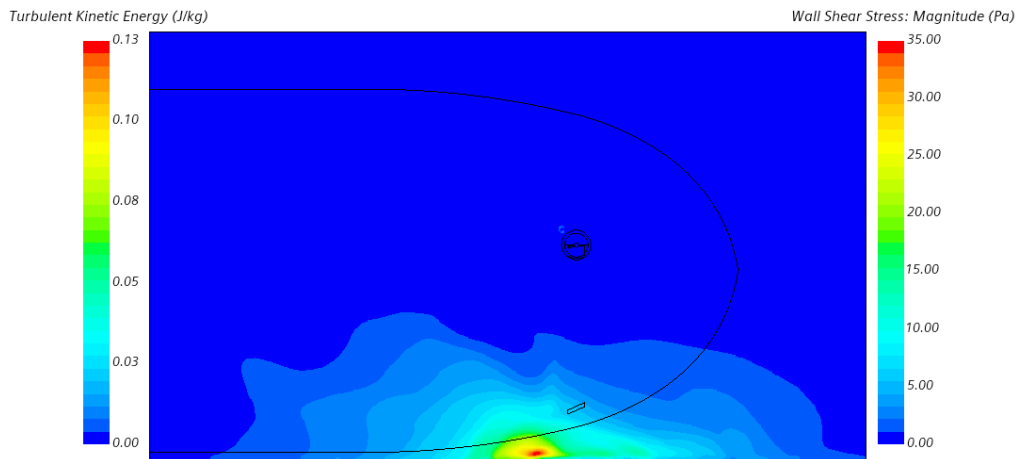


Figure 5.23: Turbulent kinetic energy k and wall shear stress τ_w at the bottom for Test 11 after 81s

5.7. Parameter sensitivity analysis

The parameter sensitivity tests are done to get insights in the effect of a certain parameter on the maximum bottom velocity. The three parameters that are studied in this thesis are shown in table 5.5 with their tested values.

Parameter	Value
Keel clearance	1.03 m
	2.57 m
	4.11 m
Wall clearance	3.30 m
	4.50 m
	5.70 m
Nominal rotation rate	366.67 rpm
	183.33 rpm

Table 5.5: The tested parameters with the varying values

It is expected by the PIANC formulae that the maximum bottom velocity goes down for an increasing keel clearance, because of the increasing distance between the propeller axis and bed h_t , which is in the denominator of equations 2.5 and 2.6. This phenomenon is also present in the parameter sensitivity test of the CFD results, see figure 5.24, but the trend of the PIANC guidelines is more steep than the trend of the CFD results. The trend of the PIANC guidelines goes with $V_{b,\max} \propto h_t^{-1}$ and the trendline through the three CFD points of the wall clearance sensitivity analysis goes with $V_{b,\max} \propto h_t^{-0.63}$. The discrepancies between the PIANC guidelines and the CFD results are more significant for smaller keel clearances. Keep in mind that the distance between the propeller axis and the bed h_t consists of the keel clearance and the distance between the propeller axis and the keel. With an almost quadrupled keel clearance, the bottom velocity goes down with 46%.

The wall clearance sensitivity seems to be less of influence but note that the differences between the tested wall clearances is less in comparison with the tested keel clearances. The maximum tested keel clearance is almost quadrupled in comparison with the smallest tested keel clearance and the maximum wall clearance has not even doubled from the minimum wall clearance. The PIANC guidelines give one and the same maximum bottom velocity for every wall clearance, because the condition of $L/h_t \geq 1.8$ is not met, so the increasing distance between the outflow opening and the quay wall L is not yet present in the formula. With larger L/h_t ratios, the guidelines expect a decrease in the maximum bottom velocity for increasing wall clearances. The power trendline through the three wall clearance points give a $V_{b,\max} \propto L^{-0.22}$ relation, but it is expected that the power decreases for higher wall clearances.

The influence of the nominal rotation rate is also tested in the parameter sensitivity test, but only two runs can be compared due to the lack of cluster space: 100% of the nominal rotation rate n and 50% of rotation rate n . The power of the thruster goes with the rotation rate cubed n^3 , which comes from the relation of the power with the torque: $P = Q\omega$, where $Q = K_q \rho n^2 D^5$ and $\omega = 2\pi n$. The maximum power of the bowthruster is 618 kW at 366.67 rpm, with half of the rotation rate, 183.33 rpm, the power is only 77 kW. The maximum bottom velocity almost halved, which is in line with the expectations from PIANC.

For decreasing rotation rates, the mean surface averaged efflux velocity between 10-70 seconds obviously also decreases, from 5.8883 m/s at 100% rpm to 2.9023 at 50% rpm. Compared to the PIANC guidelines for the efflux velocity, the obtained CFD velocities are quite low; 8.6887 m/s and 4.3699 m/s for 50% and 100% rpm respectively, according to the PIANC guidelines. The ratio between the 100% rpm and 50% efflux velocity are for both the PIANC guidelines and the CFD results the same: a factor of 2.

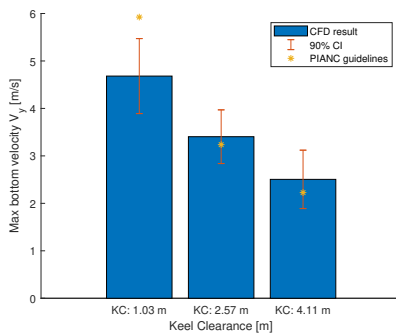


Figure 5.24: Parameter sensitivity of keel clearance

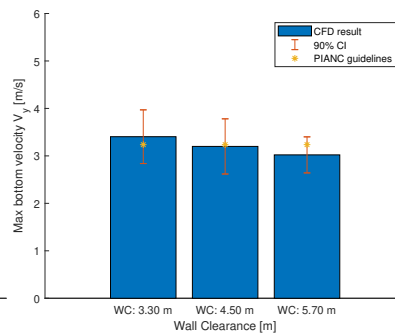


Figure 5.25: Parameter sensitivity of wall clearance

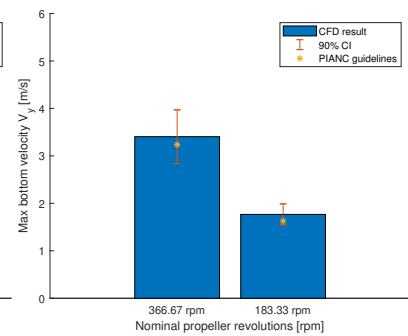


Figure 5.26: Parameter sensitivity of nominal rotation rate

6

Discussion

There are several things that bring up a discussion about the validity of this research, because there are always some discrepancies between the model and the real-world situation. This chapter is meant to discuss the approach of acquiring the results. The points of discussion are listed here.

- The averaging time interval of the CFD results are half as long as the field measurements, the CFD simulation is averaged over 60 seconds and the field measurements over 120 seconds. The averaging error becomes more when the averaged time span will be decreased. To keep the computing time manageable, it is chosen to accept this increased averaging error.

The first 10 seconds are not taken into account in the averaging operation because this is the startup phase of the velocity field. In real life, the ship would already have moved further away from the quay wall after these first 10 seconds, and after a minute the ship would have moved completely away from the quay wall and the influence of the bowthruster at the bottom velocities next to the quay wall has become negligible. During the field measurements the ship was fixed at its position with mooring lines and a two-minute mean velocity is acquired, but in a normal situation the ship sails away and the bottom is exposed for a shorter period to the propeller load. This study calculates the mean velocity field over a longer period of time, because these are needed for the bottom stability calculations.

- The height of the location of the sensor is sensitive to errors because a few centimeters difference in height could double or triple the measured bottom velocity. This is because there is a strong velocity gradient at the top of the bottom jet thickness, which is exactly around the height of the sensor locations. Due to this uncertainty, it is better to interpret the results based on the velocity profiles over the height, see the figures in appendix D.
- In this research the quay wall is represented by a flat wall. The quay wall at the location of the field measurements consists in real life of steel sheet piles, which has a corrugated profile. This corrugated profile has some impact in how the jet spreads out radially outward. This is not included in this CFD model.

The bottom of the domain is also simulated as a no-slip boundary condition without any roughness included. In the real-world situation there is definitely some relief in the bottom profile, since the bottom is covered with some bottom protection which is not flat. The bottom roughness is not included in this research because of two reasons. The first one is that it is unclear how the bottom and wall exactly looked like during the field measurements in 2019. The only information known by the author is that that the bottom of the quay is protected with loose rock of 10-60 kg, partially penetrated with colloidal concrete. The median nominal diameter D_{75} of loose rock of 10-60 kg is somewhere between 0.21 - 0.26 m [32], but since it is partly penetrated with colloidal

concrete, this value could be smaller. This brings us to the second reason why the roughness is not included in this research, because it is not easy to add a roughness corresponding to the roughness of loose rock with a diameter of around 0.25 m.

In STAR-CCM+, the roughness could be included easily in the cells adjacent to the bottom if the roughness heights are in the order of magnitude of sand grains. The roughness height may not exceed the cell height of the first layer of cells adjacent to the boundary. The rule of thumb is that the roughness height is equal to 2 times the D_{n50} value [25]. This means that the first layer of cells above the boundary needs to be in the order of magnitude of 0.5 m, which is far more than the wall jet thickness. Since the cell sizes adjacent to the bottom are in the order of magnitude of 1 mm in this model, the 0.5 meter roughness height is far too much to simulate it this way.

This means that this method is not well suited to simulate large rocks at the bottom. See appendix H for a more detailed elaboration on how the roughness of small grain sizes can be simulated in STAR-CCM+. If the roughness would be included, the shear stresses will increase near the bottom and the transfer of momentum to surrounding fluid through turbulence will increase. As a result the inner layer thickness of the jet becomes thicker, so the velocity profile normal to the wall and bottom becomes broader. This could potentially have a big influence on the measured velocities at the sensor locations.

- Due to the lack of adequate guidelines for the efflux velocity out of a tunnel thruster, there are some discrepancies between the CFD results and the PIANC guidelines. The efflux velocity formulae do not consider any cross-sectional area of the tunnel, and the ratio between the cross sectional area at the propeller and the cross-sectional area of the tunnel should be included. The mass balance forces the water to accelerate due to the smaller sectional area of the tunnel. The formulae of the PIANC theory are not covering this issue.

The efflux velocities of the tunnel thrusters are unknown from the field measurements of 2019, which is unfortunate, because an extra benchmark for the thrusters would increase the validity of this research. Matching the propeller thrust does not necessarily have to mean that the efflux velocity is matching. The uncertainties concerning the efflux velocity influence the validity of the comparison of the maximum bottom velocity from the CFD results with the PIANC guidelines.

- There was no 3D geometry of the MTS Vorstenbosch available and therefore another inland vessel geometry is picked and adjusted to the Vorstenbosch dimensions, but this is not a 1 to 1 copy. The hull was adjusted for a second time to make sure that the distance of the bowthruster to the wall is exactly the same for CFD model as during the field measurements.

The exact geometry of the tunnel thrusters is not known, so the dimensions of the guide vanes and flow deflectors within the thruster are not exactly known.

- This study only considers one type of inland vessel, with one particular bowthruster. This makes it harder to draw general conclusions for different kinds of inland vessels, and even harder for seagoing vessels. Since the Vorstenbosch is one of the biggest, if not the biggest inland vessel on the Dutch waterways, the bowthruster will be relatively powerful in comparison with other inland bowthrusters. Therefore, the conclusions of this study will be conservative for a general inland vessel.
- The near bed bottom velocity can also be affected by the propeller in the inlet, especially for small keel clearances, see for example figure E.1 in appendix E. The bottom velocities are maximum right under the inlet for Test 1, where the keel clearance is only 1.03 m. This is not explicitly studied in this thesis, but for future designs of quay walls where ships moor with a large draft and a tunnel inlet at the bottom, this should be considered as a potential threat for scour holes.

- Some of the plots shown in this thesis are instantaneous snapshots of a flow field at a certain solution time. Most of the time it is more interesting to have a mean flow field over a certain time period. Unfortunately it is computationally expensive to save every variable over all the time steps and therefore deemed unfeasible for this thesis. However, the new simulations necessary for the parameter sensitivity analysis include some 20 second averaged flow field information. Some plots can be found in appendix I. The conclusion is that the instantaneous snapshots do not show large discrepancies with the mean flow field. Therefore, the instantaneous snapshots are considered as acceptable and as representative for the flow field.
- The free surface could be modelled as a Volume of Fluid (VOF) method instead of slip boundary condition. This could potentially influence the bottom velocity.
- During the field measurements, the velocity field near the bottom could be disturbed by the construction at which the sensors are mounted at the field measurements of 2019.

7

Conclusion

The goal of this research was to develop a full-scale numerical model that simulates the field measurements done in 2019, where the near-bed flow induced by a bowthruster of an inland vessel next to a quay wall is analyzed. The purpose was to create a better understanding of how the jet out of a bowthruster develops near a quay wall. This would contribute to the accuracy of the design guidelines for bottom protection against erosion.

7.1. Research questions

In this section, the answers are given for the research questions, starting off with the sub-questions and hereafter the main research question can be answered.

What is the best way to implement the bow thruster propeller into the numerical model?

There are several ways to implement a marine propeller into a CFD model, but the best way for this specific case is to implement the propeller with a virtual disk, modelled with the body force method within STAR-CCM+. This method is best suited for the marine applications, because this method adds momentum and swirl to the water. The computing times are relatively small compared to the computing times of the moving reference frame method, which makes it out of practical considerations more suited for marine applications. The moving reference frame method was in addition impossible to implement, because there was not an exact geometry of the bowthruster of the MTS Vorstenbosch available, which is necessary to include in the mesh.

What turbulence model is best suited in this CFD model?

It is preferred to use the RANS equation in combination with the $k - \omega$ turbulence model for this specific case with small keel- and wall-clearances. The RANS equations are preferred over the DNS and LES methods due to computing times. The model consists of 7 million+ cells in the mesh, so an accurate DNS or LES simulation is not feasible in the regulative time for this thesis. The $k - \omega$ turbulence model showed the best behavior for a jet impinging to a quay wall with small keel- and wall clearances. The Spalart-Allmaras and the $k - \epsilon$ turbulence model showed some irregularities in the simulation after recirculation of the jet back into the virtual disk. The computing costs of the Reynolds Stress turbulence model were considered as too expensive for this thesis.

How does the numerical model relate to the field measurements of 2019?

The field measurements indicated that the bottom velocities were lower than were expected beforehand. These CFD results of the Vorstenbosch give much more insights in how the flow develops after impinging at the quay wall. The thickness of the jet at the bottom is relative thin and this study shows that the sensors were placed too far above the bed and they did not measure the peak velocity over the height of the domain. This also explains the relative low velocities during the field measurements compared to the expected maximum velocities at the bottom. The maximum bottom velocity is located more towards the bottom.

How do the current PIANC guidelines relate to the obtained near-bed flow velocities of the numerical model?

The current PIANC guidelines with the theoretical efflux velocity are related to some of the CFD tests. For tests 2, 11 and 13 the maximum bottom velocity of the PIANC guidelines are within the 90% confidence interval of the mean from the CFD results. For test 1 with a small keel clearance, the PIANC guidelines are conservative, with an overestimation of more than 1 m/s. It should be noted here that the efflux velocity used in the PIANC formulae deviate from the obtained efflux velocities from the CFD analysis.

What input parameter affects the total near-bed flow field the most?

The parameter sensitivity analysis gives an insight in what influence the specified parameter has on the maximum bottom velocity. From the executed CFD simulations, the keel clearance appears to be the most sensitive parameter; with an almost quadrupled keel clearance, the bottom velocity goes down with 46%.

How do the relative low bed flow velocities of the full-scale field measurements relate to the bed velocities of a numerical model and how does the bow thruster jet of an inland vessel evolve at the quay and bottom?

The bottom velocities measured during the field test of 2019 with the MTS Vorstenbosch were lower than expected by the guidelines provided by PIANC. With the use of a numerical model, this flow field is made more insightful and this study comes to the conclusion that it is hard to measure the peak velocity of the bottom jet, because this bottom jet is relatively thin. It is expected that during the field measurements the sensors did not catch the maximum bottom velocity.

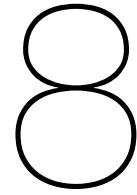
The jet which comes out of the tunnel is for larger tunnels more uniform than for smaller tunnels. It stays quite square shaped until it hits the wall and deflects radially outward. The wall jet becomes thin and will partly bump into the bottom. The water will deflect and follows the bottom in normal direction of the quay wall. The velocity of the jet decreases due to the transfer of momentum to surrounding fluid through turbulence and shear stress as a result of the influence of the wall and bottom. The maximum bottom velocity is positioned close to the wall and does not necessarily have to be in the line extending from the axis from the tunnel. For small keel clearances the bottom velocity underneath the inlet could also influence the bed stability.

7.2. General conclusions

The use of CFD is a good method to get more insights in how the bow thruster jet develops and how it is deflected by a quay wall. The obtained bottom velocities are generally not far from the predicted bottom velocities by the PIANC guidelines. A civil engineer or bottom protection specialist can use the bottom velocities and the turbulence intensity in this thesis to predict till what extend bottom protection is necessary.

The wall jet thickness is rather thin in the CFD simulations compared to the experiments in literature, because the CFD model simulates the walls without any roughness. When the roughness is included in the model, the inner layer thickness of the wall and bottom jet will increase.

A long tunnel takes out the swirl of the propeller jet and the outflow velocity profile becomes uniform and consists of only axial velocities.



Recommendations

This study comes with some recommendations for the industry and for further research and they are listed here.

- With the low near bed velocities obtained during the field measurements of 2019 with the MTS Vorstenbosch, it seems tempting to implement less robust bottom protection in the future, because it does not have to withstand high bottom velocities. This study does not recommend that, because there are locally high velocities near the bottom, but the jet may be thin. It is hard to position the velocity sensors during a field measurement at the right location of maximum bottom velocity within the thin bottom jet. With the trend of larger vessels and decreasing keel clearances, it is not recommended to economize on the bottom protection at quay walls.
- It is recommended that the near bed velocities under the inlet of the tunnel thruster are studied more explicitly, to avoid scour holes beneath the inlet of the tunnel induced by the propeller. For small keel clearances the bottom velocities underneath the inlet are considerable.
- In this specific case, a big inland tanker was analyzed, but the conclusions drawn in this study do not have to hold for all kinds of vessels with even more different types of bowthrusters. To generalize these conclusions, more types of bowthrusters on different kinds of vessels need to be analyzed.
- It is recommended to measure the efflux velocity during the future field tests, to have an extra validation benchmark for a CFD model. During the last field measurements of September 2020, the efflux velocity was measured and this could be an important setpoint to make sure that the bowthruster in the CFD model is set up with the same conditions. It is also recommended to do more research into the efflux velocity of tunnel thrusters, to come up with new design guidelines for specific types of bowthrusters, which includes a new formula with the ratio between the cross-sectional area of the propeller and the outflow of the tunnel for tunnel thrusters.
- It is also recommended to do more research into the thickness of the wall jet. The effect of wall roughness on this thickness is of specific interest. It is hard to draw conclusions about the jet thickness, since this study only touches briefly on this topic.
- The wall and the bottom of the domain are simulated with no-slip boundary conditions. This means that the velocity profile near a wall reaches zero at the wall. The walls are simulated as smooth walls, while the walls and especially the bottom have some roughness in real life. There are three options to include the roughness of the loose rock of 10-60 kg into a numerical model for future research:

- Make the first layer of cells adjacent to the bottom boundary much larger till the roughness height fits within the first layer of cell height. The big disadvantage of this method, in this study, is that this cell height covers the whole wall jet thickness, so the velocity profile near the wall lays within one layer of cells.
- Include the whole rough bottom geometry within the mesh. Since the sizes, shapes and spacing of most bottom protections are random, it is hard to include an exact copy of the real-world situation. But it is possible to include a uniform disturbance in the bottom geometry, like is done in figure 8.1.

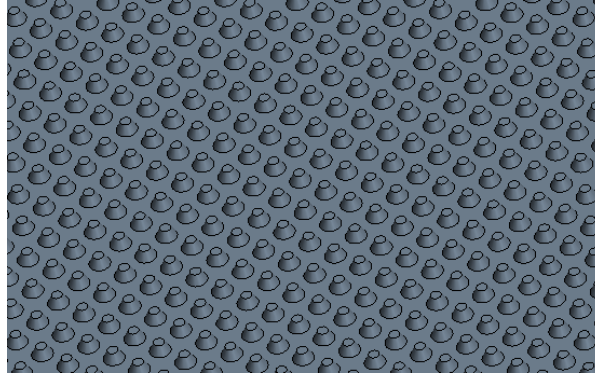


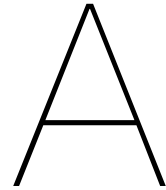
Figure 8.1: Include the surface roughness geometry in the mesh

- It is also possible to add some wall shear stress to the bottom by implementing a porous membrane at the bottom. This is done by dividing the domain into two regions with a porous baffle interface at a height above the bottom which is representative for the roughness height. A shear stress based method is suited for applications where the flow is mostly tangential to the baffle. The porosity needs to be chosen and can be based on the ratio between the area of impermeable rock and the area between the rocks. The porosity value for including large rocks bottom roughness should be much lower than for wire screens. Turbulent eddies can penetrate through the baffle, if the baffle pores are larger than the turbulent scales. The resistance can be added by specifying the porous inertial resistance and the porous viscous resistance.
- It would help if there was an accurate 3D model of the Vorstenbosch available, to give a more accurate representation of the flow around the actual ship. It would also be beneficial if there was more information available of the bowthruster in the ship, especially on the details of how the flow is deflected into the tunnel from the inlet.
- It is recommended to have a clear goal which parameters are needed to make good estimations of the bottom protections that is needed. In this case it is assumed that a averaged values of the bottom velocity is needed in combination of turbulence intensity values near the bottom. There are a lot of methods to estimate the bottom protection which all use different input parameters. It is recommended to define beforehand which parameters are of interest for future CFD work.

Bibliography

- [1] M.L. Albertson, R.A. Jensen, and H. Rouse. *Diffusion of submerged jets*. 1950.
- [2] E.A. Van Blaaderen. Modelling bowthruuster induced flow near a quay-wall - MSc Thesis. 2006.
- [3] H. G. Blaauw and E. J. van de Kaa. Erosion of bottom and sloping banks caused by the screw race of manoeuvring ships. *Delft, the Netherlands, Delft Hydraul. Lab., Jul.1978, (202)* (Paper presented at the 7th Int. Harbour Congress, Antwerp, May 22-26, 1978)), 1978.
- [4] T. Blokland. Bodembescherming belast door schroefstralen. Huidige ontwerpmethod, 1997.
- [5] T. Blokland and Ingenieursbureau Havenwerken. Schroefstraak tegen kademuur, 1996. URL <http://resolver.tudelft.nl/uuid:17f2b64b-e5b8-43c4-b13c-957fa7fc477d>.
- [6] A. Bok. De stabiliteit van de bodembescherming voor een kademuur bij het gebruik van boegschroeven - MSc Thesis. 1996.
- [7] I. Cantoni. Bowthruuster-induced flow on the bottom of a vertical quay wall - MSc Thesis. 2020.
- [8] J. De Jong. Numerical modelling of bow thrusters at open quay structures - MSc Thesis. 2014.
- [9] M. De Jong. Schade veroorzaakt door boegschroeven van manoeuvrerende schepen bij verticale kademuren - MSc Thesis. 2003.
- [10] M. Fuehrer, K. Römish, and G. Engelke. Criteria for dimensioning the bottom and slope protections and for applying the new methods of protecting navigation canals. *PIANC XXVth Congress, Section I*, 1981.
- [11] Trimble Inc. Tanker | 3d warehouse, 11 2017. URL <https://3dwarehouse.sketchup.com/model/ba7d89b5-bb66-4539-95b5-23f88b2968a0/Tanker>.
- [12] ITTC. ITTC - Recommended Procedures. *Ittc*, 7.5-02(03-01.5):1–10, 2002.
- [13] B.E. Launder and B.I. Sharma. Application of the energy-dissipation model of turbulence to the calculation of flow near a spinning disc. *Letters in Heat and Mass Transfer*, 1(2):131 – 137, 1974. ISSN 0094-4548. doi: [https://doi.org/10.1016/0094-4548\(74\)90150-7](https://doi.org/10.1016/0094-4548(74)90150-7).
- [14] A.F. Molland and S.R. Turnock. 6 - theoretical and numerical methods. In A. F. Molland and S. R. Turnock, editors, *Marine Rudders and Control Surfaces*, pages 233–311. Butterworth-Heinemann, Oxford, 2007. ISBN 978-0-7506-6944-3. URL <https://www.sciencedirect.com/science/article/pii/B9780750669443500093>.
- [15] B. Nielsen. Bowthruuster-induced Damage - MSc Thesis. 2005.
- [16] A. M. Nodeland. Wake Modelling using an actuator disk model in openFOAM. 2013.
- [17] PIANC. *Report No180. Guidelines for Protecting Berthing Structures from Scour Caused by Ships*. 2015. ISBN 9782872232239.
- [18] M. Poreh, Y. G. Tsuei, and J. E. Cermak. Investigation of a turbulent radial wall jet. *Journal of Applied Mechanics, Transactions ASME*, 34:457–463, 6 1964. ISSN 15289036. doi: 10.1115/1.3607705.
- [19] N. Rajaratnam. *Turbulent Jets*. ISSN. Elsevier Science, 1976. ISBN 9780080869964. URL <https://books.google.nl/books?id=g3R4gFObz1oC>.
- [20] K. Ren, Junling Hu, Xingguo Xiong, Linfeng Zhang, and J. Wei. Validation of turbulence models in star-ccm+ by n.a.c.a. 23012 airfoil characteristics. 04 2009.

- [21] T. Schaap. Changing the cross-sectional geometry of a bow tunnel thruster - MSc Thesis. 2015.
- [22] E. Schmidt. *Ausbreitungsverhalten und Erosionswirkung eines Bugpropellerstrahles vor einer Kaiwand*. Leichtweiss-Institut für Wasserbau Braunschweig: Mitteilungen. Leichtweiß-Inst. für Wasserbau, 1998. URL https://books.google.nl/books?id=gi_dYgEACAAJ.
- [23] L. A. Schokking. Bowthruster-induced Damage - MSc Thesis. 2002.
- [24] Siemens. Simcenter star-ccm+ 2020.1, 2020. URL https://docs.sw.siemens.com/en-US/product/226870983/doc/PL20200227072959152.userGuide_html_2020.1/custom/. [Online; accessed August 16, 2020].
- [25] T. Stevens. The prediction of stone stability by a three-dimensional eddy resolving simulation technique, 2018. URL <http://repository.tudelft.nl/>.
- [26] M. F. Tachie, R. Balachandar, and D. J. Bergstrom. Roughness effects on turbulent plane wall jets in an open channel. *Experiments in Fluids*, 37:281–292, 2004. ISSN 07234864. doi: 10.1007/s00348-004-0816-0.
- [27] A. Van den Brink. Modelling Scour Depth at Quay Walls due to Thrusters - MSc Thesis. 2014.
- [28] T. Van der Laan. Het ontwikkelen van een model voor boegschroefstralen bij verticale kademuren - MSc Thesis. 2005.
- [29] R. Van Doorn. Bow Thruster Currents at Open Quay Constructions on Piles - MSc Thesis. 2012.
- [30] R.F.A. Van Noort. Bow thruster velocities at multiple bank slope configurations and the stability of slope material - MSc Thesis. 2017.
- [31] V.J.C.G.L. Van Veldhoven. Vooronderzoek schroefstraal op een talud met breuksteen - MSc Thesis. 2002.
- [32] K. Verelst, J. B. Vercruyssen, E. Taverniers, T. De Mulder, J. Verwilligen, P. Peeters, and F. Mostaert. Ondersteuning ontwerp klasse Vb-sluis te Sint-Baafs-Vijve: deelrapport 4. Dimensionering bodembescherming stuwsluis. 12_142_4, 2016.
- [33] H.J. Verhey and Waterloopkundig Laboratorium. *The Stability of Bottom and Banks Subjected to the Velocities in the Propeller Jet Behind Ships: Presented at the 8th International Harbour Congress, Antwerp, Belgium, June 13-17, 1983*. Publication (Waterloopkundig Laboratorium (Delft, Netherlands)). Waterloopkundig Laboratorium, 1983. URL <https://books.google.nl/books?id=-1dCvgAACAAJ>.
- [34] H. K. Versteeg and W. Malalasekera. *An introduction to computational fluid dynamics - the finite volume method*. Pearson, 1995. ISBN 978-0-13-127498-3.
- [35] Veth Propulsion . Veth tunnel thruster, 2020. URL <https://www.vethpropulsion.com/products/bow-thrusters/tunnel-thruster/>. [Online; accessed June 30, 2020].
- [36] M. Wei and Y. Chiew. Impingement of propeller jet on a vertical quay wall. *Ocean Engineering*, 183: 73 – 86, 2019. ISSN 0029-8018. doi: <https://doi.org/10.1016/j.oceaneng.2019.04.071>. URL <http://www.sciencedirect.com/science/article/pii/S0029801819301994>.



German free jet velocity distribution

The free jet velocity distribution equations A.1, A.2 and A.3 are based on the work of Fuehrer, Römisch and Engelke [10].

$$V_{axis} = V_0 \quad \text{for } \frac{x}{D_p} < 2.6 \quad (\text{zone of flow establishment}) \quad (\text{A.1})$$

$$V_{axis} = 2.6 V_0 \left(\frac{D_p}{x} \right) \quad \text{for } \frac{x}{D_p} > 2.6 \quad (\text{zone of established flow}) \quad (\text{A.2})$$

$$\frac{V_{x,r}}{V_{axis}} = \exp\left(-22.2 \frac{r^2}{x^2}\right) \quad (\text{A.3})$$

B

Velocity field all tests

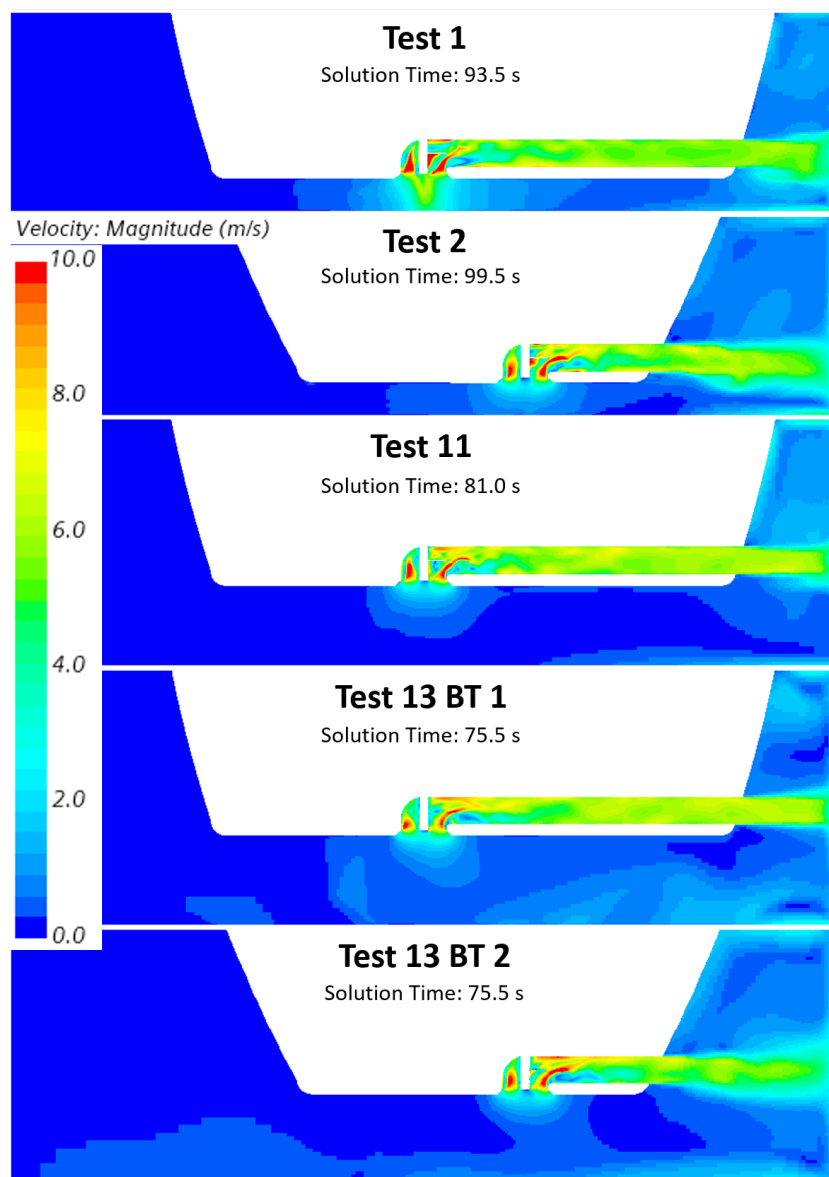
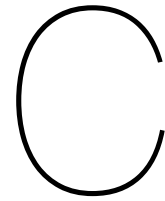


Figure B.1: Instantaneous velocity field trough bowthruster



Sensor convergence

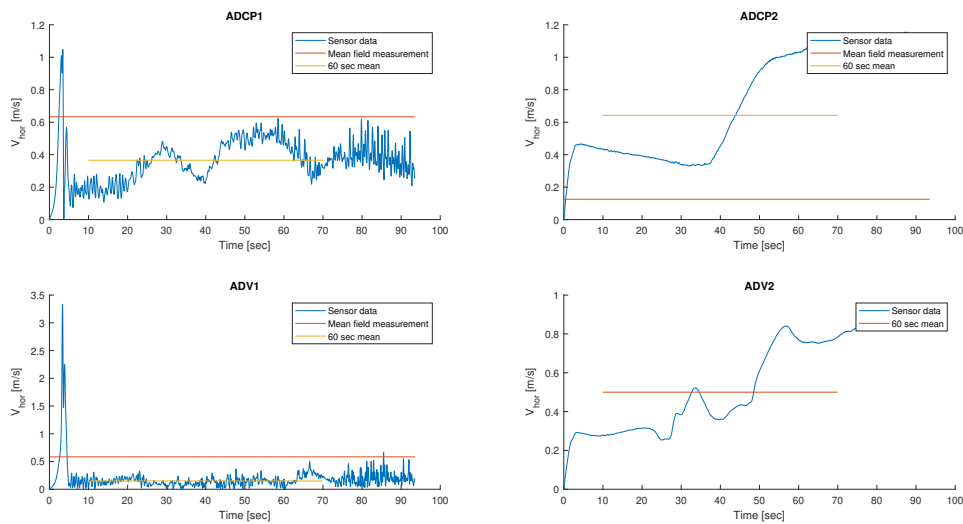


Figure C.1: Horizontal velocity at sensor location over time for test 1

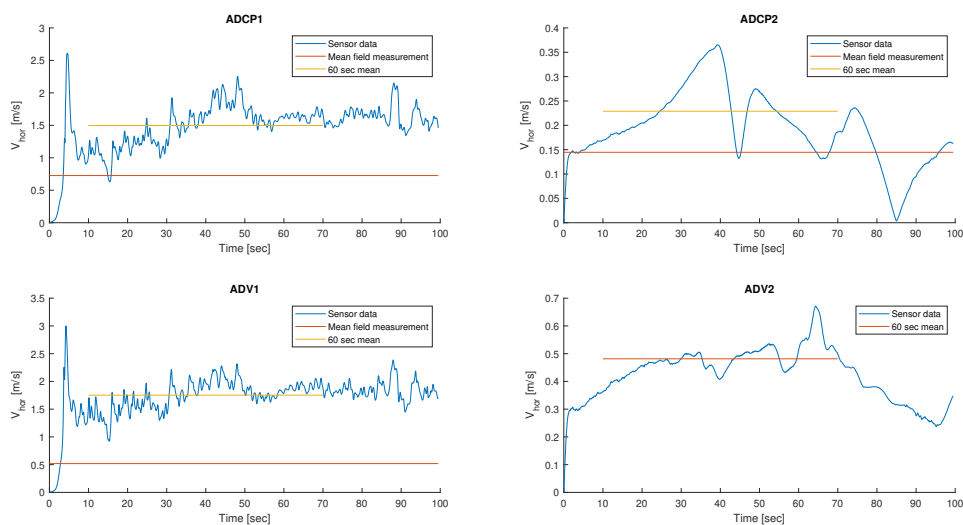


Figure C.2: Horizontal velocity at sensor location over time for test 2

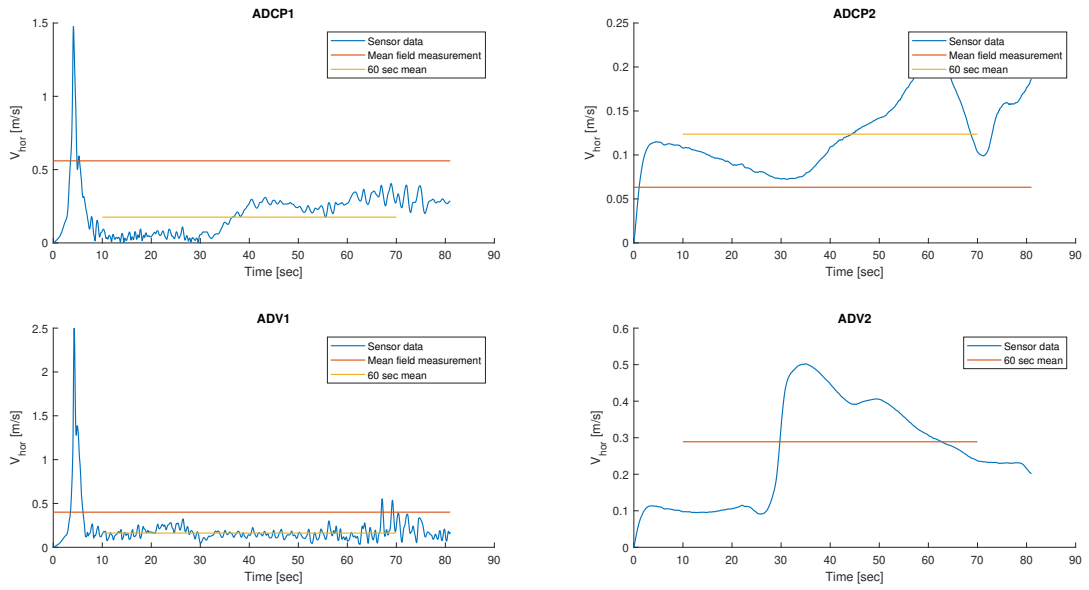


Figure C.3: Horizontal velocity at sensor location over time for test 11

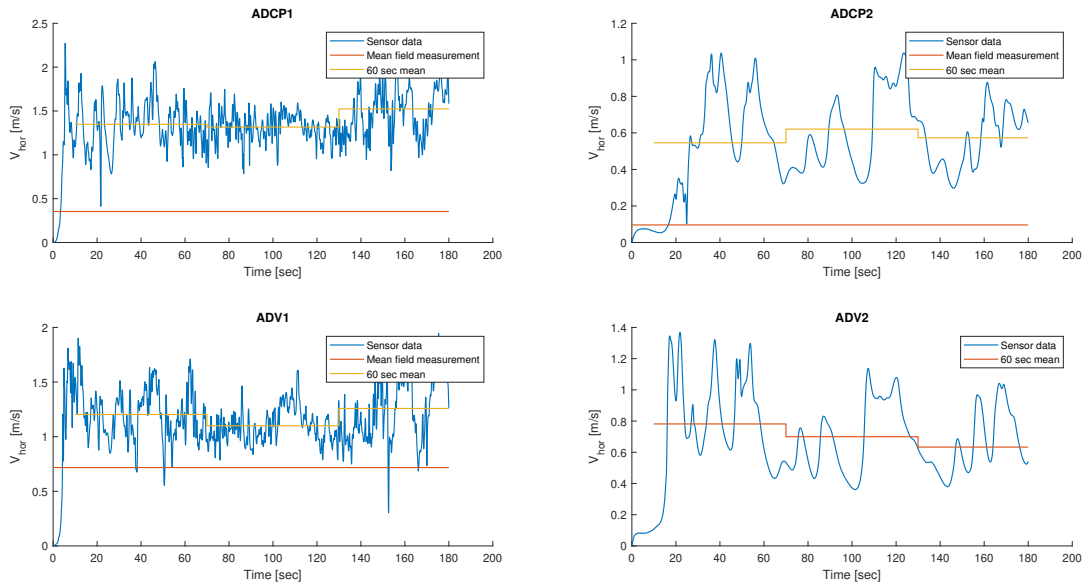
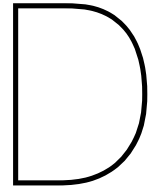


Figure C.4: Horizontal velocity at sensor location over time for test 13



Velocity profiles

In this appendix all the velocity profiles through the sensor locations of all the different tests are plotted.

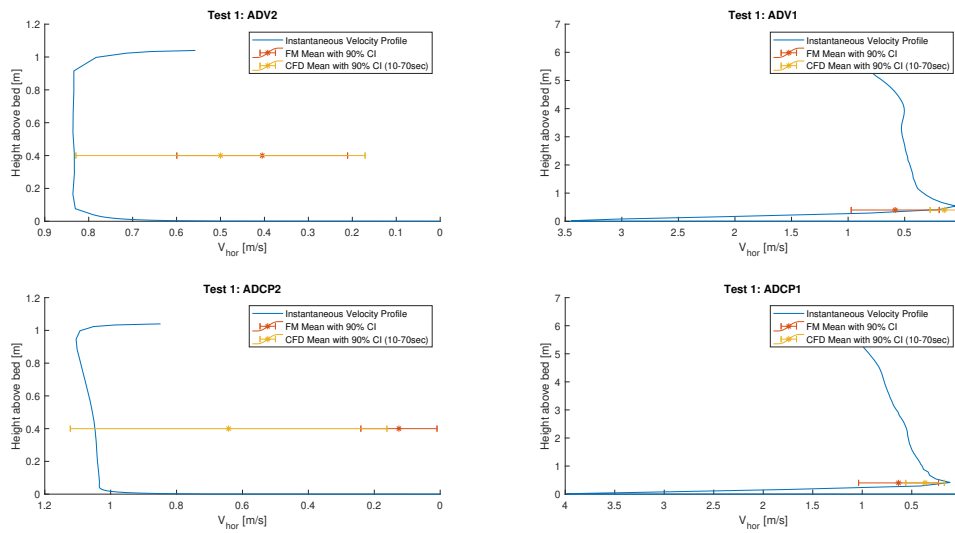


Figure D.1: Velocity profile through sensor locations Test 1 after 93s

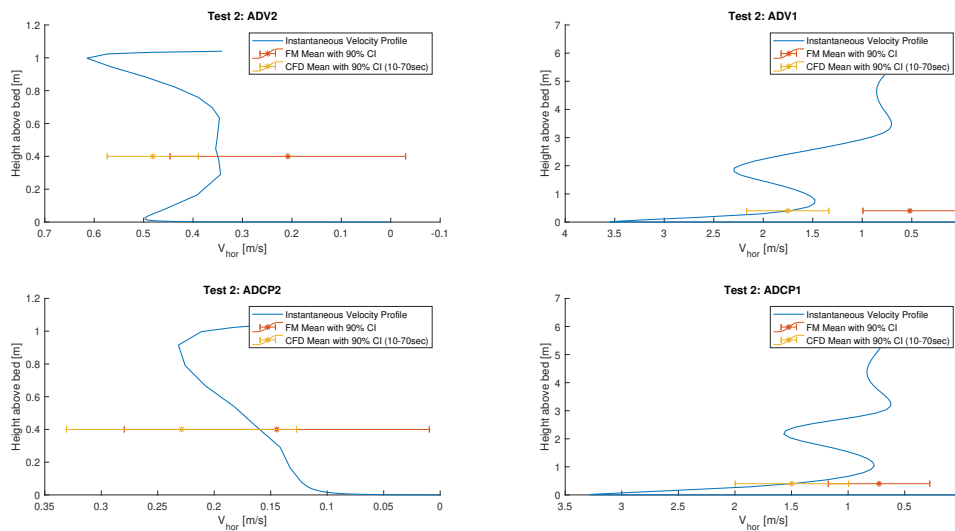


Figure D.2: Velocity profile through sensor locations Test 2 after 99s

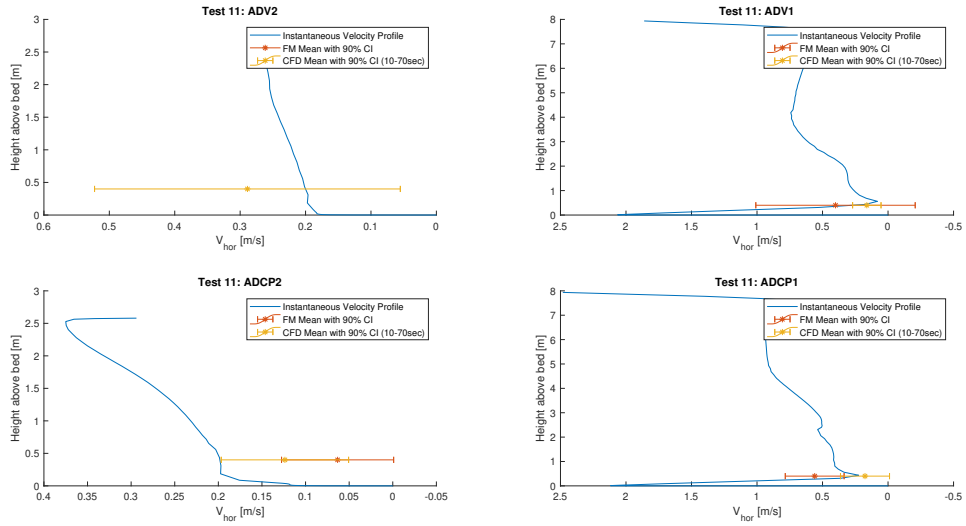


Figure D.3: Velocity profile through sensor locations Test 11 after 81s

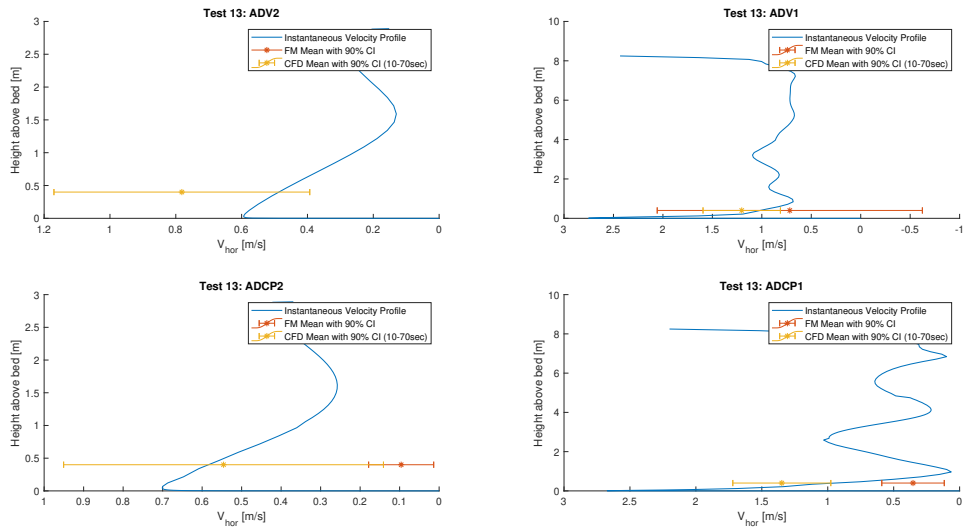
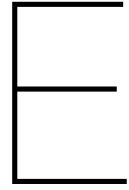


Figure D.4: Velocity profile through sensor locations Test 13 after 80s



Bottom velocity field

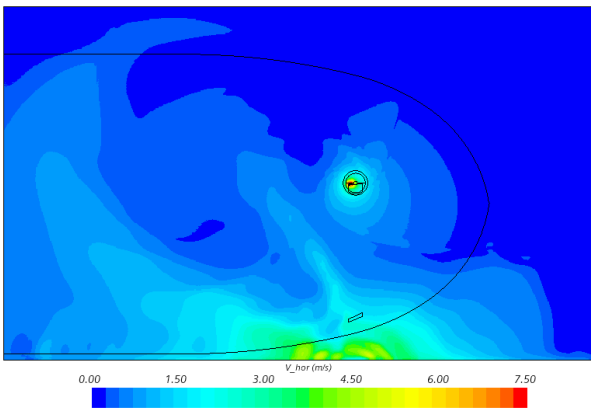


Figure E.1: Horizontal bottom velocity 1 cm above bed for Test 1 after 93s

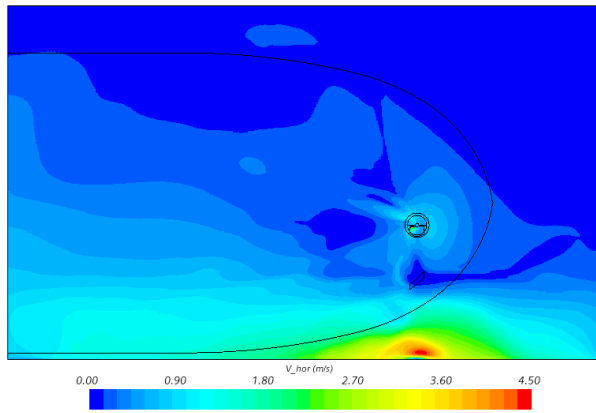


Figure E.2: Horizontal bottom velocity 1 cm above bed for Test 2 after 99s

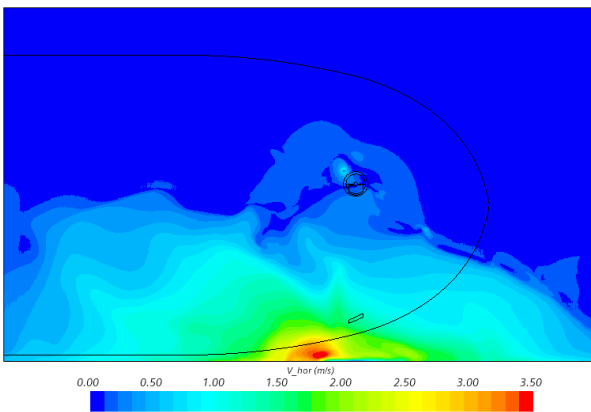


Figure E.3: Horizontal bottom velocity 1 cm above bed for Test 11 after 81s

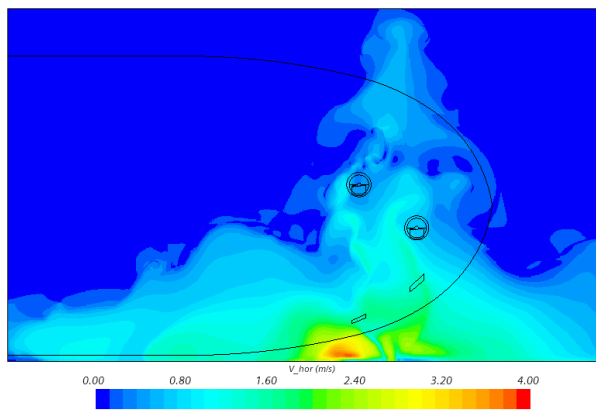


Figure E.4: Horizontal bottom velocity 1 cm above bed for Test 13 after 75s

F

Wall velocity field

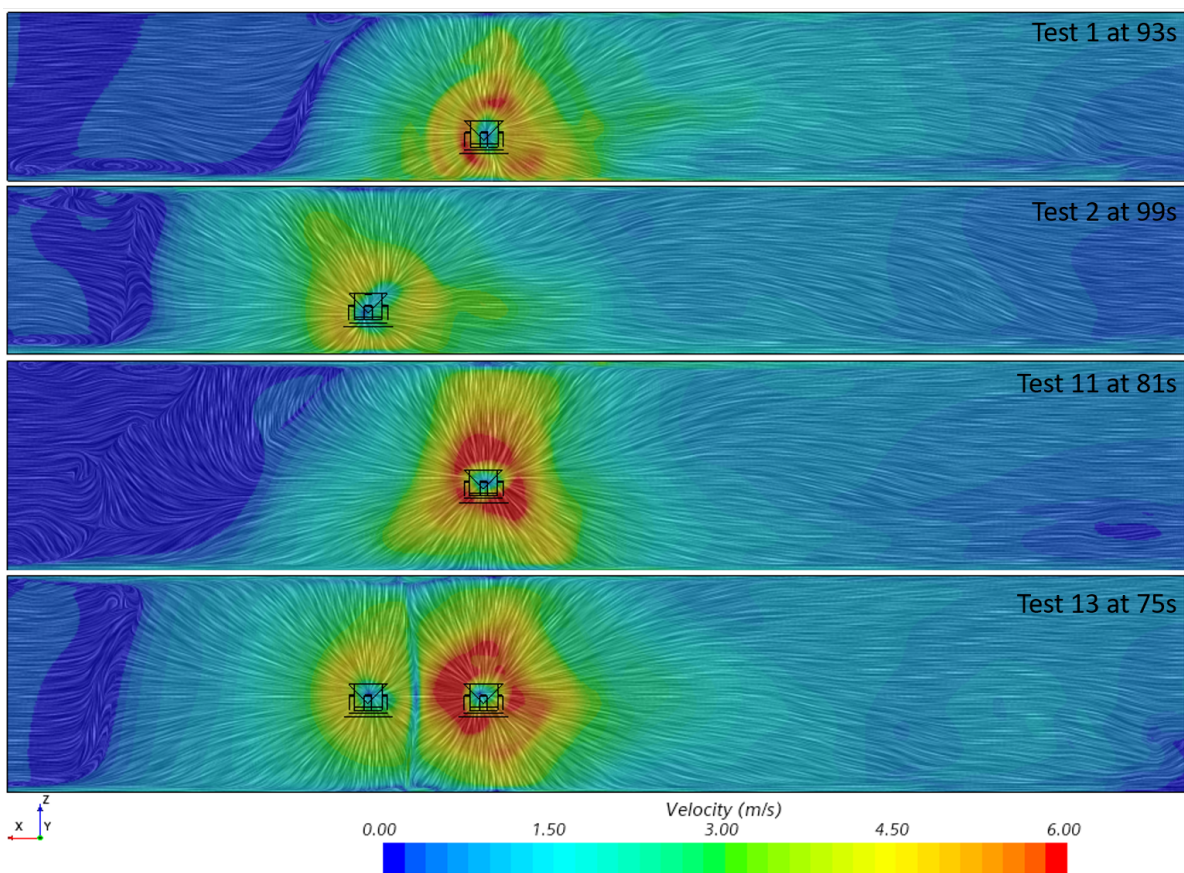


Figure F.1: Velocity field 1 cm from the quay wall for Test 1, 2, 11 and 13



Velocity along line

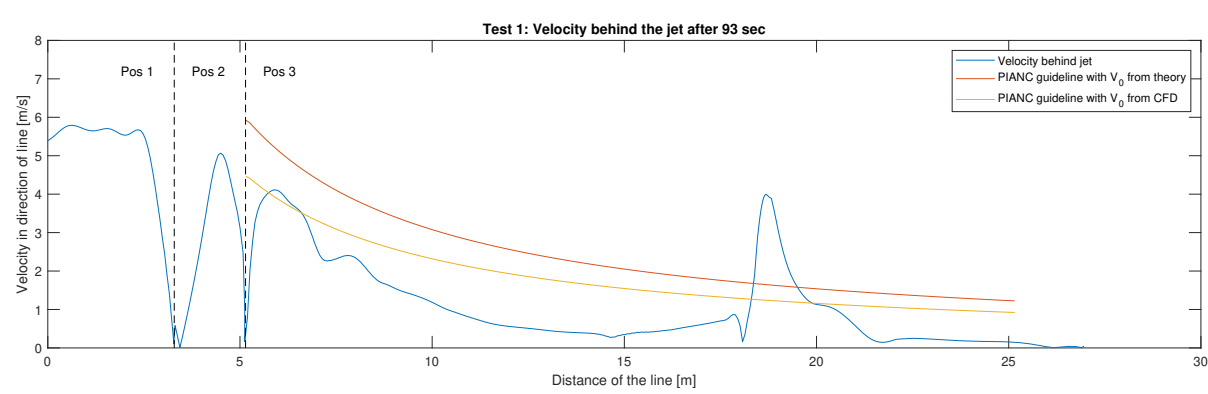


Figure G.1: Velocity degradation along line in Test 1 after 93s

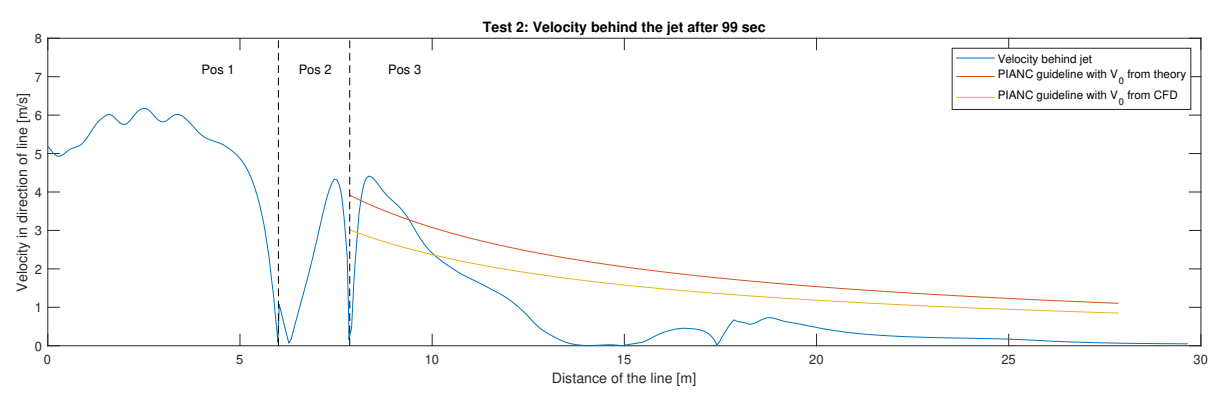


Figure G.2: Velocity degradation along line in Test 2 after 99s

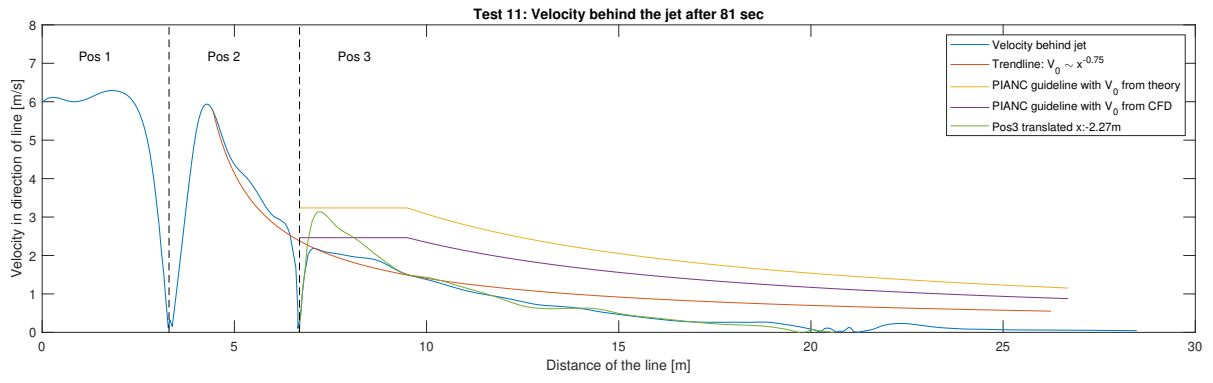
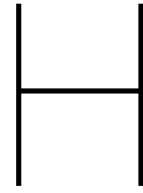


Figure G.3: Velocity degradation along line in Test 11 after 81s



Roughness

This appendix is meant to explain how the low-law velocity profile for smooth surfaces could be modified to account for roughness. The formulae are adopted from the STAR-CCM+ User Manual [24]. When the wall is smooth, the velocity profile normal to the wall follows equation 2.16 mentioned in section 2.3.2. Increasing the sand grain size at the bottom means that the roughness increases and as a result, the wall shear stress increases near the wall. This formula can be adjusted to include wall roughness into the model. This is done by adjusting the formula to equation H.1 and account for the additional shear from the roughness elements.

$$u^+ = \frac{1}{\kappa} \log(E'y^+) \quad 30 < y^+ < 200 \quad (\text{H.1}) \quad E' = \frac{E}{f} \quad (\text{H.2})$$

Where:

- u^+ = Non dimensional wall-tangential velocity component [-]
- y^+ = Non dimensional wall distance [-]
- κ = Von Karman constant (empirical constant) [-]
- E = Log law offset (empirical constant) [-]
- E' = Log law offset with wall roughness [-]
- f = Roughness function [-]

This roughness function is depending on the size and the shape of the roughness elements. When the roughness function increases the orange dotted line shifts down in figure H.1, so the u^+ value reduces. This plot appears to show that increasing the roughness, reduces the velocity adjacent to the wall, but u^+ is a dimensionless number defined by $u^+ = u/u_*$. Especially the wall shear stress increases and therefore the u_* value, because $u_* = \sqrt{\tau_w/\rho}$.

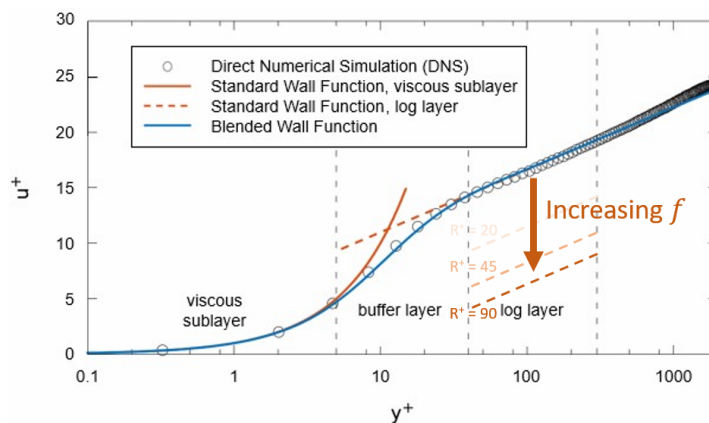


Figure H.1: Law of wall (adjusted from Simcenter STAR-CCM+ [24])

The size of the roughness elements on the bottom are represented by the roughness distance normal to the wall r . For uniform sand grains, r is equal to the sand grain diameter. Most of the time the roughness elements have many different shapes and sizes and the mean or median diameter is chosen as a representative value for r . The roughness height r is non-dimensionalized by equation H.3.

$$R^+ = \frac{r\rho u_*^*}{\mu} \quad (\text{H.3})$$

Where:

- R^+ = Roughness parameter [-]
- r = Equivalent sand-grain roughness height [m]
- ρ = Density [kg/m³]
- u_* = Velocity scale [m/s]
- μ = Dynamic viscosity [Ns/m²]

Note that this is expressed in the same form as the dimensionless wall distance y^+ . The assumption is that the dimensionless roughness height R^+ is always much smaller than the dimensionless wall normal distance y^+ . This assumption is true for small sand grain sizes close to the wall. But loose rocks could form a problem, due to this assumption.

The roughness function f is split into three regions, smooth ($R^+ < R_{\text{smooth}}^+$), transitional ($R_{\text{smooth}}^+ < R^+ < R_{\text{rough}}^+$) and rough ($R^+ > R_{\text{rough}}^+$). The roughness function is depending on the size of the roughness elements R^+ and on the shape and spacing of these elements C , see equation H.4 and H.5.

$$f = \left\{ \begin{array}{ll} 1 & \text{for } R^+ < R_{\text{smooth}}^+ \\ \left[B \left(\frac{R^+ - R_{\text{smooth}}^+}{R_{\text{rough}}^+ - R_{\text{smooth}}^+} \right) + CR^+ \right]^a & \text{for } R_{\text{smooth}}^+ < R^+ < R_{\text{rough}}^+ \\ B + CR^+ & \text{for } R^+ > R_{\text{rough}}^+ \end{array} \right\} \quad (\text{H.4})$$

$$a = \sin \left[\frac{\pi}{2} \frac{\log(R^+/R_{\text{smooth}}^+)}{\log(R_{\text{rough}}^+/R_{\text{smooth}}^+)} \right] \quad (\text{H.5})$$

Where:

- f = Roughness function [-]
- B = Model coefficient [-] (default STAR-CCM+ value: 0)
- C = Model coefficient [-] (default STAR-CCM+ value: 0.253)
- R_{smooth}^+ = Model coefficient [-] (default STAR-CCM+ value: 2.25)
- R_{rough}^+ = Model coefficient [-] (default STAR-CCM+ value: 90)

For the smooth region, the roughness function f equals 1, which means that $E' = E$ and the non dimensional velocity component u^+ is equal to the original formula, see equation H.2 and H.1. For large R^+ values the u^+ value saturates, this can also be seen in figure H.1. And the roughness height r should not be larger than the cell.

Instantaneous vs. mean

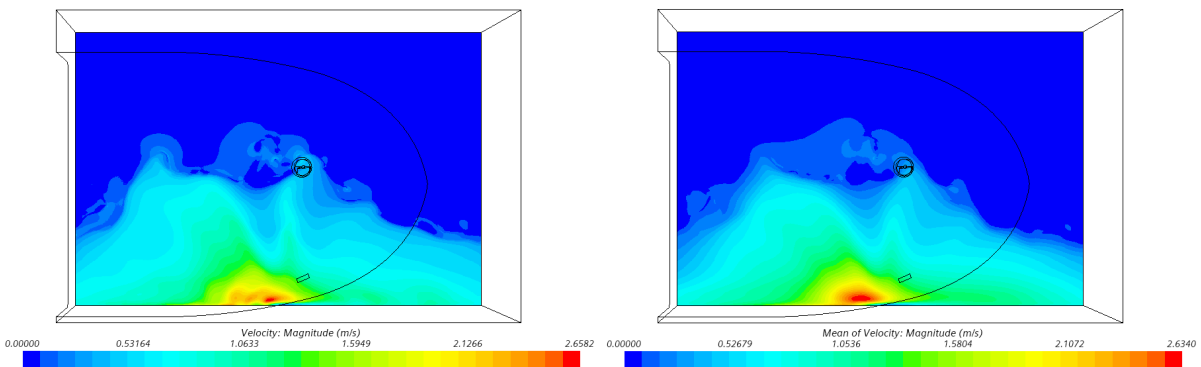


Figure I.1: Instantaneous velocity field of the parameter sensitivity test run for keel clearance of 4.11m after 100s

Figure I.2: Mean velocity field of the parameter sensitivity test run for keel clearance of 4.11m between 80-100s

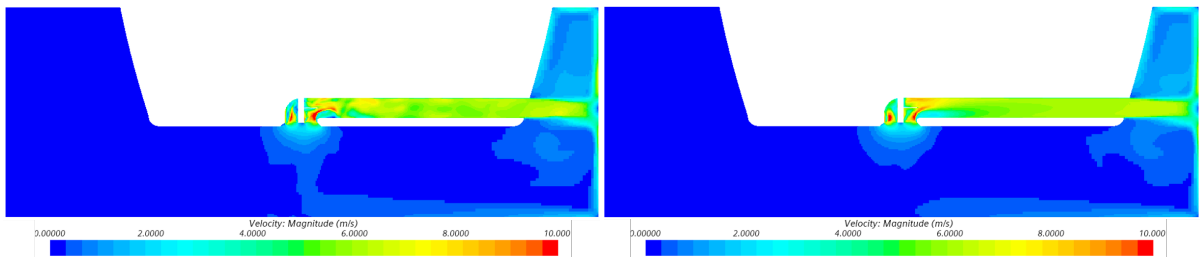


Figure I.3: Instantaneous velocity field of the parameter sensitivity test run for keel clearance of 4.11m after 100s

Figure I.4: Mean velocity field of the parameter sensitivity test run for keel clearance of 4.11m between 80-100s

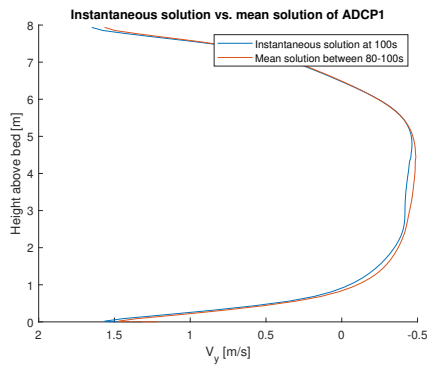


Figure I.5: Instantaneous and mean velocity profile through ADCP1 location of Wall clearance 5.70m run